MULTI-MODE SPIN DYNAMICS OF A BOSE-EINSTEIN CONDENSATE IN AN OPTICAL LATTICE

POUL LINDHOLM PEDERSEN
Department of Physics and Astronomy
University of Aarhus, Denmark

Ph.D. thesis
August 2014

This thesis is submitted to the Faculty of Science and Technology at the University of Aarhus, Denmark, in order to fulfill the requirements for obtaining the PhD degree in Physics.
The studies have been carried out at the Department of Physics and Astronomy under supervision of Associate Professor Jan Arlt, from September 2010 to August 2014.

Front cover illustration: The $m_F = \pm 1$ spin components produced through spin-changing collisions in a Bose-Einstein condensate. The clouds are averaged over 54 realisations.

ABSTRACT

The creation of Bose-Einstein condensates has revolutionised atomic physics. Access to a source of coherent atomic clouds has made the experimental verification of theoretical models has taken physics research to a new regime, where theoretical models may be implemented In this thesis, a number of new approaches towards creation and manipulation of macroscopic quantum states is presented. The research falls into two main areas:

The first research area explores the wave packets and localized states in an optical lattice. Wave packets are created in the combination of a one-dimensional optical lattice and a weak magnetic trap by amplitude modulation of the lattice. It is shown the wave packets may be deexcited into a lattice state that stays localized for hundreds of milliseconds. The deexcitation process resembles a beam splitter, where the frequency, amplitude and duration of the modulation are experimental parameters for controlling the splitting. After deexcitation, RF radiation allows for manipulation of the localized states.

Within a second research area, spin-changing collisions in a Bose-Einstein condensate are investigated within an optical lattice. The collision process resembles parametric amplification and produces correlated pairs in two different spin states. In the optical lattice, one spatial dimension is effectively frozen out, leading to a two-dimensional configuration. It is shown that the combination of strong axial compression and relatively weak radial confinement leads to a regime, where atoms are scattered into many spatial modes. The spin-changing collisions may be tuned through an applied magnetic field. Our investigations show that the spatial structure is a superposition of energetically allowed modes, leading to the observation of ring structures.

The correlated pairs created in this process have potential as a source for EPR states showing non-local entanglement. We demonstrate anti-correlation in momentum owing to the conservation of momentum in the collision process, and show that only a subset of the allowed modes participate, indicating that a bosonic stimulation of certain modes occurs.

The final part of this thesis describes progress towards atom number stabilisation using Faraday detection. Preliminary results show a stability of 10^{-3} of a thermal cloud close to the critical temperature of ^{87}Rb.

RESUMÉ

Skabelsen af Bose-Einstein-kondensater har revolutioneret atomfysikken. Den eksperimentalle adgang til koærente skyer af atomer har gjort det simplere at bekræfte teoretiske modeller, der ellers sjældent lader sig realisere. I denne afhandling beskrives nye tilgange til at skabe og manipulere makroskopiske, kvantemekaniske tilstande. Forskningen kan inddeles i to hovedområder:

I det første område undersøges bølgepakker og lokaliserede tilstande i et optisk gitter.Bølgepakkerne skabes i det samlede potential fra en svag magnetisk fælde og et en-dimensionalt optisk gitter, der amplitudemoduleres. Imens atomerne oscillerer i den magnetiske fælde, kan bølgebakkerne deeksiteres til en tilstand i det optiske gitter, hvor de forbliver lokaliserede i hundredvis af millisekunder. Deeksitationsprocessen efterligner en optisk *beam splitter*, hvor en del af bølgepakken overføres til gittertilstanden, mens resten propagerer videre. Delingsforholdet kan kontrolleres med frekvensen, amplituden og varigheden af pulsen, og de lokaliserede tilstande kan yderligere manipuleres med RF-stråling.

I det andet område beskrives spin-ændrende kollisioner i et spinor-kondensat i et optisk gitter. Kollisionsprocessen er identisk med parametrisk forstærkning og producerer korrelerede atompar i to forskellige spin-tilstande. I det optiske gitter er en af de rumlige dimensioner frosset ud, så kondensatet er i en to-dimensional konfiguration, og kombinationen af en stærk aksial fortætning og en forholdsvis svag radial indespærring placerer systemet i et *multi-mode*-regi.

Spinkonfigurationen efter en spin-ændrende kollision har lavere energi end før kollisionen. Den overskydende energi omdannes til rumlige eksitationer, og da mængden af resterende energi kan justeres med et ydre magnetfelt, kan den rumlige profil varieres gennem magnetfeltet. I *multi-mode*-regiet er den rumlige struktur en superposition af tilgængelige *modes*, hvilket fører til ringformede skyer efter frit fald.

De korrelerede par, der dannes i denne proces, kan på længere sigt bruges som en kilde til EPR-tilstande, der udviser ikke-lokal sammenfiltring. Vi demonstrerer anti-korreleration af impuls på grund af impulsbevarelse og viser, at kun en delmængde af de tilladte modes deltager i den den rumlige profil. Dette indikerer en bosonisk stimulering af udvalgte modes i kollisionerne.

I sidste del af afhandlingen bekrives igangværende eksperimenter, der leder frem mod stabilisering af mængden af atomer ved hjælp af feedback på RF-frekvensen i løbet af fordampningskølingen. Foreløbige resultater for en termisk sky af ^{87}Rb tæt på den kritiske temperatur viser en stabilitet på 10^{-3}.

PREFACE

The work presented in this thesis was carried out in the “Lattice experiment” within the Ultracold Quantum Gases Group at Aarhus University over four years. I started my PhD in September 2010 together with Nils Winter on an experiment that had been largely unused for the last year. Jan Arlt had taken over responsibility for restoring this experiment together with Jacob Sherson and Sune Mai, and upon my arrival, the laboratory was brought to a working state. With the graduation of Sune Mai we were left in the unusual situation of working with a well-designed experiment, but not knowing the details of it, since none of us had been involved in its construction. Armed with the thesis of Henrik Kjær Andersen, we developed a deeper understanding of the experiment over the following year, expecially during the move of the laboratory to its current location.

Through my PhD, my work has been divided between three projects: localized wave packets in an optical lattice, spin dynamics in an optical lattice and non-destructive Faraday detection of a BEC. The wave packet work was initiated by Sung Jong Park and Sune Mai, and these investigations were continued and published. However, during the first year it was decided that I should focus on spinor physics, and this subject naturally takes up the largest part of this thesis. At the same time, it was decided that Ph.D student Miroslav Gajdacz should focus on Faraday detection and feedback.

Acknowledgements

I would like to thank my supervisor Jan Arlt for guiding me through the world of experimental quantum optics. You have been extremely patient in explaining almost every aspect of quantum gases, and it has been wonderful that you have always taken the time to discuss even the smallest topic with your PhD students. I would also like to thank Jacob Sherson for fruitful discussions and for sharing his extensive knowledge on all kinds of quantum systems.

I have also been so fortunate to work together with Miroslav Gajdacz as my fellow PhD, and I would like to thank him for all the good times we have had in the lab. I am amazed by your intuition about physics – both theoretical and experi-

mental – and I have enjoyed your good spirits and silly humour. In the summer of 2012, Andrew Hilliard joined the experiment as a post doc, and I am grateful for all the time he took to teach me all the tricks of the trade, and teaching me the value of doing things *right* – and for proofreading this thesis. Troels Mørch worked as a master student in the lab throughout 2012 and delivered a dedicated effort in the never-ending battle against magnetic noise. Also, bachelor student Theis Skalmstang did a great job in upgrading our microwave apparatus with a very flexible synthesizer.

A big contribution in the process of creating and maintaining the experiment comes from the workshops at the institute. The Lattice experiment would certainly not exist without them, and I would like to thank the mechanical and electronic workshops for their effort. In particular, Erik Søndergaard has helped me design and repair lots of circuits, and Torben Hyltoft has been of great help in the workshop.

Time in the office would not have been as enjoyable if it was not for the company of Sune Vestergaard Dupont, Niels Hygum Nielsen, Lasse Haahr Lillevang and Anders Lind Skov. Administrative tasks would also have been much more troublesome without the aid of Grete Flarup. Also, my insight in the myterious world of theoretical physics would have been smaller without all the discussions with Jens Kusk Block.

A big thanks goes to the people in, around, and out of TÅGEKAMMERET. Especially to everyone involved with the TÅGEKAMMER revue where I have spent countless weekends rehearsing, singing and joking with a fantastic bunch of entertainers, but also to the board of 2010/11 – you are the BEST!

Finally, I would like to thank my family for their constant support – even on the voyage into the strange world of research. The last and biggest thanks goes to my girlfriend Caroline. Your presence in my life makes me happier for each day.

LIST OF PUBLICATIONS

- J. F. Sherson, S. J. Park, P. L. Pedersen, N. Winter, M. Gajdacz, S. Mai and J. Arlt, *The pump-probe coupling of matter wave packets to remote lattice states*, New Journal of Physics **14** (2012), 8, p. 083013.
  doi:10.1088/1367-2630/14/8/083013

- P. L. Pedersen, M. Gajdacz, N. Winter, A. J. Hilliard, J. F. Sherson and J. Arlt, *Production and manipulation of wave packets from ultracold atoms in an optical lattice*, Phys. Rev. A **88** (2013), p. 023620.
  doi:10.1103/PhysRevA.88.023620

- M. Gajdacz, P. L. Pedersen, T. Mørch, A. Hilliard, J. Sherson and J. Arlt, *Non-destructive Faraday imaging of dynamically controlled ultracold atoms*, Rev. Sci. Instr. **84** (2013), 8, p. 083105.
  doi:10.1063/1.4818913

- P. L. Pedersen, M. Gajdacz, F. Deuretzbacher, L. Santos, C. Klempt, J. F. Sherson, A. J. Hilliard and J. J. Arlt, *Spin dynamics in a two-dimensional quantum gas*, Phys. Rev. A **89** (2014), p. 051603.
  doi:10.1103/PhysRevA.89.051603

CONTENTS

CHAPTER 1

INTRODUCTION

1.1 Bose-Einstein condensates and quantum technology

Since the beginning of the 20th century, quantum mechanics has been the leading theory for describing matter and its dynamics at the microscopic level. The pioneering work of Niels Bohr, Erwin Schrödinger, Werner Heisenberg, Paul Dirac and many others led to the formulation of quantum theory as we know it today. Although its measurement postulates and lack of determinism makes this theory seem absurd to our everyday world, it has been a major driving force in the development of the technology of the 20th century, from semiconductors and computers, to lasers and atomic clocks.

Today, quantum mechanics still plays a prominent role in technical advances in the 21st century through the exploitation of its non-intuituve features. The field of quantum information relies heavily on the ability to prepare and manipulate quantum states, and the physical realisation of quantum computation has been a focus of research throughout the last decade. One of the milestones in the development of quantum technology was the production of an almost ideal quantum system – the Bose-Einstein condensate (BEC).

A BEC is a macroscopic ensemble of particles that occupy a single quantum state. In classical physics, a macroscopic population of a given state is impossible according to Maxwell-Boltzmann statistics, and thus a Bose-Einstein condensate is a clear manifestation of quantum statistics. The fact that the particles occupy the same quantum state means that they are described by the same wave function and hence constitute a coherent ensemble. In this respect, the BEC is the atomic counterpart of a laser, and compared to typical solid-state systems, it is extremely pure, which makes it ideal for implementing quantum mechanical models.

The prediction of the Bose-Einstein condensate dates back to 1925, when Albert Einstein discovered unusual behaviour in the statistical description of an ensemble of atoms at low temperatures [1]. The formula governing the description of photons had been proposed by Satyendra Nath Bose the year before [2], and Einstein succeeded in expanding the theory to particles of matter, although it was not yet understood that this only was valid for bosons.

The fact that a macroscopic population of the ground state suddenly appeared as a secondary phase in the system aroused Einstein's scepticism, but the idea was picked up by Fritz London a decade later in an attempt to explain the superfluidity of helium-4 [3]. Although Einstein's condensation was still only considered of "purely imaginary existence", it was now connected to the phenomenon of superfluidity.

Superfluidity is the vanishing viscosity of a liquid in the same manner as a superconductor conducts current without resistance below a critical temperature. Later, theoretical work indicated that the lack of viscosity was a quantum phenomenon related to the appearance of a coherent condensate fraction [4]. Thus, atomic BECs and liquid helium share many properties, but the density of liquid helium made the direct observation of condensation impossible.

The first positive experimental verification of Bose-Einstein condensation was achieved 70 years after its prediction by three independent groups [5–7]. Advances in laser cooling and evaporative cooling allowed for the direct observation of a BEC in a dilute atomic vapour at the lowest temperatures yet achieved, and the achievement was awarded the 2001 Nobel Prize [8].

One of the remarkable properties of a BEC is that it constitutes a coherent ensemble. This was demonstrated by interfering two independent BECs [9] and through the creation of atom lasers [10]. Another fascinating consequence of the coherence of BECs is the quantisation of rotation in vortices. Since the velocity of the condensate is related to the gradient of the phase $\nabla\varphi$, rotation requires a phase change of 2π around the centre in order to be single-valued. At the rotation centre, this is impossible to satisfy, and the result is a vortex with vanishing density at its core [11, 12].

Since the initial wave of pioneering experiments, the field of ultracold atoms has expanded at an incredible rate, and by now BECs are made on a daily basis in numerous laboratories around the world. Condensation has been achieved in many species, not only alkali atoms, but also electronically complex species like chromium [13], and heavy atoms such as ytterbium [14].

1.2 Optical lattices and quantum simulation

With the first BEC loaded into an optical lattice [15], research in cold atoms entered a new regime. An optical lattice is a standing light wave with a periodicity given by half the wavelength of the light. For a one-dimensional optical lattice,

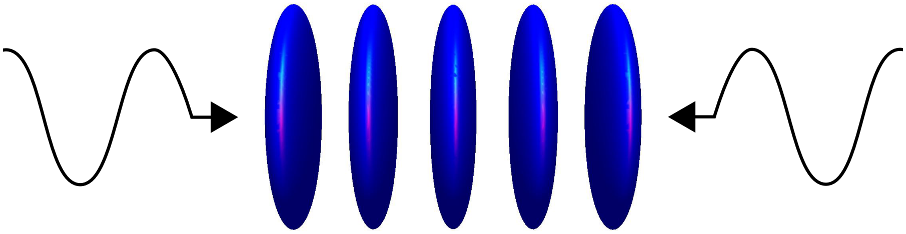

FIGURE 1.1: Illustration of a one-dimensional optical lattice. Two counter-propagating light beams interfere, resulting in a standing wave. The surface marks $1/e$ of the maximal potential.

consisting of a single retro-reflected light beam, the resulting pattern is an array of ellipsoids of high intensity as seen in figure 1.1. If the light is red-detuned to an optical transition in an atom, it acts as an attractive potential through the AC Stark shift, which makes it possible to confine atoms in the regions of high light intensity. The combination of a BEC and an optical lattice thus realises a coherent ensemble confined in a periodic potential, and thus this system is an ideal model for solid state materials.

This line of research led to the observation of the transition between a superfluid phase and a Mott insulating phase [16, 17]. The Mott insulator originates in solid state physics when the electrons in a lattice structure become "pinned" to their sites due to strong interactions with neighbouring electrons, making the system electrically insulating. The superfluid to Mott insulator transition is also fascinating because it is the manifestation of a quantum phase transition, i.e. a transition not driven by thermal energy, but solely by quantum fluctuations.

When an atom is captured in a single lattice beam, the confinement in the direction of the lattice axis is very tight compared to the other directions. This effectively reduces the atomic motion to two dimensions for a sufficiently cold sample. This procedure may be extended to higher dimensions by intersecting two lattice beams at right angles. Two beams thus create a potential that is shaped like rods resulting in a collection of one-dimensional clouds, and three beams create a zero-dimensional structure, analogous to a face-centered cubic lattice. Other geometries of optical lattices include triangular [18] and hexagonal [19], and this versatility makes it possible to realise many configurations known from solid state physics.

From a theoretical point of view, a BEC in an optical lattice is particularly interesting because the system realises the Bose-Hubbard model [16]. This simple model describes particles confined to lattice sites in the tight-binding approximation and consists only of two terms: tunnelling to neighbouring sites and on-site interactions. For an ideal potential, the Hamiltonian is thus given by

$$\hat{H} = -J \sum_{\langle i,j \rangle} \hat{a}_i \hat{a}_j^\dagger + \frac{U}{2} \sum_i \hat{n}_i(\hat{n}_i - 1), \tag{1.1}$$

where J is the tunnelling constant, $\hat{a}_i$ is the annihilation operator for a particle at the site i, and U is the on-site interaction.

This surprisingly simple equation is able to account for both superfluid and Mott insulator phases. Thus it is one of the major driving forces behind *quantum simulation*. If a complex system can be modelled by a simple, ideal system, then the implementation of this system allows for a simulation of the complex system. This is closely related to the ideas about a universal quantum simulator, presented by Feynmann in 1982 [20], and draws considerable attention to the field of quantum gases [21].

The combination of a BEC and an optical lattice has also led to remarkable advances within *quantum information processing*. By loading a two-dimensional cloud into an optical lattice, it was possible to make a two-dimensional Mott insulator and detect the atoms at each site of the lattice using a microscope with a high numerical aperture [22]. Further experiments showed that the spin state of an atom on a single site could be changed through the combination of a tightly focused beam and microwave radiation [23]. Such a system provides an important step towards realising a quantum register with cold atoms. If a single atom can be addressed with high fidelity, it is possible to manipulate and store information in it, and if individual atoms are allowed to interact in a controlled way, quantum computations may be performed in the system.

1.3 Spinor condensates and entangled states

The optical trapping of a BEC opened a new path of research because optical traps can provide confinement that is independent of magnetic substate. Hence optical trapping permitted a new type of experiments focusing on the magnetic properties of a cloud.

Only few months after the first optical trapping was achieved [24], the anti-ferromagnetic nature of the $F = 1$ manifold of sodium was demonstrated by the group of Wolfgang Ketterle [25]. The mechanism responsible for the dynamics in spinor condensates is spin-changing collisions, and the rate of these collisions is typically several orders of magnitude lower than the spin-conserving collisions responsible for thermalisation during evaporative cooling [26].

FIGURE 1.2: Spin-changing collision. Two non-rotating ($m_F = 0$) particles collide, resulting in a pair of counter-rotating ($m_F = \pm 1$) particles.

In the following years, the ground state properties of ^{87}Rb were investigated, showing that the $F = 1$ manifold is ferromagnetic and that the $F = 2$ manifold is polar (anti-ferromagnetic) with a marginally stable cyclic phase [27, 28]. The cyclic phase is not present in the $F = 1$ manifold since it is caused by the additional spin-singlet term in the $F = 2$ Hamiltonian [29].

In later experiments, focus shifted towards the dynamical properties of spinor condensates, and in two simultaneous experiments, the coherence of the spin-changing collisions was demonstrated. In Mainz, a Mott insulator was prepared with a filling of two atoms per site, leading to coherent spin oscillations [30]. In a similar experiment in Georgia, a BEC was loaded into an optical trap and prepared in a superposition of spin states, leading to coherent oscillations among the entire population [31].

The Berkeley group observed the formation of spin domains in a cloud of ^{87}Rb confined in a quasi-two-dimensional cloud [32]. The cloud was prepared in the longitudinal polar state of $F = 1$ and then quenched by ramping the magnetic field down to a value where the transverse polar state is the ground state. This caused the spin to relax to the transverse direction and using phase-contrast imaging, the precession of the spin revealed formation of domains.

A similar approach was employed by the group of Paul Lett, where a cloud was illuminated with off-resonant light using the Faraday effect to measure the differential spinor population in a sodium cloud [33]. At different magnetic fields the signature of the spin oscillations changes, revealing a quantum phase transition as the system crosses the separatrix between oscillatory and running-phase dynamics.

The spin-changing collision where two $m_F = 0$ atoms collide to create a pair of $m_F = \pm 1$ atoms

$$2\,|0\rangle \rightarrow |1\rangle + |-1\rangle \tag{1.2}$$

is sketched in figure 1.2. This collision was central in a series of experiments performed in the Hannover group, where an interesting coupling of the external structure and the spin dynamics was observed [34]. By varying the magnetic field, it was possible to select different eigenstates of the trapping potential, and the degeneracy of two modes leads to spontaneous symmetry breaking [35, 36].

This collision also has the property that it *a priori* is unknown which particle becomes spin up ($|1\rangle$) and which becomes spin down ($|-1\rangle$), leading to the entanglement of the two particles. Furthermore, number squeezing was observed in the system for clouds with 8000 atoms, increasing the measurement precision by 1.6 dB below the shot noise limit [37, 38].

Such a type of entanglement was considered in the famous EPR paper by Einstein, Podolsky and Rosen in 1935 [39]. They imagined two entangled particles separated by a distance being subjected to a measurement. Following their definition of physical realism, they were led to the apparent paradox that measuring one particle would influence the state of the other particle, violating the principle of locality.

Spin dynamics in ultracold gases may provide a novel way to investigate entanglement and the non-intuitive features of quantum mechanics. Furthermore, the entangled atomic pairs may provide useful as a resource in future quantum technologies. Thus the investigation of spin dynamics is a highly interesting research area in the field of ultracold quantum gases.

1.4 Thesis outline

The work in this thesis is focused on wave packets and spin dynamics in optical lattices. In parallel, non-destructive measurements and feedback were also investigated.

The theoretical framework will be presented in chapter 2 along with general principles used for creating, manipulating and detecting BECs. The basic formalism in dealing with multi-component condensates is also described. Chapter 3 describes the experimental apparatus and the additions that have been made during the last four years. The description is not exhaustive, and the reader is referred to previous theses from the building phase of the experiment [40, 41]. The experiments on wave packets in optical lattices are described in chapter 4. Chapter 5 deals with spin dynamics in a system confined to a two-dimensional geometry in an optical lattice, and the theory of multicomponent condensates is extended to this system. The current progress on spinor work is presented in chapter 6, where the experiments using a dipole trap are discussed. Chapter 7 presents preliminary results on feedback using Faraday detection. Finally, chapter 8 summarises and concludes this thesis.

CHAPTER 2

THEORETICAL BACKGROUND

2.1 Bose-Einstein condensation

The ideal Bose gas

Bose-Einstein condensation is a statistically driven phenomenon. It occurs for bosons – particles with integer spin – that are described by the Bose-Einstein distribution

$$N_i = \frac{1}{\exp\bigl(\beta(\epsilon_i - \mu)\bigr) - 1}, \tag{2.1}$$

where N_i is the mean occupation of th ith state, μ is the chemical potential, k_B is the Boltzmann constant, T is the temperature, and ϵ_i is the energy of the ith state. The total atom number of an ensemble may then be computed by summing N_i over all states.

Here it is important that $\mu < \epsilon_0$ to keep the occupation number of the lowest state positive. This implies that the occupation n_0 of the lowest state grows significantly as $\mu \rightarrow \epsilon_0$. Therefore, one needs to pay special attention when dealing with the lowest state.

The onset of condensation can be simply evaluated for non-interacting particles in a box. Here, $\epsilon_i = p^2/2M$, M is the atomic mass, and the occupation number in excited states can be evaluated with an integral

$$N_\mathrm{th} = \sum_{p\neq 0} \frac{1}{\exp\bigl(\beta(p^2/2M - \mu)\bigr) - 1} \rightarrow \frac{V}{h^3} \int \mathrm{d}^3p \, \frac{1}{\exp\bigl(\beta(p^2/2M - \mu)\bigr) - 1}, \tag{2.2}$$

where V is the volume of the box. The resulting integral belongs to the Bose functions $g_n(z)$ [42, 43] and the equation may be stated in terms of the fugacity $z = e^{\beta\mu}$ as

$$\frac{N_\mathrm{th}}{V} = \frac{1}{\lambda_\mathrm{T}^3} g_{3/2}(z), \tag{2.3}$$

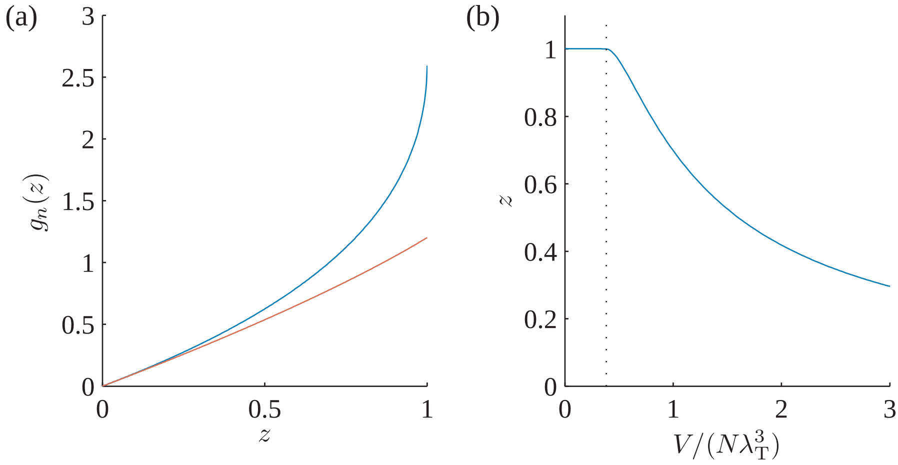

FIGURE 2.1: *(a)* The Bose function $g_n(z)$ for $n = 3/2$ (blue) and $n = 3$ (red). *(b)* Fugacity as a function of $V/(N\lambda_\mathrm{T}^3)$, numerically evaluated from equation (2.3). The critical point is marked with a black, dotted line.

where $\lambda_\mathrm{T} = \sqrt{\frac{2\pi\hbar^2}{Mk_\mathrm{B}T}}$ is the thermal de Broglie wavelength. The function

$$g_{3/2}(z) = \frac{2}{\sqrt{\pi}} \int_0^\infty \frac{1}{z^{-1}e^x - 1} \tag{2.4}$$

grows monotonically with z until $z = 1$ where it reaches its maximal value. Since the value is finite, as seen in figure 2.1 (a), this indicates a critical point, where the distribution function is unable to account for any more atoms.

This is seen more clearly by solving equation (2.3) numerically as a function of $V/(N\lambda_\mathrm{T}^3)$. The solution is shown in figure 2.1 (a), and shows that for large densities and low temperature (small $V/(N\lambda_\mathrm{T}^3)$), the fugacity saturates at the value of one. The critical point is when $z = 1$, and the Bose function attains the value $\zeta\left(\frac{3}{2}\right)$, where ζ is Riemann's zeta function.

However, it is possible to violate equation (2.3) beyond the critical point. If an ensemble of N atoms contained in a volume V exactly at the critical point is cooled further, then λ_T increases, while $g_{3/2}$ is fixed at a value of one. Thus, equation (2.3) cannot accommodate all the atoms in thermal states, since the excited states are statistically "blocked". In this regime, a "two-component" description must be employed in order to account for all the atoms,

$$\frac{N_{\mathrm{tot}}}{V} = \frac{1}{\lambda_{\mathrm{T}}^3} g_{3/2}(z) + N_0(T). \tag{2.5}$$

This step is permissive since the lowest state is not accounted for when going from a discrete sum to an integral.

If the gas is further cooled, the occupation number of the lowest state increases, and from the temperature dependence of λ_{T}, the condensed component grows as

$$N_0(T) = \frac{N_{\mathrm{tot}}}{V}\left[1 - \left(\frac{T}{T_{\mathrm{c}}}\right)^{3/2}\right], \quad \text{(free space)} \tag{2.6}$$

where T_{c} is the critical temperature. This temperature can now be determined as the point where $g_{3/2}$ attains its maximum value: $g_{3/2}(1) = \zeta\left(\frac{3}{2}\right)$, where ζ is Riemann's zeta function. This is often described in terms of the *phase-space density* $\varpi = n\lambda_{\mathrm{T}}^3$:

$$\varpi(T_{\mathrm{c}}) = \zeta\left(\tfrac{3}{2}\right). \qquad \text{(free space)} \tag{2.7}$$

These results are derived for free space, but obviously, any real experiment must deal with a gas trapped in some external potential. This does not change the qualitative results, but the density of states is different, which leads to different scaling.

Consider a 3D harmonic trap defined by the potential

$$V\big(x, y, z\big) = \tfrac{1}{2} M \left(\omega_x^2 x^2 + \omega_y^2 y^2 + \omega_z^2 z^2\right), \tag{2.8}$$

where $\omega_x, \omega_y, \omega_z$ are the (angular) trap frequencies. Here, the relevant Bose function is g_3 [42] which leads to a different form of the condensate fraction

$$N_0 = N_{\mathrm{tot}}\left[1 - \left(\frac{T}{T_{\mathrm{c}}}\right)^3\right]. \tag{2.9}$$

In a harmonic trap, the critical temperature can be found by equating the available thermal states with the total number of atoms, which yields the critical temperature

$$T_{\mathrm{c}} = \frac{\hbar\overline{\omega}}{k_{\mathrm{B}}}\left(\frac{N_{\mathrm{tot}}}{\zeta(3)}\right)^{1/3}, \tag{2.10}$$

where $\overline{\omega} = \sqrt[3]{\omega_x \omega_y \omega_z}$ is the geometric mean of the trap frequencies.

Equation (2.10) sets the temperature scale for condensing an atomic cloud, and one can quickly estimate what temperature to aim for in a BEC experiment: With a mean trap frequency of $2\pi \times 100\,\mathrm{Hz}$ and 10^5 atoms, the critical temperature will be around $200\,\mathrm{nK}$.

The interacting Bose gas

The inclusion of interactions in the description of a BEC changes the energy and spatial profile of the condensate. For repulsive interactions, the radius of the cloud grows compared to the non-interacting gas, but for attractive interactions, the cloud will be unstable [44]. To include interactions in the description, we shall briefly review basic scattering theory. This formalism will also be useful for describing multi-component condensates in section 2.2.

Consider a particle with wave number k, incident along z on the scattering potential of another particle. The resulting wave function can generally be written as an incoming plane wave and a scattered spherical wave

$$\psi = e^{ikz} + f(\theta)\frac{e^{ikr}}{r}, \tag{2.11}$$

where f is the scattering amplitude. To separate the variables, one writes the scattered wave function in terms of an angular part given by Legendre polynomials, $P_l(\cos\theta)$, and a radial part, $R_{kl}(r)$,

$$\psi_{\mathrm{sc}} = \sum_{l=0}^{\infty} A_l P_l(\cos\theta) R_{kl}(r). \tag{2.12}$$

Application of the atomic Hamiltonian

$$\hat{H} = -\frac{\hbar^2}{2M}\nabla^2 + U(\boldsymbol{r}) \tag{2.13}$$

to the radial function yields a radial equation featuring a term $-l(l+1)/r^2$ [45], which is equivalent to a centrifugal barrier. This barrier grows rapidly in energy as l increases, such that only a few terms will contribute to the scattering. For ultracold atoms, one may safely neglect all except the s-wave scattering term ($l = 0$).

In the asymptotic limit $k \to 0$, all information about the scattering process is contained a phase shift which takes the simple form $\delta_0 = ka$, where a is a constant with units of length, known as the *scattering length*. This is equivalent to describing the particles as spheres of radius a, and for identical bosons, the total scattering cross-section is

$$\sigma_{\mathrm{sc}} = \int \left|f(\theta)\right|^2 = 8\pi a^2, \tag{2.14}$$

whereas it is zero for identical fermions. For ^{87}Rb, the scattering length is around $100a_{\mathrm{B}}$, where a_{B} is the Bohr radius.

If the interatomic separation is large compared to the scattering length, then the scattering can be viewed as a contact interaction, which leads to the interaction potential

$$U_0(\boldsymbol{r}) = \frac{4\pi\hbar^2 a}{M}\delta(\boldsymbol{r}). \tag{2.15}$$

This effective interaction greatly reduces the complexity in the description of a many-body system of interacting particles. In the Hartree approximation, the interaction becomes local, which makes the energy functional simple [44]

$$E = N\int d\boldsymbol{r}\left(\frac{\hbar^2}{2M}\left|\nabla\phi(\boldsymbol{r})\right|^2 + V(\boldsymbol{r})\left|\phi(\boldsymbol{r})\right|^2 + \frac{(N-1)}{2}U_0\left|\phi(\boldsymbol{r})\right|^4\right), \tag{2.16}$$

where $\phi(\boldsymbol{r})$ is the single-particle wave function, $V(\boldsymbol{r})$ is the trap potential and N is the particle number. To find the ground state, this functional is minimised using μ as a Lagrange multiplier to keep the particle number constant. In the limit where $N \gg 1$, this yields the *Gross-Pitaevskii equation*

$$\left(-\frac{\hbar^2}{2M}\nabla^2\psi(\boldsymbol{r}) + V(\boldsymbol{r}) + U_0\left|\psi(\boldsymbol{r})\right|^2\right)\psi(\boldsymbol{r}) = \mu\psi(\boldsymbol{r}), \tag{2.17}$$

where $\psi(\boldsymbol{r}) = \sqrt{N}\phi(\boldsymbol{r})$, $n(\boldsymbol{r}) = |\psi(\boldsymbol{r})|^2$, and μ is the chemical potential. The wave function is the order parameter for the condensed phase, as it is zero in the non-condensed phase, and finite in the condensed phased.

For an ultracold cloud, this equation may be further simplified by the *Thomas-Fermi approximation.* At zero temperature, the kinetic term in equation (2.17) can be neglected, which makes the solution for the atomic density very simple

$$n(\boldsymbol{r}) = \frac{\mu - V(\boldsymbol{r})}{U_0}, \quad \mu - V(\boldsymbol{r}) > 0. \tag{2.18}$$

For a typical three-dimensional harmonic trap potential, this yields a cloud with the shape of an inverted parabola

$$n\big(x,y,z\big) = n(0)\left(1 - \frac{x^2}{R_x^2} - \frac{y^2}{R_y^2} - \frac{z^2}{R_z^2}\right), \quad \mu - V(\boldsymbol{r}) > 0, \tag{2.19}$$

where $R_i = \sqrt{2\mu/M\omega_i^2}$ are the *Thomas-Fermi radii.*

The chemical potential for the cloud is found by requiring normalisation of the cloud, $\int \mathrm{d}^3\boldsymbol{r}\; n(\boldsymbol{r}) = N$, yielding

$$\mu = \tfrac{1}{2}\left[(15Na)^2 M\hbar^4\overline{\omega}^6\right]^{1/5}. \tag{2.20}$$

2.2 Multi-component condensates

For an ensemble of atoms, where the internal state is not restricted to a single value, the order parameter of the condensed phase can no longer be described by a scalar value. For a system of spin-1 particles, the order parameter is described by the normalised vector $\boldsymbol{\chi} = \left(\chi_1, \chi_0, \chi_{-1}\right)^\mathsf{T}$, and such condensates are often called *spinor condensates*.

This increased number of degrees of freedom allows for more complex dynamics, since the scattering can couple different spin states. This requires a more general formulation of scattering theory, which we will describe below. This will be put into the context of two-dimensional condensates in chapter 5.

Scattering theory for multi-component condensates

The treatment here follows that of Stamper-Kurn and Ueda [46].

We start by considering two particles described by a set of quantum numbers $L_\text{pair}, m_{L,\text{pair}}$ for the external angular momentum, $F_\text{pair}, m_{F,\text{pair}}$ for the internal angular momentum and by a relative wave vector k. A scattering event connects an initial state (subscript i) with a final state (subscript f), but to reduce the large number of possible scattering channels, we shall make some simplifying assumptions:

1. *Cold collisions.* As for the scalar condensates, we assume that the incident energy is low, such that only s-waves are considered ($L_{\text{pair},i} = 0$).

2. *Spinor-gas collisions.* The interaction potential is assumed to be rotationally invariant, meaning that the interaction is unaffected by external, nonsymmetric fields. Even though this is not strictly true, it is a good approximation, and it guarantees that the total angular momentum, F plus L, is conserved.

3. *Weak-dipolar approximation.* The spin-orbit coupling due to the effective interaction is assumed to be weak, such that F and L are conserved individually: $F_{\text{pair},i} = F_{\text{pair},f} = F_\text{pair}$ and $L_\text{pair,i} = L_{\text{pair},f} = 0$.

4. *No F-mixing.* The interaction does not mix the hyperfine manifolds, so a relaxation from $F = 2$ to $F = 1$ is not allowed.

These approximations allow for a simple description in terms of spin-dependent scattering lengths. The allowed values of F_pair are limited by the parity of the atomic state. Under the exchange of the two particles, the total wave function must change by a factor of $(-1)^{2F}$. On the other hand, the spin part of the wave function must change by $(-1)^{F_{\text{pair}}+2F}$, and the orbital part must change by $(-1)^{L_{\text{pair}}}$. For an s-wave collision, this exchange must obey

$$(-1)^{2F} = (-1)^{F_{\text{pair}}+2F}, \tag{2.21}$$

leading to the conclusion that F_{pair} must be even. Equation (2.15) thus takes the form

$$\hat{V} = \frac{1}{2}\sum_{i\neq j}\delta\big(\boldsymbol{r}_i - \boldsymbol{r}_j\big)\sum_{\text{even}\,F_{\text{pair}}}\frac{4\pi\hbar^2 a_{F,\text{pair}}}{M}\hat{P}_{F,\text{pair}}, \tag{2.22}$$

where $a_{F,\text{pair}}$ is the spin-dependent scattering length, M is atomic mass and $\hat{P}_{F,\text{pair}}$ is projector onto the F_{pair} state. This expression may be simplified by using the two identities

$$\sum_{F_{\text{pair}}}\hat{P}_{F,\text{pair}} = \mathbb{1} \tag{2.23}$$

$$\hat{\boldsymbol{F}}_1\cdot\hat{\boldsymbol{F}}_2 = \sum_{F_{\text{pair}}}\Big[\tfrac{1}{2}F_{\text{pair}}(F_{\text{pair}}+1) - F(F+1)\Big]\hat{P}_{F,\text{pair}}. \tag{2.24}$$

For the $F = 2$ manifold, one may eliminate the P_4 and P_2 projectors, leading to an interaction potential of the form

$$V(\boldsymbol{r}) = \sum_{i\neq j}\tfrac{1}{2}\delta\big(\boldsymbol{r}_i - \boldsymbol{r}_j\big)(c_0 + c_1\boldsymbol{F}_1\cdot\boldsymbol{F}_2 + c_2P_0), \tag{2.25}$$

where the constants are given by

$$\begin{aligned} c_0 &= \tfrac{1}{7}(4g_2 + 3g_4)\\ c_1 &= \tfrac{1}{7}(-g_2 + g_4)\\ c_2 &= \tfrac{1}{7}(7g_0 - 10g_2 + 3g_4), \end{aligned} \tag{2.26}$$

and $g_F = 4\pi\hbar^2/M$ is the coupling strength for the F-channel.

It is worth noting the different effects of the three terms: The first, c_0, does not alter spin, so it is responsible for spin-preserving collisions; since all scattering lengths are of the same magnitude, this term will dominate. The other two terms depend on the spin configuration, and they lead to spin-changing collisions.

Effective Hamiltonian in the linear regime

We shall now take the Hamiltonian to the experimentally relevant setup of a condensate prepared in the $F = 2$, $m_F = 0$ state. For the experiments presented in chapter 5, only the initial, linear regime is relevant, which effectively will turn the $F = 2$ manifold into an $F = 1$ system.

In second quantised form, the single-particle Hamiltonian for the system is given by[1]

$$\hat{H}_0 = \sum_{m_F} \int \mathrm{d}^3\boldsymbol{r}\, \hat{\psi}^\dagger_{m_F}(\boldsymbol{r}) \left(-\frac{\hbar^2}{2M}\nabla^2 + V(\boldsymbol{r}) + E_Z \right) \hat{\psi}_{m_F}(\boldsymbol{r}), \tag{2.27}$$

where $\hat{\psi}_{m_F}$ is the annihilation operator for a particle in state m_F, $V(\boldsymbol{r})$ is the trap potential, and E_Z is the Zeeman energy. The Zeeman energy will be addressed further in section 2.3, but for now, it is sufficient to write it as

$$E_Z = p m_F + q m_F^2, \tag{2.28}$$

which is defined relative to the $m_F = 0$ state, and takes both the linear and quadratic shift into account.

The interaction Hamiltonian in second quantisation has the form

$$\hat{H}_{\text{int}} = \tfrac{1}{2} \int \mathrm{d}^3\boldsymbol{r} \sum_{\boldsymbol{m}} U_{\boldsymbol{m}} \hat{\psi}^\dagger_{m_4}(\boldsymbol{r}) \hat{\psi}^\dagger_{m_3}(\boldsymbol{r}) \hat{\psi}_{m_2}(\boldsymbol{r}) \hat{\psi}_{m_1}(\boldsymbol{r}), \tag{2.29}$$

where each term in the sum describes the scattering of two particles in states m_1 and m_2 into m_3 and m_4, which is described by the vector $\boldsymbol{m} = (m_1, m_2, m_3, m_4)^\intercal$. The factor $U_{\boldsymbol{m}}$ is the coupling constant for the scattering channel, and it is given by the Clebsch-Gordan coefficients

$$U_{\boldsymbol{m}} = \sum_F \sum_{M_F=-F}^{F} g_F \langle m_1, m_2 | F, M_F \rangle \langle F, M_F | m_3, m_4 \rangle . \tag{2.30}$$

Many of the possible channels in equation (2.29) are not allowed as discussed in previous section, and the Hamiltonian may be decomposed into the same three terms as equation (2.25). If we identify the projector $\hat{P}_0$ with the spin-singlet operator $\hat{A}_2 = \sum_{m=-2}^{2} (-1)^m \hat{\psi}_m \hat{\psi}_{-m} / \sqrt{5}$, the interaction Hamiltonian is only given by

---

[1] This section follows the treatment of Garu Gebreyesus [47].

the bosonic field operators and the spin matrices $\hat{\boldsymbol{F}}$

$$\begin{aligned}\hat{H}_{\text{int}} =& \frac{c_0}{2}\int \mathrm{d}^3\boldsymbol{r} \sum_{m'm} \hat{\psi}^\dagger_{m'}(\boldsymbol{r})\hat{\psi}^\dagger_{m}(\boldsymbol{r})\hat{\psi}_{m'}(\boldsymbol{r})\hat{\psi}_{m}(\boldsymbol{r}) \\ &+ \frac{c_1}{2}\int \mathrm{d}^3\boldsymbol{r} \sum_{\boldsymbol{m}} \hat{\psi}^\dagger_{m_4}(\boldsymbol{r})\hat{\psi}^\dagger_{m_3}(\boldsymbol{r})\hat{\boldsymbol{F}}_{m_3m_2}\cdot\hat{\boldsymbol{F}}_{m_4m_1}\hat{\psi}_{m_2}(\boldsymbol{r})\hat{\psi}_{m_1}(\boldsymbol{r}) \\ &+ \frac{c_2}{10}\int \mathrm{d}^3\boldsymbol{r} \sum_{mn}(-1)^{m+n}\hat{\psi}^\dagger_{m}(\boldsymbol{r})\hat{\psi}^\dagger_{-m}(\boldsymbol{r})\hat{\psi}_{n}(\boldsymbol{r})\hat{\psi}_{-n}(\boldsymbol{r}).\end{aligned} \tag{2.31}$$

This Hamiltonian may be taken to the linear regime, where the majority of the atoms are in $m_F = 0$. We apply the Bogoliubov approximation [48]

$$\begin{pmatrix}\hat{\psi}_2(\boldsymbol{r})\\ \hat{\psi}_1(\boldsymbol{r})\\ \hat{\psi}_0(\boldsymbol{r})\\ \hat{\psi}_{-1}(\boldsymbol{r})\\ \hat{\psi}_{-2}(\boldsymbol{r})\end{pmatrix} = \begin{pmatrix}\psi_2(\boldsymbol{r})\\ \psi_1(\boldsymbol{r})\\ \psi_0(\boldsymbol{r})\\ \psi_{-1}(\boldsymbol{r})\\ \psi_{-2}(\boldsymbol{r})\end{pmatrix} + \begin{pmatrix}\delta\hat{\psi}_2(\boldsymbol{r})\\ \delta\hat{\psi}_1(\boldsymbol{r})\\ \delta\hat{\psi}_0(\boldsymbol{r})\\ \delta\hat{\psi}_{-1}(\boldsymbol{r})\\ \delta\hat{\psi}_{-2}(\boldsymbol{r})\end{pmatrix}, \tag{2.32}$$

where the operator character of the fields is separated as a perturbation to a classical field. In the linear regime, we may approximate $\hat{\psi}_0$ as classical and $\hat{\psi}_{\pm 1}$ as a small perturbation that is quantum mechanical. The $\hat{\psi}_{\pm 2}$ are assumed not to be populated, which leads to the state vector

$$\begin{pmatrix}\hat{\psi}_2(\boldsymbol{r})\\ \hat{\psi}_1(\boldsymbol{r})\\ \hat{\psi}_0(\boldsymbol{r})\\ \hat{\psi}_{-1}(\boldsymbol{r})\\ \hat{\psi}_{-2}(\boldsymbol{r})\end{pmatrix} = \begin{pmatrix}0\\ 0\\ \psi_0(\boldsymbol{r})\\ 0\\ 0\end{pmatrix} + \begin{pmatrix}0\\ \delta\hat{\psi}_1(\boldsymbol{r})\\ 0\\ \delta\hat{\psi}_{-1}(\boldsymbol{r})\\ 0\end{pmatrix}. \tag{2.33}$$

This may then be inserted into the Hamiltonian, and, if we neglect spin-changing collisions in the $m_F = \pm 1$ states, we only need to keep terms of $\delta\hat{\psi}_{m_F}$ to second order. It now remains to calculate the matrix elements and combining equation (2.27) and (2.29) in the expression for the free energy

$$\begin{aligned}\hat{H}-\mu\hat{N}=&\int \mathrm{d}^3\boldsymbol{r}\,\psi_0^*\left(-\frac{\hbar^2}{2M}\nabla^2+V(\boldsymbol{r})+\frac{U_0}{2}\left|\psi_0\right|^2-\mu\right)\psi_0\\&+\sum_{m'=\pm1}\int \mathrm{d}^3\boldsymbol{r}\,\delta\hat{\psi}^\dagger_{m'}\left(-\frac{\hbar^2}{2M}\nabla^2+V(\boldsymbol{r})+(U_0+U_1)\left|\psi_0\right|^2-\mu+q\right)\delta\hat{\psi}_{m'}\\&+U_1\int \mathrm{d}^3\boldsymbol{r}\,\left|\psi_0\right|^2\left(\delta\hat{\psi}^\dagger_1\delta\hat{\psi}^\dagger_{-1}+\delta\hat{\psi}_1\delta\hat{\psi}_{-1}\right).\end{aligned}\tag{2.34}$$

Here,

$$\begin{aligned}U_0&=c_0+\tfrac{1}{5}c_2=\frac{7g_0+10g_2+18g_4}{35}\\U_1&=3c_1-\tfrac{1}{5}c_2=\frac{-7g_0-5g_2+12g_4}{35}.\end{aligned}\tag{2.35}$$

Equation (2.34) has a straightforward interpretation: The first line describes the energy of the $m_F=0$ state, the second line describes the energy of the $m_F=\pm1$ states, and the third line describes the interconversion between $m_F=0$ and $m_F=\pm1$, i.e. spin-changing collisions.

The first line shows that the $m_F=0$ atoms only experience the potential from the trap and the non-linear interaction with other $m_F=0$ atoms. The interaction energy is U_0, so this constant may be associated with spin-preserving collisions.

The $m_F=\pm1$ atoms see a slightly different potential, since the interaction with $m_F=0$ is set by U_0+U_1. These atoms are also affected by the quadratic Zeeman energy.

Furthermore, we can see that the spin-changing collisions are governed by U_1, and the ratio of U_1 to U_0 gives the significance of spin-changing collisions. Using the values from table 2.1, the ratio is seen to be 3.7%.

Finally, it is worth noting that, in the linear approximation, there is no depletion of $m_F=0$, so the dynamics of $m_F=\pm1$ will be decoupled from $m_F=0$, and only the second and third lines of equation (2.34) will be relevant for spin-changing collisions.

2.3 Magnetic field interaction

The interaction of an atom with a static magnetic field gives rise to the well-known Zeeman effect. For weak fields, the interaction causes a splitting of the hyperfine

a_0	87.685
a_2	91.049
a_4	99.197
c_0	94.541
c_1	1.164
c_2	0.128
U_0	94.567
U_1	3.467

TABLE 2.1: Scattering lengths and interaction energies for ^{87}Rb. All quantities are stated in Bohr radii, so c_i and U_i should be multiplied by $4\pi\hbar^2 a_\mathrm{B}/M$. Scattering lengths are calculated by Prof. E. Tiemann, Leibniz Universität Hannover [49].

levels, but in the limit of strong fields, the hyperfine manifolds mix and split according to the value of m_J. The latter limit is known as the *Paschen-Back* regime.

The hyperfine interaction is given by $A_\mathrm{hfs}\hat{\boldsymbol{I}}\cdot\hat{\boldsymbol{J}}$, where $\hat{\boldsymbol{I}}$ is the nuclear spin, $\hat{\boldsymbol{J}}$ is the total electronic angular momentum, and A_hfs is a constant that characterises the interaction strength. In the presence of an external magnetic field, the Hamiltonian is

$$H = -\left(\hat{\boldsymbol{\mu}}_J + \hat{\boldsymbol{\mu}}_I\right)\cdot\boldsymbol{B} + A_\mathrm{hfs}\hat{\boldsymbol{I}}\cdot\hat{\boldsymbol{J}}. \tag{2.36}$$

For the ground state of ^{87}Rb, $I = 3/2$ and $J = 1/2$, which causes the states to separate into two manifolds of $F = 1$ and $F = 2$ when the field is small compared to the hyperfine interaction energy. The two manifolds are separated by the energy $\Delta E_\mathrm{hfs} = (I + \frac{1}{2})A_\mathrm{hfs} = 6.834\,682\,\mathrm{GHz}$.

By expanding equation (2.36) on the $|J\,m_J\,I\,m_I\rangle$ states, one obtains the *Breit-Rabi formula* [50]

$$E_{J=1/2,I,m_F} = -\frac{\Delta E_\mathrm{hfs}}{2(2I+1)} + g_I\mu_\mathrm{B} m_F B \pm \frac{\Delta E_\mathrm{hfs}}{2}\sqrt{1 + \frac{4m_F\xi}{2I+1} + \xi^2}, \tag{2.37}$$

where $\xi = \mu_\mathrm{B}(g_J - g_I)B/\Delta E_\mathrm{hfs}$, g_I and g_J are Landé g-factors for the nuclear and electronic angular momentum, respectively, and μ_B is the Bohr magneton. This expression is valid for the ground state of ^{87}Rb, as shown in figure 2.2.

For low magnetic fields, the linear Zeeman formula is a good approximation to the total shift, but there is a small correction that amounts to a quadratic shift. Taking E_0 as the reference, the *quadratic Zeeman energy* is defined as

$$2q = |E_1 - E_0| - |E_{-1} - E_0|, \tag{2.38}$$

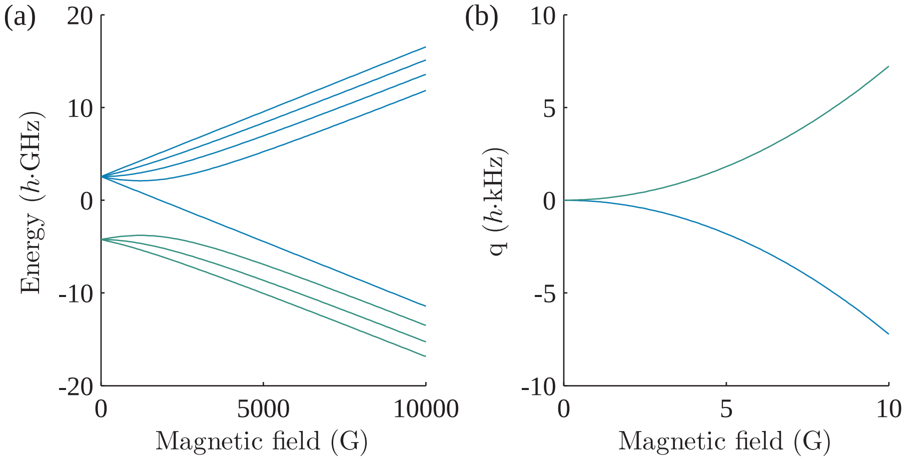

FIGURE 2.2: The Zeeman effect in ^{87}Rb as given by the Breit-Rabi formula. (a) The Zeeman shift from equation (2.37) showing the transition to the Paschen-Back regime, $F = 1$ (green), $F = 2$ (blue). (b) The quadratic Zeeman energy for $F = 1$ (green) and $F = 2$ (blue).

where subscripts refer to m_F. In the limit of small magnetic fields, the term ξ^2 may be neglected, and when expanding the square root to second order, one obtains the expression

$$\begin{aligned} q &= \tfrac{1}{2}(E_1 + E_{-1} - 2E_0) \\ &= \pm\frac{(g_J - g_I)^2}{(2I+1)^2}\frac{(\mu_B B)^2}{\Delta E_{\text{hfs}}} \\ &= \pm h \times 71.59\,\text{Hz/G}^2 B^2, \end{aligned} \tag{2.39}$$

where the upper (lower) sign is for the $F = 1$ ($F = 2$) manifold. The quadratic approximation is valid for $B \lesssim 500$ G, which makes it applicable for all purposes in this thesis.

The fact that q is negative for $F = 2$ means that if one considers two non-interacting particles, they will have lower energy in the $m_F = \pm 1$ state than in the $m_F = 0$ state. When increasing the magnetic field, there will be an increasing excess energy in the collision $2|0\rangle \rightarrow |+1\rangle + |-1\rangle$.

2.4 Atom-light interaction

When a particle is exposed to light, the response is an induced dipole moment p in the atom, which in general may be quantified by a *polarisability* α

$$p = \alpha E, \tag{2.40}$$

where E is the incident electric field. The classical response is given by the Lorentz model, where the real part of α describes dispersion and the imaginary part describes absorption.

This model has a quantum mechanical counterpart which describes the fully quantised interaction between atoms and photons in terms of a polarisability tensor. Such a description is very useful for light that is far-detuned from all considered resonances, and where absorption is negligible. However, for resonant interactions, a simpler description exists using the *optical Bloch equations*.

The optical Bloch equations are a convenient formulation of the Schrödinger equation that includes phenomenological dephasing. These equations are often combined with the Maxwell wave equation to describe the propagation of the light through the atomic sample, known as the Maxwell-Bloch equations. For our purposes, an explicit expression for the atoms is sufficient to describe resonant interactions.

First, the optical Bloch equations are derived and subsequently applied to absorption imaging and microwave interactions. Afterwards, the polarisability tensor is described, and applied to the regime where the Faraday effect dominates. Finally, the dipole force is discussed using a perturbative approach.

The optical Bloch equations

To describe a resonant light-atom interaction, a two-level atomic system is sufficient to explain the experiments in this thesis. A two-level atom can be described by a 2×2 density matrix

$$\hat{\rho} = \begin{bmatrix} \rho_{11} & \rho_{21} \\ \rho_{12} & \rho_{22} \end{bmatrix}, \tag{2.41}$$

where the matrix entries are written as ρ_{ij}. The population in the ground and excited state is given by the diagonal entries ρ_{11} and ρ_{22} respectively. Similarly, the coherences are given by the off-diagonal entries ρ_{12} and ρ_{21}, and since the population is conserved, the relation $\rho_{11} + \rho_{22} = 1$ holds.

Alternatively, the density matrix may be described by the identity matrix $\mathbb{1}$ and the Pauli matrices $\hat{\sigma}_1$, $\hat{\sigma}_2$, and $\hat{\sigma}_3$

$$\mathbb{1} = \begin{bmatrix} 1 & 0 \\ 0 & 1 \end{bmatrix}, \quad \hat{\sigma}_1 = \begin{bmatrix} 0 & 1 \\ 1 & 0 \end{bmatrix}, \quad \hat{\sigma}_2 = \begin{bmatrix} 0 & -i \\ i & 0 \end{bmatrix}, \quad \hat{\sigma}_3 = \begin{bmatrix} 1 & 0 \\ 0 & -1 \end{bmatrix}. \tag{2.42}$$

Combinations of these yield the following relations

$$\begin{aligned} \rho_{11} &= \tfrac{1}{2}(\mathbb{1} + \hat{\sigma}_3), & \rho_{21} &= \tfrac{1}{2}(\hat{\sigma}_1 + i\hat{\sigma}_2), \\ \rho_{12} &= \tfrac{1}{2}(\hat{\sigma}_1 - i\hat{\sigma}_2), & \rho_{22} &= \tfrac{1}{2}(\mathbb{1} - \hat{\sigma}_3). \end{aligned} \tag{2.43}$$

For now, we shall use the Pauli matrices to represent an atomic state because of their mathematical properties, and their physical significance will be described later.

The atomic Hamiltonian may be described as a 2 × 2 matrix [51]

$$\hat{H}_\mathrm{A} = \frac{\hbar\omega_0}{2}\hat{\sigma}_3, \tag{2.44}$$

where ω_0 is the Bohr frequency. The interaction between an atom and an electric field is given by $\hat{H}_\mathrm{int} = -\hat{\boldsymbol{d}} \cdot \boldsymbol{E}$, where $\hat{\boldsymbol{d}}$ is the dipole moment operator of the atom, and $\boldsymbol{E}$ is an electric field. Although we assume the driving field to be electric, the results are as valid with a magnetic field $\boldsymbol{B}$ and a magnetic moment $\boldsymbol{\mu}$. The dipole moment is in general complex, so it can be split into two parts

$$\hat{H}_\mathrm{int} = -\boldsymbol{d}_\mathrm{r} \cdot \boldsymbol{E}\hat{\sigma}_1 + \boldsymbol{d}_\mathrm{i} \cdot \boldsymbol{E}\hat{\sigma}_2, \tag{2.45}$$

where $\boldsymbol{d}_\mathrm{r}$ is the real part of $\boldsymbol{d}$ and $\boldsymbol{d}_\mathrm{i}$ is the imaginary part. The commutator relations for the Pauli matrices $\left[\hat{\sigma}_i, \hat{\sigma}_j\right] = 2i\epsilon_{ijk}\hat{\sigma}_k$ makes it easy to write the equations of motion using the Heisenberg expression

$$\begin{aligned} \dot{\hat{\sigma}}_1 &= -\omega_0\hat{\sigma}_2 + \tfrac{2}{\hbar}\boldsymbol{d}_\mathrm{i} \cdot \boldsymbol{E}\hat{\sigma}_3 \\ \dot{\hat{\sigma}}_2 &= \omega_0\hat{\sigma}_1 + \tfrac{2}{\hbar}\boldsymbol{d}_\mathrm{r} \cdot \boldsymbol{E}\hat{\sigma}_3 \\ \dot{\hat{\sigma}}_3 &= -\tfrac{2}{\hbar}\boldsymbol{d}_\mathrm{r} \cdot \boldsymbol{E}\hat{\sigma}_2 - \tfrac{2}{\hbar}\boldsymbol{d}_\mathrm{i} \cdot \boldsymbol{E}\hat{\sigma}_1. \end{aligned} \tag{2.46}$$

These equations may be taken into the semiclassical regime by replacing the (operator) matrices $\hat{\sigma}_1$ with their expectation value $s_i = \langle\hat{\sigma}_i\rangle$. This is good approximation for the many-particle systems that we shall deal with.

We may also make a simplification in equations (2.46), by neglecting the imaginary part of $\boldsymbol{d}$. This corresponds to only considering $\Delta m_F = 0$ transitions, and although we shall primarily be working with $\Delta m_f = \pm 1$ transitions, this approximation is not problematic. The only effect of the approximation is that the field is linearly polarised, which means that the field is polarised parallel to the quantisation axis [51]. We may thus make the substitution $\boldsymbol{d}_\mathrm{r} \cdot \boldsymbol{E} = dE$, and defining $\kappa = 2d/\hbar$ we obtain

$$\begin{aligned}\dot{s}_1 &= -\omega_0 s_2 \\ \dot{s}_2 &= \omega_0 s_1 + \kappa E s_3 \\ \dot{s}_3 &= -\kappa E s_2.\end{aligned} \tag{2.47}$$

There is one final approximation to be made, namely the rotating wave approximation. We assume a sinusoidal field $E = E_0 \cos \omega t$, and we can transfer into a rotating frame by applying a rotation of ωt around the s_3 axis. By neglecting the terms varying with $2\omega t$, we obtain the equations

$$\begin{aligned}\dot{u} &= \Delta v \\ \dot{v} &= -\Delta u + \kappa E_0 w \\ \dot{w} &= -\kappa E_0 v.\end{aligned} \tag{2.48}$$

These variables are basically just the rotated Pauli matrices, and we may relate them to the density matrix by substituting $\hat{\sigma}_1$, $\hat{\sigma}_2$ and $\hat{\sigma}_3$ with u, v and w, respectively, in equation (2.43).

The physical interpretation of these new variables is seen by subtracting ρ_{11} from ρ_{22}. One sees, that w describes the population inversion $\rho_{22} - \rho_{11}$, and from (2.48) it is clear that w is driven by v. In that sense, v describes the absorptive part of the dipole moment, and u describes the remaining dispersive part.

These equations may also be expressed as a vector product between a torque vector $\boldsymbol{\Omega} = (\kappa E_0,\ 0,\ \Delta)^\mathsf{T}$ and the so-called Bloch vector $\boldsymbol{\rho} = (u,\ v,\ w)^\mathsf{T}$

$$\frac{d}{dt}\boldsymbol{\rho} = -\boldsymbol{\Omega} \times \boldsymbol{\rho}. \tag{2.49}$$

This shows that the Bloch vector is constant in magnitude (which is sensible, since we have no loss mechanisms in the equations), and rotates around the torque vector. The vector thus describes a rotation on a sphere – the Bloch sphere – that represents the state of the atom. The Bloch sphere is illustrated in figure 2.3

Since the Bloch vector rotates around the torque vector, it is only possible to reach full population inversion (i.e. all population in the excited state), if $\boldsymbol{\Omega}$ lies in the u-v plane, which in turn requires that the detuning is zero. The rotation

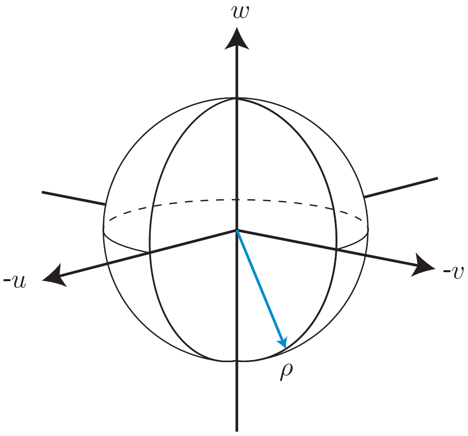

FIGURE 2.3: The Bloch sphere. The state of the atom is described by the Bloch vector $\boldsymbol{\rho}$ which rotates on a sphere in the uvw-space.

frequency is given by the magnitude of the torque vector, and is also known as the *generalised Rabi frequency*

$$\Omega = \sqrt{\chi^2 + \Delta^2}, \tag{2.50}$$

where $\chi = \kappa E_0$ is the resonant Rabi frequency. Thus, the rotation frequency will be lowest exactly on resonance, where the population oscillates between the ground and excited state. When the detuning increases, so does the frequency; however, for non-zero detuning, the population inversion is never complete, as illustrated in figure 2.4.

These oscillations are also known as *Rabi oscillations*, and the explicit Rabi solution of the optical Bloch equations is

$$\rho_{22} = \frac{\chi^2}{\Omega^2} \sin^2\left(\frac{\Omega t}{2}\right), \tag{2.51}$$

where the atom was assumed to start in the ground state at $t = 0$. From this expression, it is clear that the first population inversion occurs when $t\chi = \pi$, and a pulse of this duration is known as a π-pulse.

Another effect that can be seen in the Rabi solution, is *power broadening*. The spectral width of the resonance is set by the envelope χ^2/Ω^2, and since Ω is the vectorial sum of χ and Δ, the envelope reaches the value $1/2$ when $\Delta = \chi$. When the power is increased, so is χ, since it depends on the electric field strength. This leads to a wider spectrum, known as power broadening.

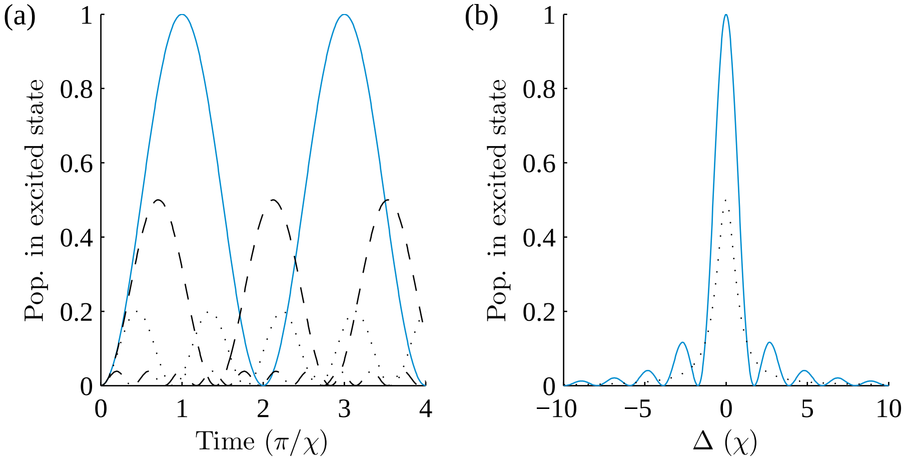

FIGURE 2.4: Rabi oscillations in a two-level system. *(a)* Rabi oscillations for $\Delta = 0$ (blue, solid), $\Delta = \chi$ (black, dashed), $\Delta = 2\chi$ (black, dotted), and $\Delta = 5\chi$ (black, dash-dotted). *(b)* Spectrum for a π-pulse (blue, solid) and for a dephased ensemble (black, dotted).

Losses may be taken into account by adding a phenomenological decay rate Γ to w and a transverse decay rate $\gamma_\perp$ to u and v. For natural broadening, the transverse decay rate takes the value of $\gamma_\perp = \Gamma/2$. With loss included, the equations (2.48) are known as the optical Blochs equations:

$$\begin{aligned}\dot{u} &= \Delta v - \tfrac{1}{2}\Gamma u \\ \dot{v} &= -\Delta u + \chi w - \tfrac{1}{2}\Gamma v \\ \dot{w} &= -\chi v - \Gamma(w-1).\end{aligned} \tag{2.52}$$

The solution to these more complicated differential equations are known as Torrey's solutions, and the general form of these solutions is [51]

$$\zeta(t) = Ae^{-at} + \left[B\cos(\Omega_\Gamma t) + \frac{C}{\Omega_\Gamma}\sin(\Omega_\Gamma t)\right]e^{-bt} + D, \tag{2.53}$$

where ζ is u, v or w; a and b are decay rates; Ω_Γ is the modified oscillation frequency, and A, B, C and D are constants determined by the variable represented by ζ and the initial conditions.

The parameters a, b and Ω_Γ depend only on physical quantities, and the general solution is very complicated. Exactly on resonance, the description becomes simpler, and the three lowercase constants are

$$a = \frac{\Gamma}{2}, \qquad b = \frac{3\Gamma}{4}, \qquad \Omega_\Gamma = \sqrt{\chi^2 - \left(\frac{\Gamma}{4}\right)^2}. \tag{2.54}$$

This shows that the oscillations occur at a slightly lower frequency similarly to a damped oscillator, and that the oscillation amplitude decays with a rate of $3\Gamma/4$. For w, the total solution assumes the form

$$w(t) = -1 + \frac{\Omega^2}{\Omega^2 + \Gamma^2/2}\left[1 - e^{-(3\Gamma/4)t}\left(\cos(\Omega_\Gamma t) + \frac{3\Gamma}{4\Omega_\Gamma}\sin(\Omega_\Gamma t)\right)\right]. \tag{2.55}$$

When the oscillation is completely decayed, the system is said to be *dephased*, since all coherence is lost. The spectral shape of such a pulse does not exhibit the side peaks as the π-pulse did; instead its shape is that of a Lorentzian,

$$L(\Delta) = \frac{\Gamma/2}{\Delta^2 + (\Gamma/2)^2}, \tag{2.56}$$

where Γ is the full width at half maximum (FWHM). The line shape is plotted in figure 2.4.

Resonant light: absorption imaging

Absorption imaging measures the cloud's density profile by using the shadow the cloud casts on a resonant laser beam. The principle is illustrated in figure 2.5: (a) When atoms absorb light, they leave shadows on the profile of the light. (b) Another image is taken without the atoms. (c) The images are divided to account for the structure of the beam profile, and the *optical density* is calculated. Although the clouds at the edges of the picture are barely visible in the raw image (a), they are clear in the optical density.

To obtain a clear shadow on the raw image, a large number of photons should be scattered out of the beam. To this end, a closed transition (i.e. one where atoms are not lost to optically dark states) is used, such that the atom may cycle on the transition many times. We shall assume a two-level atom, even though the structure of ^{87}Rb includes many more levels.

The two primary transitions in ^{87}Rb are the D1 and D2 lines. Figure 2.6 shows the energy level diagram of the D1 and D2 lines. We use the D2 transition because it provides the best approximation to a two-level system: The excited state contains four hyperfine manifolds, and for a closed transition, one may choose $F = 2 \longrightarrow F' = 3$, since the selection rules only allow decay back to $F = 2$.

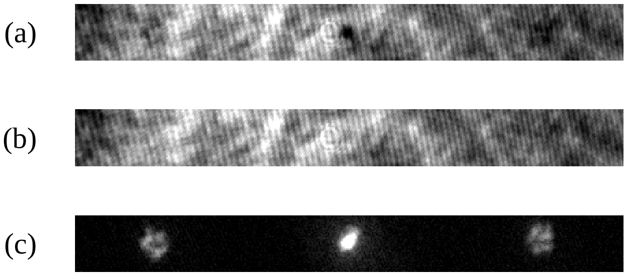

FIGURE 2.5: Principle of absorption imaging. *(a)* Raw image. Resonant light illuminates the atomic cloud leading to areas of reduced light intensity. *(b)* Beam image. An image of the beam is taken without atoms. *(c)* The two images are divided, and the optical density is calculated.

The natural linewidth of the D2 transition is 6.1 MHz [50], which is narrow compared to the spacing between the hyperfine manifolds of the excited state, $\sim 100\,\mathrm{MHz}$. Thus, if the light is resonant with the $F=2 \to F'=3$ transition, we can neglect other levels and approximate the system by a two-level atom.

To calculate the absorbed light, we use the optical Bloch equations. If Γ is the decay rate of the excited state, an atom will scatter photons with the rate

$$R_{\mathrm{sc}} = \Gamma \rho_{22}. \tag{2.57}$$

Using the relations (2.43), we may express ρ_{22} as $\frac{1}{2}(1-w)$.

Since we assume a large number of cycles we go to the steady state limit where the oscillation is fully decohered. We have the two equations

$$0 = \dot{u} - i\dot{v} = -(\tfrac{1}{2}\Gamma - i\Delta)(u - iv) + i\chi w \tag{2.58}$$

$$0 = \dot{w} = -\Gamma(w-1) - \chi v. \tag{2.59}$$

Solution of these equations leads to the expression

$$w = \frac{1}{1+s}, \tag{2.60}$$

where s is the saturation parameter

$$s = \frac{\chi^2/2}{\Gamma^2/4 + \Delta^2}. \tag{2.61}$$

Since χ^2 is proportional to the light intensity, the saturation parameter may be expressed as a saturation intensity I_{sat} yielding

$$s = \frac{I/I_{\mathrm{sat}}}{1 + (2\Delta/\Gamma)^2}. \tag{2.62}$$

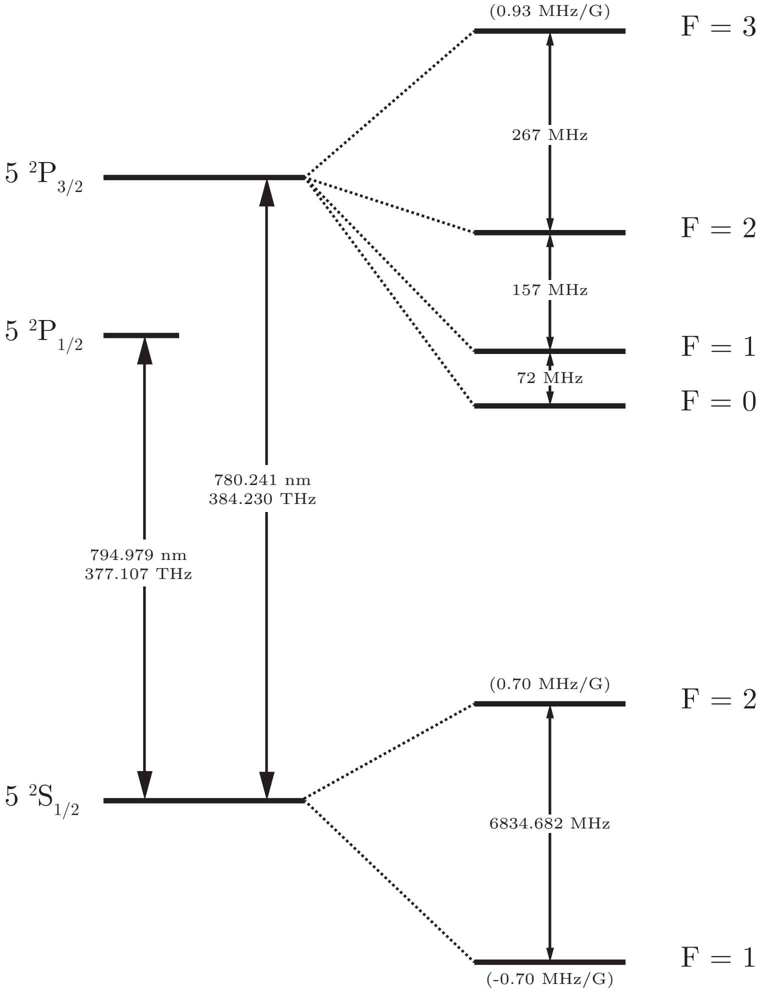

FIGURE 2.6: The level structure of the D2 transition of ^{87}Rb, $5\,^2S_{1/2} \rightarrow 5\,^2P_{3/2}$. The D1 transition, $5\,^2S_{1/2} \rightarrow 5\,^2P_{1/2}$ is shown for reference. The linear Zeeman shift is written in brackets; for the $P_{3/2}$ state, it is 0.93 MHz/G for all hyperfine states. Data is taken from [50].

Returning to the scattering rate, it is now possible to write the explicit expression

$$R_{\mathrm{sc}} = \Gamma \tfrac{1}{2}(1-w) = \frac{\Gamma s}{2(1+s)}. \tag{2.63}$$

Since scattering reduces the light intensity, the intensity will decrease at a rate proportional to the scattering rate. For now, we assume that the scattering depends linearly on the atomic density n, and that the energy scattered in a single scattering event is $\hbar\omega$. The intensity change after propagating a distance $\mathrm{d}z$ is $-\hbar\omega R_{\mathrm{sc}} n \mathrm{d}z$, leading to the differential equation

$$\frac{dI}{dz} = -\hbar\omega R_{\mathrm{sc}} n. \tag{2.64}$$

If we substitute the expression for R_{sc}, we obtain the equation

$$\frac{dI}{dz} = -\frac{\hbar\omega\Gamma n}{2} \frac{I/I_{\mathrm{sat}}}{1 + I/I_{\mathrm{sat}} + (2\Delta/\Gamma)^2}, \tag{2.65}$$

For resonant light, this reduces to

$$\frac{dI}{dz} = -\frac{\hbar\omega\Gamma n}{2} \frac{I/I_{\mathrm{sat}}}{1 + I/I_{\mathrm{sat}}}, \tag{2.66}$$

From basic atomic properties it is thus possible to calculate the saturation intensity and thereby the light absorption from a given atomic cloud. This is a well-established way of calculating the density of an atomic ensemble from an absorption image.

The validity of this method is, however, limited, since this model assumes that scattered photons are not reabsorbed, which is not necessarily the case for dense clouds. To include this effect and to model experimental complications such as impure light polarisation and the multi-level atomic structure, it is possible to introduce an *effective saturation intensity* $I_{\mathrm{sat}}^{\mathrm{eff}} = \alpha^* I_{\mathrm{sat}}$ characterised by the dimensionless constant α^* [52].

Using the expression for the absorption cross-section $\sigma_0 = \hbar\omega\Gamma/2I_{\mathrm{sat}}$, a new differential equation is obtained

$$\frac{dI}{dz} = -n\frac{\sigma_0}{\alpha^*} \frac{I}{1 + I/I_{\mathrm{sat}}^{\mathrm{eff}}}, \tag{2.67}$$

which is integrated over the length of the sample, yielding an expression for the optical depth

$$\mathrm{OD}_0 = \sigma_0 \int n\, dz = -\alpha^* \ln\left(\frac{I}{I_0}\right) + \frac{I_0 - I}{I_{\mathrm{sat}}}. \tag{2.68}$$

This shows that the effect of α^* reduces to a scaling between the optical density and the ratio of intensity to saturation intensity.

Since the optical density only depends on cloud properties, it must be independent of the imaging conditions. One can then find α^* by imaging the same cloud with different light intensities and afterwards evaluating the images with different values of α^*. The value that keeps OD_0 constant must be the correct value. We have performed such a calibration of our imaging systems, and it will be described in section 3.5.

Microwave interaction

The other type of resonant interaction that needs to be discussed, is the interaction with a field in the microwave region. Such a field may couple hyperfine states within the same fine state, such as the $F = 1 \rightarrow F' = 2$ in the $5\,{}^2\mathrm{S}_{1/2}$ state of ${}^{87}\mathrm{Rb}$ which has a transition frequency of 6.834682 GHz (see figure 2.6). The fact that the initial and final states have the same angular quantum number means that the parity cannot change as required by electronic dipole selection rules. The microwave transition is thus a *magnetic dipole transition*, which connects states of equal parity but otherwise obey the same selection rules [45].

Being a magnetic transition, the microwave interaction is much weaker than an electric dipole transition and very narrow in frequency[2]. This means, that the spectral width typically will be dominated by magnetic field noise through the Zeeman effect, or by the Fourier width of the microwave pulse.

Another important aspect of microwave transitions is that they generally are non-destructive as opposed to absorption imaging. This is easily seen by calculating the recoil velocity for the two transitions, $v_{\mathrm{rec}} = \hbar k/m$. For the D2 transition, this amounts to 5.89 mm/s, whereas a microwave photon of 6.834 GHz only inflicts 104 nm/s. Given the fact that the kinetic energy scales quadratically with velocity, the heating caused by microwave radiation is negligible.

Although the microwave interaction is a magnetic interaction, all the theory regarding the Bloch equations is applicable to this situation. In practice, however, microwave transitions are driven with a Rabi frequency typically in the kHz regime whereas optical transitions work in the MHz regime. So where absorption imaging worked in the dephased limit, we shall deal with the coherent aspects of microwave interaction.

---

[2] The magnetic dipole transition comes from the 2nd term in the expansion $e^{i\boldsymbol{k}\cdot\boldsymbol{r}} = 1 + i\boldsymbol{k}\cdot\boldsymbol{r} + \ldots$, where $\boldsymbol{k}$ is the wave vector of the light and $\boldsymbol{r}$ is the position of the electron. Thus, this transition will be weaker by a factor of ka, where a is the radius of the electron orbit. This typically amounts to a factor on the order of $\sim 10^{-3}$ [53, p. 405].

The microwave source may be used for state preparation by producing a π-pulse. This is only possible on resonance, so it is important that the resonance frequency is stable (through the Zeeman shift). Any change in magnetic field that happens on a time-scale slower than the microwave pulse appears as a “shot-to-shot” fluctuation, whereas changes on a time scale faster than the pulse amounts to a broadening of the resonance profile.

One way of dealing with ambient noise is to make the pulse spectrally broader through the Fourier width. The Fourier transform of a square pulse is the sinc function, and for a pulse of duration τ, the spectrum is

$$\operatorname{sinc}^2(\pi\tau\nu) = \left(\frac{\sin(\pi\tau\nu)}{\pi\tau\nu}\right)^2 \tag{2.69}$$

This function has characteristic wings of little side peaks that are spaced by $1/\tau$, and the central peak gets narrower with increasing τ as can be seen by finding the *half-width at half maximum* (HWHM):

$$\begin{aligned} \left(\frac{\sin(\pi\tau\nu)}{\pi\tau\nu}\right)^2 &= \tfrac{1}{2} \\ 1 - \tfrac{1}{3}(\pi\tau\nu)^2 &\simeq \tfrac{1}{2} \\ \nu &\simeq \frac{\sqrt{3/2}}{\tau\pi}, \end{aligned} \tag{2.70}$$

where the Taylor expansion of sinc was applied. This means that a very short pulse has a very broad spectrum and that it cannot resolve the shift of the resonance due to magnetic noise. A short π-pulse obviously requires a large Rabi frequency, which in turn requires a large field amplitude; so to exploit the Fourier width, high microwave power is needed.

Another approach to state preparation is rapid adiabatic passage. Here, the frequency of the microwave is swept across a resonance, starting and ending in the far-detuned regime. This approach is often used for RF interactions coupling m_F states in the same manifold [54], since it is easier to keep coherence at the lower frequency. We have not used microwave sweeps for state preparation, since the pulses are very stable, but sweeps are very efficient for localising the resonance frequency of a microwave transition.

Polarisability tensor

To describe off-resonant interactions, and in particular the effect of atom-light interactions on the light, we introduce a more general model. Here, the light is described in quantised fashion, and the multi-level structure of the atom is taken into account.

First, we let the polarisation state of the light be described by the *Stokes vector* $\hat{\mathbf{S}} = \left(\hat{S}_0, \hat{S}_x, \hat{S}_y, \hat{S}_z\right)^{\mathsf{T}}$ [55]. This formalism is an extension of the simpler Jones vector, and it is superior in that it allows for partial polarisation of the light. In that respect, it is very similar to the density matrix description of an atom.

After quantising the field, the components of $\hat{\mathbf{S}}$ are operators of the electrical field, given by

$$\begin{aligned}
\hat{S}_0 &= \tfrac{1}{2}\left(\hat{N}_{\mathrm{ph},x} + \hat{N}_{\mathrm{ph},y}\right),\\
\hat{S}_x &= \tfrac{1}{2}\left(\hat{N}_{\mathrm{ph},y} - \hat{N}_{\mathrm{ph},x}\right),\\
\hat{S}_y &= \tfrac{1}{2}\left(\hat{N}_{\mathrm{ph},135^\circ} - \hat{N}_{\mathrm{ph},45^\circ}\right),\\
\hat{S}_z &= \tfrac{1}{2}\left(\hat{N}_{\mathrm{ph},\sigma+} - \hat{N}_{\mathrm{ph},\sigma-}\right),
\end{aligned} \tag{2.71}$$

where $\hat{N}_{\mathrm{ph},\lambda}$ is the photon number operator for the polarisation λ. Each of the Stokes operators obeys the canonical commutation relation

$$\left[\hat{S}_i, \hat{S}_j\right] = i\epsilon_{ijk}\hat{S}_k. \tag{2.72}$$

This formalism allows for a full quantum description of both the atom and the light, and also incorporates the polarisation state of the light. This is crucial for the description of the Faraday effect which will be discussed later in this section.

Secondly, let the atom be described in the hyperfine basis $|F, m_F\rangle$. We consider a transition from the F to the F' manifold, each with a state multiplicity of $2F+1$ and $2F'+1$. The light driving this transition is oscillating at an angular frequency of ω and it is incident along the z-axis.

For this fully quantised description, the interaction Hamiltonian takes a more complicated form. The interaction is now described by a *polarisability tensor* $\alpha_{\mu\nu}$, which takes into account transitions between different m_F states in the atom and corresponding evolution in positive and negative rotating components of the electric field [56].

We shall be interested in the polarisability tensor for off-resonant light, and this allows us to neglect population in the excited states. These are then *adiabatically eliminated* such that the interaction is only described in terms of the ground states [57]. Without going into details, the interaction Hamiltonian can be decomposed into the irreducible parts [58]

$$\hat{H}_{\mathrm{int}} = \tfrac{1}{3} g\alpha^{(0)}\hat{N}_{\mathrm{ph}}\hat{N}_{\mathrm{at}} + g\alpha^{(1)}\hat{S}_z\hat{F}_z + \hat{H}^{(2)}, \tag{2.73}$$

where $g = \omega/2\epsilon_0 V$, V is the volume of the illuminated sample, $\alpha^{(0)}$ and $\alpha^{(1)}$ are the scalar and vector polarisabilities respectively, and F_z is the z-component of the total angular momentum. $H^{(2)}$ is the tensor interaction, which will not be discussed in this thesis.

The general form of any of the polarisability is a linear combination of couplings between the different hyperfine states F and F'

$$\alpha^{(i)} = \alpha_0 \sum_{F,F'} a_F^{F'} \frac{\Delta_{FF'}}{\Delta_{FF'}^2 + \Gamma^2/4} \tag{2.74}$$

where $\Delta_{FF'} = \omega - \omega_{FF'}$ is the detuning from a resonance, $\alpha_0 = 3\epsilon_0 \hbar \Gamma \lambda^3 / 8\pi^2$ is the classical polarisability, Γ is the decay rate, and $a_F^{F'}$ is coupling constant that depends on the Wigner 6-j coefficients [56, 58].

Equation (2.74) is basically the classical polarisability scaled with a factor that depends on the "geometry" of angular momentum. Still, this is a very general model, and to make it more tractable, we shall make further approximations in the following section.

Faraday effect: Vector polarisability

Going to a far detuned regime, we return to equation (2.73). In the region of large detuning, the tensor term drops out [58]. In this context, large detuning is with respect to the hyperfine states of the F' manifold. For the D2 transition of ^{87}Rb, the hyperfine splitting of the excited state is around 200-300 MHz (see figure 2.6), so with a detuning of $\sim 1\,$GHz, we can safely neglect the tensor term.

It is worth noting that this effect is due to the symmetry of the Wigner 6-j coefficients [56, 58]. The single valence electron causes a balance in the coefficients, and this cancellation is thus a common phenomenon in alkali atoms.

The two remaining terms in equation (2.73) have qualitatively different effects on light interacting with an atomic ensemble. The scalar term depends on the total number of photons, and it will only add a global phase to the light. The vector term, however, depends on $\hat{S}_z = \frac{1}{2}(\hat{N}_{\mathrm{ph},\sigma^+} - \hat{N}_{\mathrm{ph},\sigma^-})$ which gives a differential phase to the two circular light states. It is therefore sufficient to focus on the vector term for the rest of this section

$$\hat{H}_{\mathrm{int}} = g\alpha^{(1)} \hat{S}_z \hat{F}_z = \frac{g}{2} \alpha^{(1)} \langle \hat{F}_z \rangle \big(\hat{N}_{\mathrm{ph},\sigma^+} - \hat{N}_{\mathrm{ph},\sigma^-} \big). \tag{2.75}$$

Here, we have approximated the operator $\hat{F}_z$ with its expectation value, which is a good approximation for large ensembles. That this differential light shift is equivalent to a rotation of the polarisation plane will become apparent when we apply

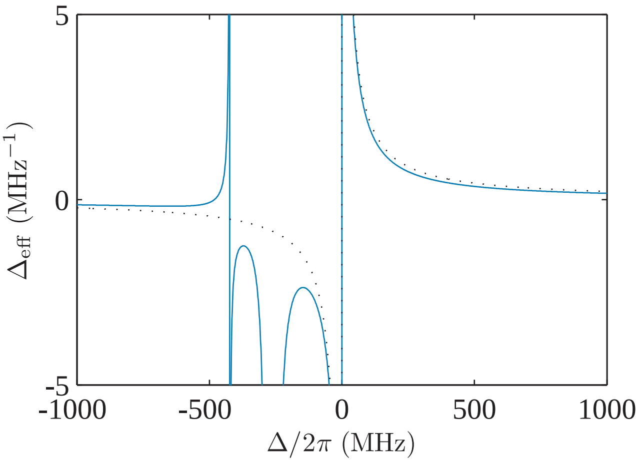

FIGURE 2.7: The effective detuning (solid blue) and the approximated detuning (dotted black). The transition $F = 2 \rightarrow F' = 3$ is set to zero detuning, which is the convention used in this thesis.

the Heisenberg equation of motion to the Stokes components. First, the explicit expression for $\alpha^{(1)}$ needs to be found, and we focus on the experimentally relevant case of the $F = 2 \rightarrow F' = 3$ transition on the D2 line of ^{87}Rb.

In the far detuned regime, $\Delta_{FF'} \gg \Gamma/2$, the frequency dependence of each term in the polarisability (2.74) simply reduces to $1/\Delta_{FF'}$, and if the detuning is larger than the excited state hyperfine splitting, then it is a good approximation to only use the nearest resonance. This reduces the polarisability to [58]

$$\alpha^{(1)} = -\frac{1}{3}\frac{\alpha_0}{\Delta} \tag{2.76}$$

for the $F = 2$ manifold. For more accurate results, one may simply collect the different terms in an effective detuning Δ_{eff} [59]

$$\frac{1}{\Delta_{\text{eff}}} = \frac{1}{20}\left(\frac{28}{\Delta_{2,3}} - \frac{5}{\Delta_{2,2}} - \frac{3}{\Delta_{2,1}}\right), \tag{2.77}$$

where $\Delta_{f,f'} = \omega_f - \omega_{f'}$. See figure 2.7 for a plot of $1/\Delta_{\text{eff}}$ and $1/\Delta$.

The interaction Hamiltonian now takes the form $\hat{H}_{\text{int}} = \frac{c}{\Delta}\langle\hat{F}_z\rangle\hat{S}_z$, where c is a constant given by equation (2.76). We now apply the Heisenberg equation of motion to the Stokes operators

$$\frac{\partial \hat{S}_j}{\partial t} = \frac{1}{i\hbar}\left[\hat{S}_j, \hat{H}_{\text{int}}\right]. \tag{2.78}$$

Using the commutator relations for the Stokes operators, this yields the coupled equations

$$\frac{\partial \hat{S}_x}{\partial t} = \frac{c}{h\Delta}\langle \hat{F}_z\rangle \hat{S}_y \tag{2.79a}$$

$$\frac{\partial \hat{S}_y}{\partial t} = -\frac{c}{h\Delta}\langle \hat{F}_z\rangle \hat{S}_x \tag{2.79b}$$

$$\frac{\partial \hat{S}_z}{\partial t} = 0. \tag{2.79c}$$

This system of equations describes rotation of the x- and y-components around the z-axis, which can be made explicit by taking the derivative of equation (2.79a) and substituting it into equation (2.79b)

$$\frac{\partial^2 \hat{S}_x}{\partial t^2} = -\left(\frac{c}{\hbar\Delta}\langle \hat{F}_z\rangle\right)^2 \hat{S}_x = -\omega_S^2 \hat{S}_x \tag{2.80}$$

The Stokes vector will thus rotate with angular frequency ω_s, which means that the electric field will rotate at half that frequency[3]. If we assume the cloud to consist only of atoms in a single m_F state, we may approximate the expectation value of $\hat{F}_z$ by N_{at} times the single-particle value $\langle \hat{f}_z\rangle$. This leads to an expression for the Faraday angle

$$\theta_{\mathrm{F}} = \tfrac{1}{2}\omega_S \tau = \frac{\Gamma\lambda^2 L\langle f_z\rangle}{16\pi}\frac{n}{\Delta}, \tag{2.81}$$

where $\tau = L/c$, and L is the length of the sample. This exhibits the $1/\Delta$ dependence that is typical for all dispersive imaging techniques, and a linear dependence on the atomic density. In other words, the rotation angle provides a measure for the number of atoms.

If the light is imaged on a camera, we may make take θ_{F} as a function of x and y, which turns equation (2.81) into

$$\theta_{\mathrm{F}}(x,y) = \frac{\Gamma\lambda^2\langle f_z\rangle}{16\pi}\frac{\int n(\boldsymbol{r})dz}{\Delta}. \tag{2.82}$$

It is thus possible to extract the column density from the Faraday angle yielding an image of the in-trap cloud.

The Faraday rotation in equation (2.82) may be used for non-destructive imaging by sending linearly polarised light onto the atomic sample and then splitting

---

[3] This can qualitatively be seen through the fact that the Stokes vector only contains terms of order $\hat{N}_{\mathrm{ph}}$ which classically corresponds to $\hat{E}^2$.

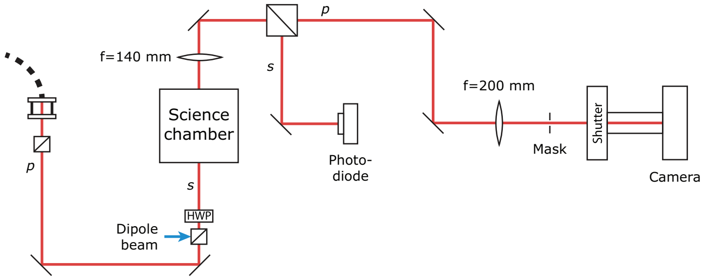

FIGURE 2.8: Faraday imaging setup. Polarisations are indicated in italics. The off-resonant light is combined with the absorption imaging light for the z axis before the fibre. The imaging light is combined with the light from the optical dipole trap on a polarising beam splitter before the chamber. The light is s polarised before the chamber, so without Faraday rotation, all light will be split off in the large polarising beam splitter and sent to the photodiode.

the non-rotated light away on a polarising beam-splitting cube as illustrated in figure 2.8. The non-ideal behaviour of the cube and the ellipticity of the polarisation is quantified by the *cube suppression* $\mathrm{CS} = I(0)/I(\pi/2)$, and this yields the transmitted light intensity

$$I(\theta_\mathrm{F}) = I_0 \frac{\sin^2(\theta_\mathrm{F}) + \mathrm{CS}\cos^2(\theta_\mathrm{F})}{1+\mathrm{CS}}. \tag{2.83}$$

We have measured the cube suppression to be $\mathrm{CS} \approx 1.5 \times 10^{-3}$ from the intensity after the cube. Since CS is small, we may neglect all terms of second order in CS. This leads to an expression for the Faraday angle

$$\sin^2(\theta_\mathrm{F}) = \left(\frac{I(\theta_\mathrm{F})}{I(0)} - 1\right)\left(\frac{\mathrm{CS}}{1-\mathrm{CS}}\right), \tag{2.84}$$

where we have defined $I_0\mathrm{CS} \equiv I(0)$. The light leaking through the cube causes the subtraction of 1, and this sets the detection limit for low light intensities. Our cube suppression of 1.5×10^{-3} amounts to a measurable reduction in signal-to-noise ratio only for rotation angles smaller than 5° [59].

The destructiveness of the imaging method is quantified by the number of photons scattered by the atoms. Absorption effects were neglected in the derivation of the Hamiltonian due to the adiabatic elimination of excited state population. However, the scattering rate may be calculated in a non-rigorous way as in the case of absorption imaging. This amounts to taking the imaginary part of the polarisability, and the resulting scattering rate is identical to (2.63)

$$R_{\mathrm{sc}} = \frac{\Gamma}{2} \frac{I/I_{\mathrm{sat}}}{I/I_{\mathrm{sat}} + 1(2\Delta/\Gamma)^2}. \tag{2.85}$$

In the limit of far detuning, $(2\Delta/\Gamma)^2 \gg 1$, $(2\Delta/\Gamma)^2 \gg I/I_{\mathrm{sat}}$, the expression reduces to

$$R_{\mathrm{sc}} = \frac{\Gamma^3}{8I_{\mathrm{sat}}} \frac{I}{\Delta^2}. \tag{2.86}$$

This shows that the scattering rate scales as $1/\Delta^2$ whereas the signal, equation (2.81) scales as $1/\Delta$. This makes it profitable to go to the far detuned regime, since the destructive properties will be suppressed compared to the signal.

Optical dipole force: Scalar polarisability

We now focus on the further detuned regime. If the detuning of linearly polarised light is large compared to the fine structure, then the symmetry of the Wigner 6-j symbols makes the vector term of the polarisability vanish [56]. This leaves only the scalar term in the interaction Hamiltonian. For ^{87}Rb, this means that the detuning must be large compared to the difference between the D1 and D2 line, $\Delta \gg \Delta E_{\mathrm{fs}}$. This energy difference is $\sim 7\,\mathrm{THz}$, whereas a laser of 914 nm is detuned by $\sim 50\,\mathrm{THz}$ from the D1 line (see figure 2.6).

To evaluate the effect of the polarisability in this regime, we shall apply a slightly different approach. If we are not interested in the polarisation states of the light, we may use a semiclassical approach and calculate the perturbation caused by the light. We assume the light to have the electric field polarised along z and to oscillate with the frequency ω. In the dipole approximation, the perturbing Hamiltonian is

$$\hat{H}' = -\hat{d}_z \mathscr{E}_0 \cos(\omega t) = -\tfrac{1}{2} \hat{d}_z \mathscr{E}_0 \left(e^{i\omega t} + e^{-i\omega t}\right) \tag{2.87}$$

We evaluate the perturbation to 2nd order, and assume that at time $t = 0$, the system is in an eigenstate $|m\rangle$ of the unperturbed Hamiltonian, when the interaction is activated. If we designate the phase of the state $|m\rangle$ by ϕ_m, we may calculate the time derivative of the phase to 2nd order as[4]

$$\hbar \dot{\phi}_m = \frac{\mathscr{E}_0^2}{2\hbar} \sum_{n \neq m} \left|\langle m|\hat{d}_z|n\rangle\right|^2 \cos(\omega t) \left(\frac{e^{i\omega t} - e^{-i\omega_{nm} t}}{\omega_{nm} + \omega} + \frac{e^{-i\omega t} - e^{i\omega_{nm} t}}{\omega_{nm} - \omega} \right), \tag{2.88}$$

---

[4] The calculation is detailed in [44], section 3.3.

where ω_{nm} is the Bohr frequency between the states $|n\rangle$ and $|m\rangle$. To obtain the energy shift of $|m\rangle$, we identify the time average of $\dot{\phi}_m$ as the Bohr frequency. We take $\Delta E_m = -\hbar\langle\dot{\phi}\rangle$, and if we write the cosine as complex exponentials, only a single term has a finite contribution when averaging

$$\Delta E_m = -\frac{\mathcal{E}_0^2}{4\hbar}\sum_{n\neq m}\left|\langle m|\hat{d}_z|n\rangle\right|^2\left(\frac{1}{\omega_{nm}+\omega}+\frac{1}{\omega_{nm}-\omega}\right), \tag{2.89}$$

This result is very general, but it may be made slightly simpler through the *rotating wave approximation* (RWA). If the light is only slightly detuned from the atomic transitions, the term containing $\omega_{nm}+\omega$ will be much smaller than the one containing $\omega_{nm}-\omega$. We may thus neglect the former term. Introducing the light intensity $I = \frac{1}{2}c\epsilon_0\mathcal{E}_0^2$, we have

$$\Delta E_m = \frac{I}{2\hbar c\epsilon_0}\sum_{n\neq m}\left|\langle m|\hat{d}_z|n\rangle\right|^2\frac{1}{\omega-\omega_{nm}}. \tag{2.90}$$

For a two-level system, this expression leads to an attractive potential for red detunings ($\omega < \omega_{nm}$) and a repulsive potential for blue detunings ($\omega > \omega_{nm}$), which is the basic principle of optical trapping. For the excited state, the Bohr frequency ω_{nm} in equation (2.89) changes sign, leading to an overall change of sign, when performing the RWA. Thus, the effect on the excited state is just the opposite of that for the ground state; when the ground state is lowered in energy, the excited state is raised in energy and vice versa (see figure 2.9)

To take both of the D lines into account (see figure 2.6 on page 26), one uses the Wigner-Eckart theorem to simplify the matrix element. The theorem states, that a matrix element involving angular momentum states may be split into Clebsch-Gordan coefficient that only depends on the coupling of angular momenta and a reduced matrix element $\langle m||\hat{d}_z||n\rangle$ that is independent of the angular momenta [60].

The result of this is to introduce a line strength that is given by the Clebsch-Gordan coefficients, and when the matrix element is eliminated by the introduction of the natural linewidth Γ_{nm}, [50]

$$\Gamma_{nm} = \left|\langle m||\hat{d}_z||n\rangle\right|^2\frac{\omega_{nm}^3}{3\pi\epsilon_0\hbar c^3}, \tag{2.91}$$

we obtain the full expression

$$U_{\text{dip}}(\boldsymbol{r}) = \frac{\pi c^2}{2}\left(\frac{2\Gamma_2}{\omega_2^3\Delta_2}+\frac{\Gamma_1}{\omega_1^3\Delta_1}\right)I(\boldsymbol{r}), \tag{2.92}$$

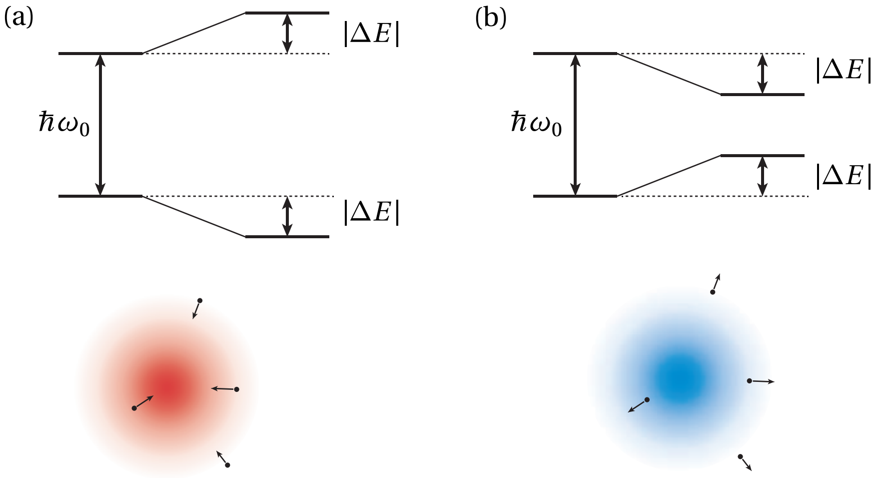

FIGURE 2.9: The effect of a light shift for *(a)* red detuning, *(b)* blue detuning. For each case, the spatial effect on atoms in the ground state is sketched.

where $\Delta_i = \omega - \omega_i$ is the detuning from the D1 and D2 lines and Γ_i is the natural linewidth of the transition. The factor of two for the D2 line is the line strength of the transition, and originates from the fact that the excited state has twice the number of F manifolds that the D1 line has.

In equation (2.91) linearly polarised light is assumed. Circularly polarised light can also be taken into account by an extra term for the D1 and D2 lines. This yields a differential light shift for the m_F states [61].

2.5 Optical traps

Trap properties

The optical dipole force that was discussed in section 2.4 on page 35 may be used to generate a trapping potential called an optical dipole trap. Equation (2.92) shows that the trap potential is proportional to the light intensity, and the simplest experimental realisation is to confine atoms in a single red-detuned beam. A typical light beam will have a Gaussian shape [62]

$$I(r,z) = I_0 e^{-2r^2/w(z)^2}, \tag{2.93}$$

for a beam propagating along z. Here, r is the transverse coordinate, I_0 is the peak intensity, and $w(z)$ is the e^{-2} radius called the *spot size*. For a standard beam of

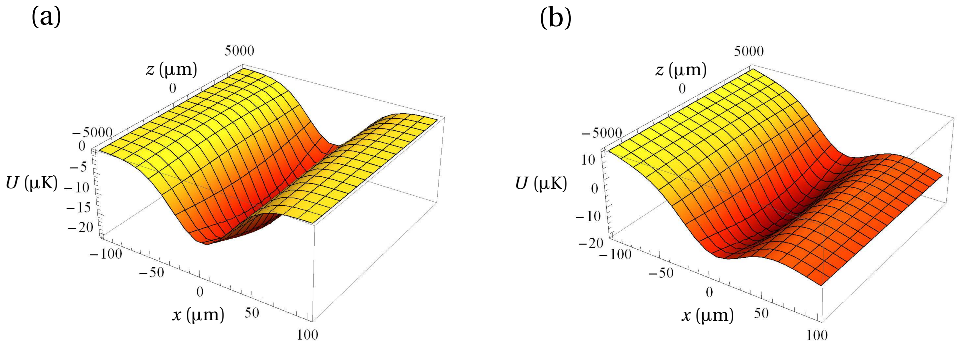

FIGURE 2.10: Dipole trap potentials. *(a)* Typical dipole trap potential without gravity. Notice the difference in scales along x and z which makes the Rayleigh range envelope visible. *(b)* Same dipole potential, but with gravity added along x.

power P and minimal spot size w_0 – called the *beam waist* – the peak intensity is $I_0 = 2P/\pi w_0^2$, and the spot size varies with z as

$$w(z) = w_0\sqrt{1 + z^2/z_0^2}, \tag{2.94}$$

where $z_0 = \pi w_o^2/\lambda$ is the Rayleigh length. It is clear that the transverse size is given by the spot size whereas the longitudinal size is given by the Rayleigh length, which makes the confinement much tighter transversely (figure 2.10). This has an effect when gravity is taken into account, and if a dipole trap is too weak, gravity may reduce the effective trap depth to the point, where it cannot hold any particles (figure 2.10 (b)).

A more sophisticated trap can be created by retro-reflecting the light beam, such that the light interferes with itself and creates a standing light wave. This adds a longitudinal interference factor to equation (2.93)

$$I(r,z) = \frac{8P}{\pi w(z)^2} e^{-2r^2/w(z)^2} \cos^2(kz), \tag{2.95}$$

where the additional factor of 4 comes from the interference of the electric fields, and k is the wave number. Here, the transverse confinement is still given by the spot size, but the longitudinal confinement is set by the wavelength, which is several orders of magnitude smaller than typical Rayleigh ranges. This makes a vertical lattice very effective for holding atoms against gravity.

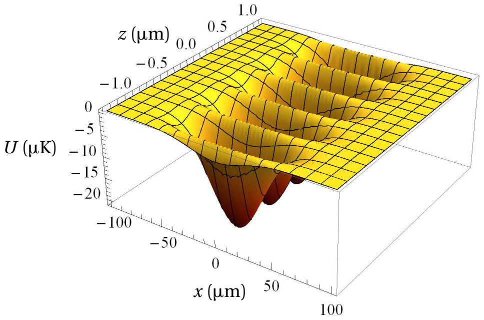

FIGURE 2.11: Optical lattice potential. The interference creates the longitudinal structure, whereas the transverse structure is given by the Gaussian profile of the laser beams. Notice the difference in scale along x and z.

The trap potential from an optical lattice may then be calculated by inserting equation (2.95) into equation (2.92). The maximum potential – and hence the trap depth – is then given by

$$V_0 = \frac{8P}{w(z)^2}\frac{c^2}{2}\left(\frac{2\Gamma_2}{\omega_2^3\Delta_2} + \frac{\Gamma_1}{\omega_1^3\Delta_1}\right). \tag{2.96}$$

Typically, one defines the s parameter in terms of the recoil energy $E_\mathrm{r} = \hbar^2 k^2/2M$

$$s \equiv \frac{V_0}{E_\mathrm{r}}. \tag{2.97}$$

This is a dimensionless parameter used to quantify the trap depth.

The tightness of the trap may be quantified by the trapping frequencies ω_i, which comes from a quadratic expansion of the trap potential at the bottom of the trap. For a single, cylindrically symmetric dipole beam, the potential is characterised by two trap frequencies: a radial frequency ω_r and an axial frequency ω_z. The expansion of equation (2.93) combined with equation (2.92) yields

$$U(r,z) \simeq -V_0^{\mathrm{dip}}\left[1 - 2\left(\frac{r}{w_0}\right)^2 - \left(\frac{z}{z_0}\right)^2\right], \tag{2.98}$$

where $V_0^{\mathrm{dip}} = V_0/4$. Equating the quadratic terms with a single-particle harmonic oscillator produces the expressions for the trapping frequencies

$$\begin{aligned}\omega_r^{\text{dip}} &= \sqrt{\frac{4V_0^{\text{dip}}}{Mw_0^2}},\\ \omega_z^{\text{dip}} &= \sqrt{\frac{2V_0^{\text{dip}}}{Mz_0^2}}.\end{aligned} \tag{2.99}$$

The radial frequency ω_r^{dip} is typically on the order of 10–100 Hz, and since z_0 typically is several orders of magnitude larger that w_0, the axial trapping frequency ω_z^{dip} will be negligible.

For an optical lattice, the expansion has an additional term

$$U(r,z) \simeq -V_0\left[1-2\left(\frac{r}{w_0}\right)^2-\left(\frac{1}{z_0^2}+k^2\right)z^2\right], \tag{2.100}$$

where k is the wave number of the lattice. Here, the $1/z_0$ term may safely be neglected, which leads to the trapping frequencies

$$\begin{aligned}\omega_r &= \sqrt{\frac{4V_0}{M}}w_0^{-1} = \sqrt{2s}\frac{\hbar k}{Mw_0},\\ \omega_z &= \sqrt{\frac{2V_0}{M}}k = \sqrt{s}\frac{\hbar k^2}{M}.\end{aligned} \tag{2.101}$$

It is clear that since k typically is much larger than w_0^{-1}, the axial trapping frequency will be very large for an optical lattice – usually in the kHz regime. For a deep optical lattice, the trapping frequency is so large, that the particle will only be in the ground state along this direction, and hence the motion is "frozen out" along the lattice.

Band structure

Apart from the trapping properties, optical lattices are interesting, because they set up a periodic potential. Such potentials are well-known in solid state physics, and they lead to the formation of energy bands.

To describe an atom in an optical lattice, we use the Schrödinger equation in one dimension

$$\frac{-\hbar^2}{2M}\frac{d^2}{dx^2}\psi(x)+V_0\cos^2(kx)\psi(x)=E\psi(x), \tag{2.102}$$

where an infinite lattice is assumed. In practice, the structure will be modified by the Gaussian profile of the laser beam, but we shall ignore this effect for now.

Bloch's theorem states that the solution to equation (2.102) can be described as a product state of a plane wave and a function u with the same periodicity as the lattice [63]

$$\phi_q^{(n)}(x) = e^{iqx/\hbar} u_q^{(n)}(x), \tag{2.103}$$

where n is the band index. Using equation (2.103) as ansatz and working in units of E_r, we obtain the differential equation

$$\begin{aligned} -\frac{1}{k^2}\left[\frac{q^2}{\hbar^2} u_q^{(n)}(x) - \frac{2iq}{\hbar}\frac{du_q^{(n)}}{dx} + \frac{d^2u_q^{(n)}}{dx^2}\right] & \\ + s\cos^2(kx)\, u_q^{(n)}(x) = \epsilon_q^{(n)} u_q^{(n)}(x), & \qquad (2.104) \end{aligned}$$

where $\epsilon_q^{(n)} \equiv E_q^{(n)}/E_\mathrm{r}$. Rewriting $s\cos^2(kx)$ in terms of exponentials yields

$$\begin{aligned} -\frac{1}{k^2}\left[-\frac{q^2}{\hbar^2} u_q^{(n)}(x) + \frac{2iq}{\hbar}\frac{du_q^{(n)}}{dx} + \frac{d^2u_q^{(n)}}{dx^2}\right] & \\ + \frac{s}{2}\left(1 + \frac{1}{2}e^{2ikx} + \frac{1}{2}e^{-2ikx}\right) u_q^{(n)}(x) = \epsilon_q^{(n)} u_q^{(n)}(x), & \qquad (2.105) \end{aligned}$$

and it is now obvious to also expand $u_q^{(n)}$ in exponentials

$$u_q^{(n)}(x) = \sum_{l=-\infty}^{\infty} c_{l,q}^{(n)} e^{i2lkx}. \tag{2.106}$$

The combination of equation (2.105) and (2.106) defines a matrix equation in terms of exponentials of all orders. The matrix elements are seen to be

$$H_{l,l'} = \begin{cases} (2l + q/\hbar k)^2 + s/2, & l' = l \\ -s/4, & l' = l \pm 1 \\ 0 & \text{otherwise} \end{cases} \tag{2.107}$$

The situation is then described by the equation

$$\sum_l H_{l,l'} c_{q,l}^{(n)} = \epsilon_q^{(n)} c_{q,l'}^{(n)}, \tag{2.108}$$

and the problem reduces to diagonalising the matrix $\boldsymbol{H}$. This is typically done by truncating l symmetrically around 0, e.g. $l = -L, -L+1, \ldots, L$. Such a matrix has

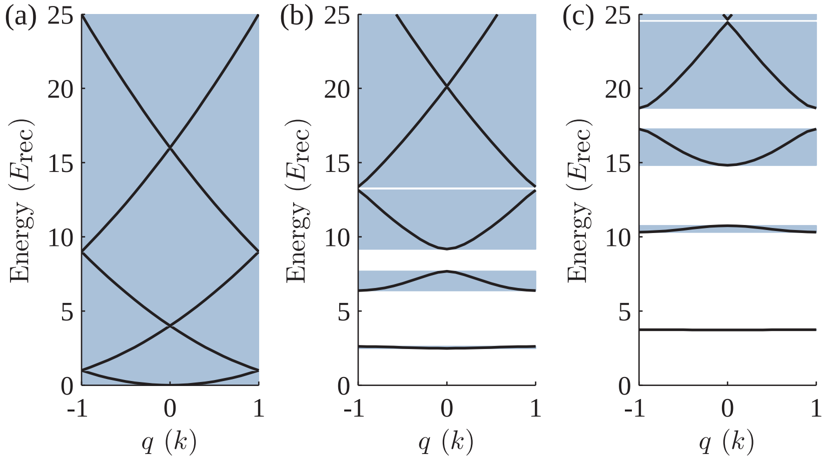

FIGURE 2.12: Bloch bands of an optical lattice at different values of s. *(a)* $s = 0$, dispersion is identical to that of free space. *(b)* $s = 8$, band gaps open. *(c)* $s = 16$, curvature of lowest band is negligible.

$2L+1$ eigenstates which are called Bloch bands, and they are normally identified by the index $n = 0, 1, \ldots, 2L+1$, starting from the ground state.

The band structure is shown in figure 2.12 for different values of s. For vanishing s, the dispersion approaches that of free-space, but as the lattice potential is increased, the dispersion splits into bands and band gaps. The width of the bands decreases with increasing potential, making the dispersion approximately flat for the lowest states at large values of s.

The curvature of the bands also has an impact on the motion of the particles. In general, the group velocity is given by $d\omega/dk$ which can be written as [63]

$$v_{\rm g} = \frac{1}{\hbar}\frac{dE(k)}{dk}. \tag{2.109}$$

Thus, the velocity is given by the slope of the band, which indicates that particles in the lowest band of a deep lattice will be static, as one would expect. On the other hand, a particle in a nearly unbound band will be able to oscillate by following the dispersion curve.

The states corresponding to the Bloch bands are called *Bloch functions*. They are given by the eigenvectors of the Hamiltonian as

$$\phi_q^{(n)}(x) = e^{iqx/\hbar}\sum_l c_{l,q}^{(n)} e^{i2lkx}. \tag{2.110}$$

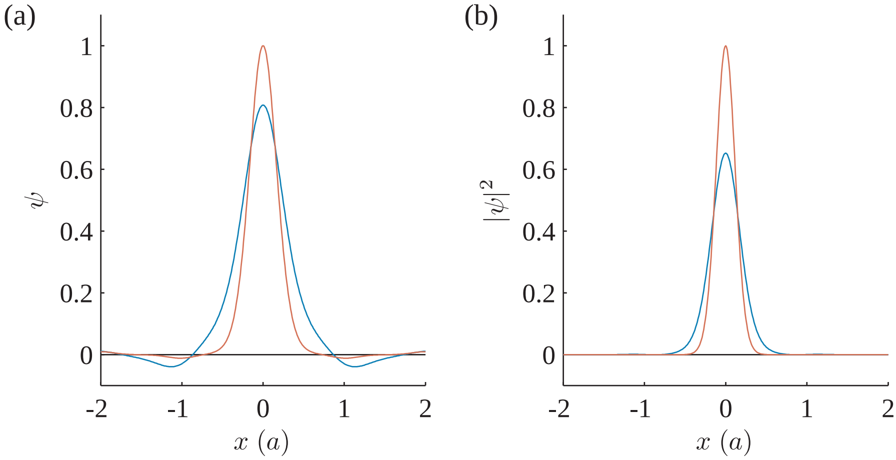

FIGURE 2.13: Wannier states in an optical lattice. *(a)* Wave function at $s = 4$ (blue) and at $s = 16$ (red). *(b)* Probability density for $s = 4$ (blue) and at $s = 16$ (red).

The periodic nature of the Bloch functions makes them completely delocalised over the lattice. Therefore, they are less useful for describing systems where localisation is significant. For such a system, the Wannier functions are more useful [64]

$$\psi_{\mathrm{W}}^{(n)}(x - x_i) = C \sum_q e^{iqx_i/\hbar} \phi_q^{(n)}(x), \tag{2.111}$$

where C is a normalisation constant. This describes a particle that is localised at the ith lattice site with position x_i, and it is basically the Fourier transform of the Bloch states. The localisation of the Wannier states is illustrated in figure 2.13 for two different values of s. At low lattice potential, there is a significant overlap of the wave function with the neighbouring site, but for a high lattice potential this overlap decreases.

Atoms localised in a lattice structure are well described in the basis of Wannier states as in the Bose-Hubbard model. The tunnelling rate J used in the model is related to the width of the band as [65]

$$J = \tfrac{1}{4}\left(\max\left(\epsilon_q^{(0)}\right) - \min\left(\epsilon_q^{(0)}\right)\right). \tag{2.112}$$

Thus, the tunnelling rate may be determined from a band structure calculation.

Transitions between lattice bands can be induced by modulating the amplitude of the lattice potential. A sinusoidal modulation can be thought of as a phonon in the lattice, and the atoms may absorb such a phonon to undergo a band

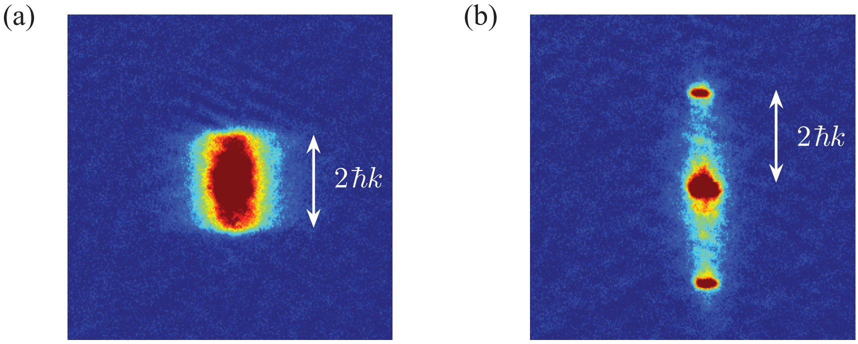

FIGURE 2.14: Lattice ramp-down methods. *(a)* Band mapping. The atoms in the lowest band fill up the 1st Brillouin zone, which leads to the width of $2\hbar k\tau/m$, where τ is the time-of-flight. *(b)* Projection. The lowest band is projected onto the free-space momentum, and has a large population in multiples $0, \pm 2$ of the lattice momentum

excitation. The optical potential may be described by

$$V = s E_{\mathrm{r}} \cos^2\left(k y\right)[1+\epsilon \cos(2\pi \nu t)], \tag{2.113}$$

where ϵ is the relative amplitude and ν is the frequency of the modulation.

The matrix element connecting two states in different bands is determined by $\cos^2\left(k y\right)$ which has even parity. This leads to the selection rule $\Delta n = 2$ to lowest order. Thus the amplitude modulation can only excite atoms in the 0th band to the 2nd band, and the resonance criterion is $\nu = 2\,\nu_{\mathrm{trap}}$, in accordance with parametric excitation.

Loading techniques

When transferring a BEC to an optical lattice, the free-space momentum $\hbar k$ is transformed to the lattice basis of quasi-momenta $\hbar q$. To go from the free-space ground state to the lattice ground state, one needs to perform the basis change adiabatically with respect to the timescale set by the lattice.

There are, in general, two relevant time scales, corresponding to two different energy scales. Violation of these time-constraints leads to two different non-adiabatic phenomena:

- *The single-site energy.* This energy is set by the band gap, and violation of this will cause population of higher bands when loading the lattice. The criterion for adiabaticity is [66]

$$\left| \langle 1, q | \frac{\partial H}{\partial t} | 0, q \rangle \right| \ll \Delta E^2 \big(q, t \big) / \hbar, \tag{2.114}$$

where $|n, q\rangle$ is a Bloch state, and ΔE is the energy difference between the ground state and the first excited state. For $q \approx 0$, this is easy to achieve, since the band gap is constant in magnitude, even at low trap depths. From the band structure it is clear that $\Delta E > 4E_\mathrm{r}$ for all trap depths, so a good criterion for adiabaticity is

$$\frac{dV_0}{dt} \ll 16 E_\mathrm{r}^2 / \hbar. \tag{2.115}$$

For a lattice laser at $\lambda = 914\,\mathrm{nm}$, the criterion reduces to

$$\frac{ds}{dt} \ll 16 E_\mathrm{r} / \hbar \approx 2.8 \times 10^5\,\mathrm{Hz}, \tag{2.116}$$

which means that a loading rate of more than 1 ms will be adiabatic with respect to the single-site energy scale.

- *Multi-particle energy*. When loading the atoms into the lattice, there will be a spatial redistribution due to the change in external potential. This will typically be a compression, and to keep the chemical potential constant, the atoms will tunnel to new sites. The time scale is set by the change in trap frequencies in three dimensions combined with the tunnelling rate, and it is generally a much stricter requirement for adiabaticity. The group of Immanuel Bloch investigated this criterion closer and found a ramp time of 100 ms to be adiabatic [67].

The single-site time scale also allows for two ways of unloading the cloud from the lattice. If the lattice potential is ramped down adiabatically, population is conserved in the different energy bands, and the bands are mapped onto the free-space momentum. This is called *band mapping*. When releasing such a cloud from the trap, population in the lowest band fills up the first Brillouin zone, and in time-of-flight, the width of the cloud will reflect this distribution in momentum leading to a cloud of width $2\hbar k \tau / m$, where τ is the time-of-flight. This is shown in figure 2.14 (a). Population in higher bands populate higher Brillouin zones, so they will gain an extra $\hbar k$ and appear correspondingly further away from the centre of the cloud.

If the ramp is non-adiabatic, then the lattice momentum is projected directly on the free-space momentum, and this is called a *projection measurement*. The decomposition of a Bloch band in free-space momentum shows up as clouds travelling with an integer number of $\hbar k_{\text{lat}}$ in time-of-flight, and the normalised population in each cloud is equal to the decomposition coefficient. For the lowest band, the coefficients are finite only for the orders 0 and ±2, as is shown in figure 2.14 (b) [66]. This is useful for detecting coherence (or lack thereof) in the cloud, since the decomposition washes out for an incoherent ensemble.

A third way of applying an optical lattice is the so-called *Kapitza-Dirac* method. Here, the lattice is ramped up instantly leading to a projection from free-space to lattice momentum. After a short time, the lattice is instantly ramped down again, such that the lattice momentum is projected back onto the free-space momentum. While in the lattice, the cloud evolves under the lattice Hamiltonian which introduces a complicated oscillation between the scattering orders. The oscillation pattern depends on lattice depth, and this provides a method for inferring s [40]. This method is mentioned in section 3.3.

CHAPTER 3

EXPERIMENTAL APPARATUS

In this chapter, I shall describe the experimental apparatus used for the work presented in this thesis. The first section outlines the “core setup” used for the production of Bose-Einstein condensates. This was built by Henrik Kjær Andersen and Jesper Fevre Bertelsen, and a detailed description of this setup may be found in their Ph.D. theses [40, 41]. Instead, I shall highlight the changes to the setup in the last few years. Several of the changes occurred after moving the experiment to its current location in late 2010. The following sections describe the main changes to the experiment: magnetic field control, optical traps, Faraday laser setup, absorption imaging setup, experimental control software and microwave setup.

3.1 BEC apparatus

Overview

The experiment produces Bose-Einstein condensates of ^{87}Rb, and the system is sketched in figure 3.1. A typical experimental sequence for creating a BEC is divided into five broad steps:

1. *Magneto-optical trap* (MOT). Atoms are loaded to the trap from a background pressure of rubidium, which is maintained by running current through a dispenser. Magneto-optical trapping is a combined cooling and trapping routine where atoms are immersed in near-resonant light from all spatial directions. A magnetic quadrupole field is applied such that if an atom moves away from the centre of the trap, it becomes resonant with the laser light and is “kicked” back into the trap by absorbing a photon. In order for the atom to distinguish between two counter-propagating laser beams, they are given opposite circular polarisations, so the atom will only gain momentum towards the centre of the trap instead of out of the trap [68]. Typically, $\sim 10^9$ atoms are loaded.

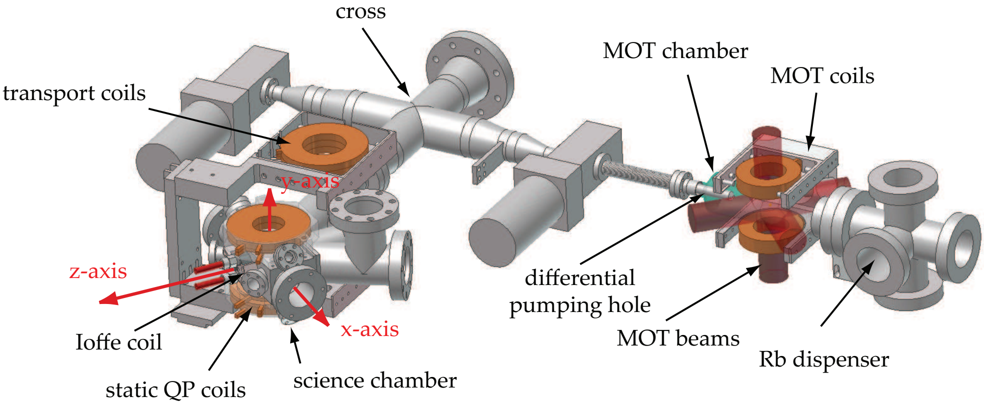

FIGURE 3.1: Overview of the vacuum system. The six cooling beams are shown as red cylinders in the MOT region. At the Science chamber, the three axes are shown as red arrows. Used with permission from [40].

2. *Transport.* Since the MOT chamber has a reasonably high background pressure of ^{87}Rb in order to load atoms into the trap, the lifetime is insufficient for further cooling. Therefore, another chamber – the *Science chamber* – is installed, and the two chambers are connected by a narrow tube, such that the two chambers can be held at different pressures. The atoms are moved to the cross through the differential pumping stage by a movable magnetic trap, and from there, a second magnetic trap moves the atoms to the Science chamber.

3. *Quadrupole Ioffe-Pritchard configuration trap* (QUIC). The Science chamber features two types of magnetic traps: The *quadrupole trap* (QP) and the QUIC trap. Initially, the cloud is loaded into a quadrupole trap, leading to a linear trap potential as shown in figure 3.2 (a). As the cloud is cooled down, the atoms spend more time in the centre of the trap, where there is a zero-crossing. This makes the atoms susceptible to *Majorana spin flips*, where the spin does not follow the magnetic field adiabatically and are transferred to another spin state. Spin flips to untrapped states causes losses, and to avoid this, the trap is transformed to the QUIC type by adding a third coil, breaking the symmetry and changing the potential to a harmonic shape as shown in figure 3.2 (b).

4. *Forced evaporative cooling.* The physical principle for cooling in the Science chamber is evaporation. Here, RF radiation is applied to the atoms, which

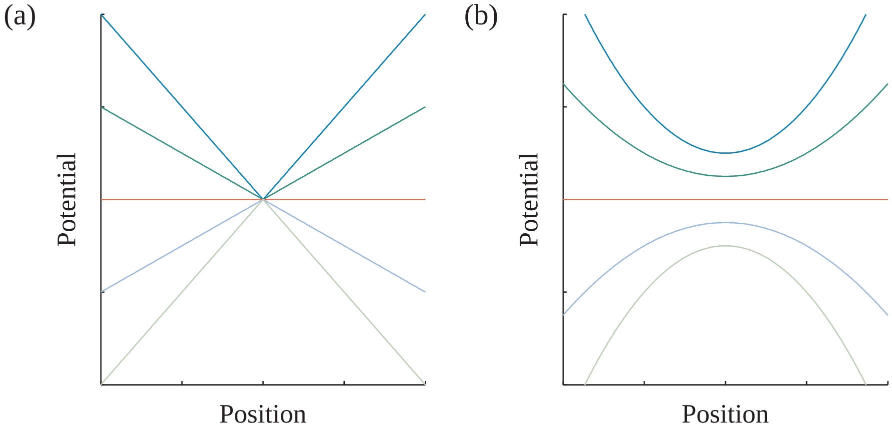

FIGURE 3.2: Magnetic potential of ^{87}Rb. $m_F = 2$ (dark blue), 1 (dark red), 0 (green), −1 (bright red), −2 (bright blue). *(a)* Potential in QP trap. *(b)* Potential in QUIC trap. The offset field from the Ioffe coil produces the finite potential in the centre of the trap.

drives transitions between different m_F states in the $F = 2$ manifold. A transition occurs only when the frequency of the RF radiation matches the Zeeman shift in the magnetic trap, which depends on the atom's position in the trap. Since the warmest atoms spend most of the time at positions furthest away from the trap, they will be shifted towards higher transition frequencies. Applying RF radiation with a large frequency and then slowly ramping it down in frequency will thus address the warmest atoms and transfer them to an untrapped state (figure 3.2 (a)) leading to an overall colder cloud [5]. The total time for evaporative cooling is around 45 s.

5. *Absorption imaging.* To probe the atomic cloud, the atoms are exposed resonant light, and the Shadow they cast on the light is imaged on a CCD camera. Typically, the cloud is allowed to expand for 15-20 ms before imaging; this time is called *time-of-flight*.

The vacuum system and the lasers are mounted on two separate optical tables denoted the *vacuum table* and *laser table* respectively. This separation is chosen to eliminate as many vibrations as possible to the lasers. The light is delivered to the vacuum table through optical fibres.

The RF radiation is produced by a home-built synthesizer (10 kHz – 70 MHz) which is controlled directly from the computer via *direct digital synthesis*. The

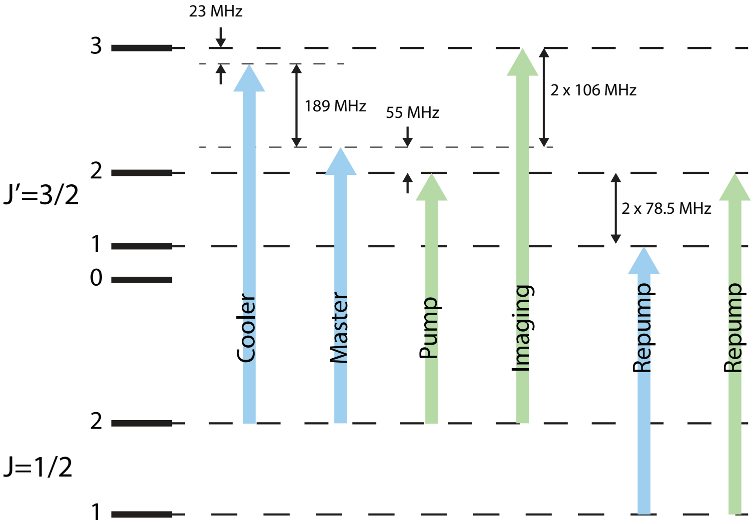

FIGURE 3.3: Lasers and lock points relative to the structure of ^{87}Rb. The lock points are shown in blue, and the frequency after shifts in AOMs are shown in green.

possibility also exists to connect the synthesizer to an FPGA, which supplies the frequencies for the radiation. This option is crucial for the work presented in section 7.1.

Laser table

The laser system is based on three home-built diode lasers that are running in Littrow configuration [69], and they emit light around 780 nm which corresponds to the D2 line of ^{87}Rb. The three lasers are called *Master*, *Cooler* and *Repump* and each has a saturated absorption spectroscopy setup [70]. The lock points for the three lasers and their frequencies after passing through *acousto-optical modulators* (AOMs) are shown in figure 3.3.

The Cooler laser is amplified in a *tapered amplifier* (TA) which increases the power to 320 mW. The light is then divided between 3 different fibres, guiding the light to the vacuum table. Each fibre is split in two by 50/50 fibre splitters, such that they constitute a counter-propagating beam pair for the MOT.

In combination, the Cooler and Repump laser create a closed cooling scheme. The Cooler excites an atom to $F' = 3$, and the only dipole-allowed relaxation is to $F = 2$. However, an atom will occasionally relax to the $F = 1$ state through off-resonant excitation to $F' = 2$, and here it is not available for further excitation from the Cooler. Such an atom will be lost to the cooling cycle if the Repump laser is not included. The Repump laser excites an atom from $F = 1$ to $F' = 2$, from where it will predominantly relax to $F = 2$ reinserting it into the cooling cycle.

The Master laser serves a dual purpose: Optical pumping and imaging. To this end, a half-wave plate is mounted on a mechanic flipper which makes it possible to send the beam through one of two ports on a polarising beam splitter. For the optical pumping, it is sent through a single-pass AOM where it is shifted 55 MHz down in frequency (blue arrow, "Pump" in figure 3.3), and for the imaging, it is sent through a double-pass AOM where it is shifted $2 \times 106\,\text{MHz}$ up in frequency (blue arrow, "Imaging" in figure 3.3).

For both applications of the Master laser, it can be combined with a small amount of the Repump laser. For the optical pumping, this is necessary for capturing any atoms that relax to $F = 1$ during the pumping. When imaging, the Repump can be used to see any atoms in $F = 1$.

The only change that has been made to the laser setup is the omission of a *compressed MOT* (CMOT) phase. After the MOT, the atoms can be further cooled by allowing the atoms to spend more time in the dark state, thus decreasing the light pressure.

This method was used in the old laboratory, but after moving the experiment to the new lab, the CMOT decreased the atom number after capturing them in the MOT coils. This has not been fully explained, but we suspect that the background magnetic field is the problem, as it is different in the new lab. Currently, we are not able to compensate the background field in the MOT chamber, so we decided to omit the CMOT stage. However, if more atoms are critical for later experiments, new cancellation coils should be constructed for the CMOT to work again.

Vacuum table

The two parts of the vacuum chamber on the Vacuum table each have a separate turbopump, ion-getter pump and titanium sublimation pump. The turbo pumps are used for pumping the chamber down from atmospheric pressure, and the ion-getter pumps are used afterwards to maintain the low pressure. The titanium sublimation pumps are fired once or twice per year if the pressure is too high.

The MOT chamber is kept at a pressure of 3×10^{-10} Torr which makes the lifetime of atoms in this region relatively short. The pressure in the Science chamber is much lower, $\sim 5 \times 10^{-12}$ Torr [40], because there are no rubidium dispensers running. The lifetime in this chamber is around 80 s.

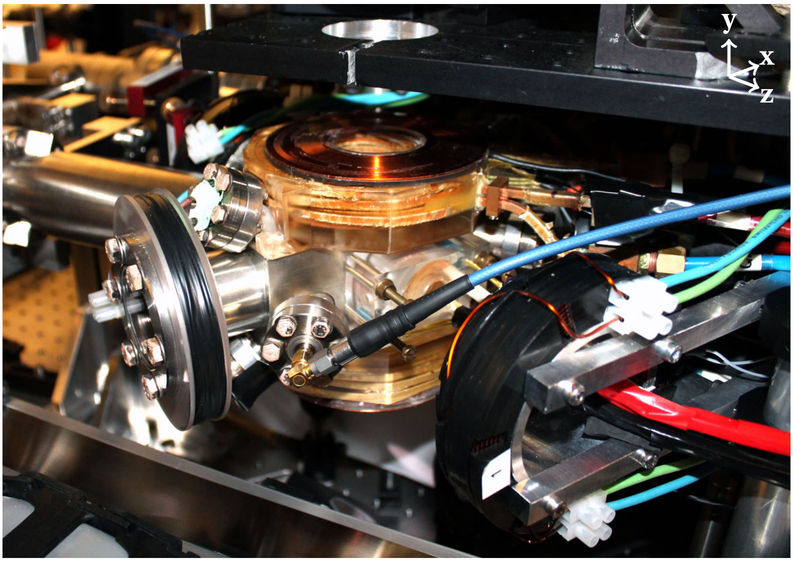

FIGURE 3.4: Science chamber. The quadrupole part of the QUIC trap are the epoxy-covered coils visible below and above the chamber. The Ioffe coil is partly hidden behind a microwave cable. Above the QP coils, one of the y-shim coils is visible. The x- and z-shim coils are covered in black tape, and on the side of the z-shim coil pointing towards the chamber, one of the fast coils can be seen.

The Science chamber is designed to allow optical access along three perpendicular axes. In figure 3.4, the Science chamber is pictured, and the axes definitions that will be used in this thesis are shown. The Ioffe coil is aligned with the z-axis, the vertical axis is the primary axis for the optical lattice and is called the y-axis, and the last axis is the primary imaging axis and is called the x-axis.

Following the move of the experiment, three changes were made: The quadrupole coils for the QUIC trap were readjusted, the rubidium dispensers were exchanged and the moveable lens for imaging along the y-axis was fastened.

The miaslignment of the quadrupole coils was discovered, because it was difficult to obtain a BEC after the move. The trap bottom had apparently shifted one MHz up in energy, which would correspond to more than a Gauss of background magnetic field.[1] This field was directed along the z-axis, and was for some time compensated by the z-shim coils (see section 3.2), but at a later stage it was discovered that the QP part of the QUIC coils were movable and not fully tight-

---

[1] The Zeeman shift of the $F = 2$ manifold is 0.7 MHz/G, so a shift of 1 MHz would equal 1.4 G.

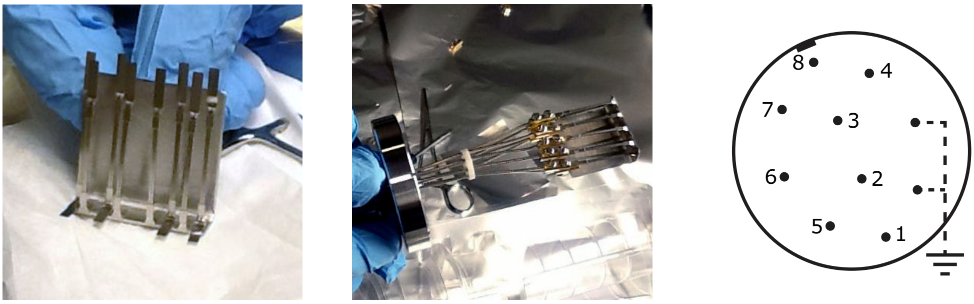

FIGURE 3.5: New ^{87}Rb dispensers. *(left)* Dispensers are point-welded onto a metal plate that is common ground. *(middle)* Dispensers mounted on flange. *(right)* Connector diagram of the dispensers.

ened. The coils can be shifted along the z-axis which amounts to changing the relative strength of the QP and QUIC coils. After realigning the coils, the trap bottom shifted back to the old value.

In the autumn of 2011, the dispensers were exchanged because the MOT loading time was increasing unreasonably, and there were no dispensers left to change to. The experiment was previously run at a very high dispenser current so out of the original four dispensers, only one was still working. It was decided to install eight new (and larger) dispensers[2] to avoid breaking vacuum again in the near future.

For the exchange of dispensers, the vent for the turbo pump was connected and a supply of nitrogen gas was prepared to minimise oxidation of the inside of the chamber. The nitrogen was supplied through the vent of the turbo pump, and a large plastic bag was filled with nitrogen as a reservoir when the vacuum was broken. Once the vacuum was broken, a steady flow of nitrogen was supplied to the chamber to keep it above atmospheric pressure. Finally, the old dispensers were removed and the new flange[3] with dispensers was inserted.

After inserting the new flange, the chamber was baked out for one week, and during the last two days, the dispensers were degassed. During the degassing, the pressure was monitored, and it rose dramatically when a dispenser was fired. The procedure was to increase the current slowly from 1 A and in steps of 0.5 A. When the dispenser had been running for a few minutes, it was turned off, and the pressure was allowed to settle again.

The biggest problem in degassing the dispensers is that the dispenser suddenly

---

[2] SAES 5G013 with 25 mm length of active area.

[3] All parts were cleaned in ultrasonic bath before inserting them into the vacuum chamber.

can release extreme amounts of rubidium which coats the interior of the glass cell. To our knowledge, there is no “safe method” for degassing, but we found this method useful. Initially, the dispensers were only degassed to 4 A, but since we were not able to load enough atoms into the MOT, the dispensers were degassed to 5 A. This caused the pressure to increase by several orders of magnitude, but afterwards, the MOT was working much better.

So far, dispensers 1-3 and 6-8 have been degassed (figure 3.5). This is fine as long as vacuum does not have to be broken, since exposure to air would deteriorate the dispensers quickly. Therefore, two dispensers (4 & 5) have been left intact for such a situation. During the last 2.5 years, we have only been using one dispenser, so it seems that the current setup is very rubidium-efficient.

The final change in the setup was the fastening of the movable lens along the vertical y-axis. This lens is mounted to a stage controlled by an automated micrometre screw, and was intended to shift along with the time-of-flight to always keep the condensate in focus when imaging along y. Due to concerns about reproducibility and its influence on the optical lattice, it was decided to disconnect the automated micrometre screw[4].

3.2 Magnetic field control

The primary coils are the three quadrupole pairs MOT, Transport and QUIC coils (see figure 3.1). The MOT and Transport coils are mounted on a rail to transport atoms from the MOT chamber to the Science chamber, and the QUIC coils are mounted on the Science chamber.

All three pairs of coils are designed for low inductance and high current, and they are supplied by separate power supplies (Delta Elektronika SM15-300). The coils have only ∼ 40 windings and need up to 300 A to deliver the desired magnetic fields, which necessitates significant cooling. Therefore, the coils are made of hollow wire such that cooling water can flow through them, and the coils are cast in epoxy to avoid deformation as seen in figure 3.4.

The MOT and Transport coils are unregulated, but the QUIC coils have a regulation system using several Danfysik Ultrastab current transducers to measure the current. The circuit was designed with three IGBTs that would regulate the total current (T1 & T2), the current bypassed the Ioffe coil (T2) and the current bypassed the QP coils (T3). The T1 IGBT was disconnected as it gave better stability of the system, so in the current setup, the Ioffe coil cannot be bypassed (see figure 3.6).

---

[4] The lens is shown in figure 3.10 after the Science chamber.

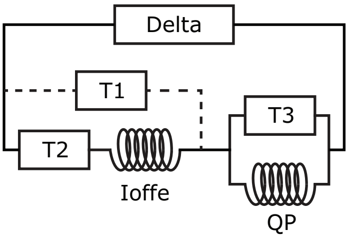

FIGURE 3.6: The QUIC coils circuit. T2 and T3 are IGBTs for controlling the current in each of the branches of the trap. Both are controlled by a regulating circuit. T1 has been disconnected.

I_{QUIC} (A)	I_z (A)	ν_{rad} (Hz)	ν_{ax} (Hz)	Trap bottom (kHz)
300	-0.144	370	17.9	560
150	2.8	60	12.4	–
75	2.8	32	8.6	–

TABLE 3.1: Magnetic trap parameters. I_z is the current in the z-shim coils; negative currents correspond to fields opposite to the field from the Ioffe coil. Trap frequencies are $\omega = 2\pi\nu$ and “Trap bottom” designates the RF frequency, where all atoms are evaporated away.

This means that the QP trap is produced by the transport coils, and when transferring the cloud to the QUIC trap, the current is ramped down in the transport coils while the current is ramped up in the QUIC coils.

The magnetic trap set up by the QUIC coils is summarised in table 3.1. The standard trap (300 A) gives a very high radial trap frequency, which is good for increasing the thermalisation rate. This is used together with a field along z that mostly cancels the background field.

The Transport coils also have the feature of switching between QP and Helmholtz configurations in order to generate large fields for e.g. Feshbach resonances. We have used this feature a few times, but the noise of the unregulated power supply made it unsuitable for our experiments.

Apart from the three primary coils, there is an additional shim coil pair mounted in Helmholtz configuration for each of the three axes on the Science chamber. These coils are of the same size as the primary coils but are made of regular wire and have more windings. They were originally designed to run a constant current to cancel any background fields, but they have proved very convenient for changing the offset field of the system for modest magnetic field strengths.

Axis	Windings	Calibration	Inductance	Resistance
x	190	3.24 G/A	9.75 mH	4.4 Ω
y	32	1.720 G/A	180 µH	1.1 Ω
z	169	1.721 G/A	6.55 mH	2.4 Ω
z_{fast}	33	0.363 G/A	230 µH	0.6 Ω

TABLE 3.2: Specifications of shim coils. The windings is for each of the coils in the pair. Calibration was made using microwave radiation and following the transition as the current is varied. Inductance and resistance are measured values.

Previously, only the z-shim coils was used to set the trap bottom and to decompress the trap. For this, the coils were powered by a Danfysik System 7000 bipolar current supply prototype. Although very stable in current, the power supply had a ramp time of ∼ 10 ms which was too slow for the spinor experiments presented in chapter 5. Therefore the power supply was replaced by a HighFinesse BCS 13/4 bipolar power supply which is both stable and fast, but has a limited current range of ±4 A. Furthermore, the original coils were replaced by a more symmetric coil pair which has both a slow part with 169 windings and a fast part with 33 windings. Currently, only the slow coils are in use.

The parameters of the shim coils are shown in table 3.2, and from the combination of inductance and resistance, it is clear that the y axis has the shortest rise time $\tau = L/R$. This makes the y-shim coils ideal for fast ramps, and to this end, another HighFinesse power supply is used for these coils. The power supply has different ramp settings, but the very fast settings causes the output to oscillate.

The *in situ* calibration of each of the coils was performed by driving the hyperfine $|F=2,\, m_F=2\rangle \rightarrow |F=1,\, m_F=1\rangle$ transition for different shim currents. This maps out the relation between the transition frequency and the current in the coils. From the Zeeman shift, the frequency is

$$h\nu = E_{2,2} - E_{1,1} = \nu_0 + (g_2\mu_B 2B - g_1\mu_B B), \tag{3.1}$$

where ν_0 is the transition frequency without magnetic field. Since $g_2\mu_B = -g_1\mu_B = h \times 0.700\,\text{MHz/G}$, this makes it easy to find the magnetic field

$$B = \frac{\nu - \nu_0}{3 \times 0.700\,\text{MHz/G}}. \tag{3.2}$$

For each coil axis, the field is given by

$$B = \sqrt{\left(A_i I_i + B_i^{(\text{off})}\right)^2 + B_0^2}, \tag{3.3}$$

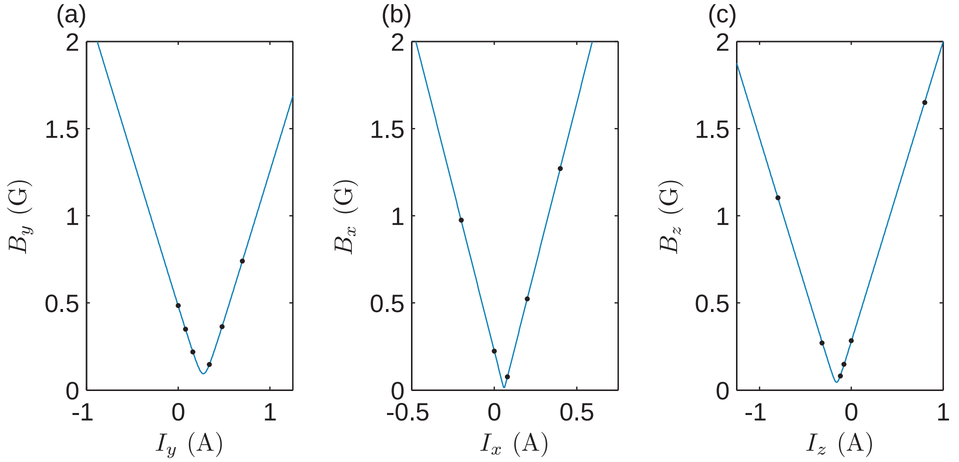

FIGURE 3.7: Calibration of shim coils and nulling of background field. The slope at large currents yields the calibration of the coils in table 3.2 and the minimum point corresponds to the background field. *(a)* Calibration of y-shim coils. *(b)* x-shim coils. *(c)* z-shim coils.

where A_i is the calibration of the coil, I_i is the current through the coils, $B_i^{(\text{off})}$ is the offset field along the given axis and B_0 is the transverse offset field. So by mapping out $B(I_i)$, one obtains not only the calibration of the coils but also the offset fields. This "field nulling" is crucial for being able to produce accurate magnetic fields, since the offset has to be taken into account. The procedure is illustrated in figure 3.7.

In practice, this requires an optical trap to keep the atoms in $|F=1, m_F=1\rangle$ trapped. Since the microwave transition shifts significantly (3×0.700 MHz/G) compared to the Fourier width of a typical pulse ($\sim$ 10 kHz), it is advantageous to use a microwave sweep to find the transition frequency roughly, and then locate it accurately with pulses afterwards.

The HighFinesse power supplies are controlled by arbitrary waveform generators that are programmed from the computer (see section 3.6). This is because there has been a problem with ground loops between the experiment control computer and the power supplies. This problem is not present for the Knürr-Heinzinger PTN 32-10 power supply that drives the x-shim coils, but this power supply is running on another power group. The ground loops can most likely be avoided by moving the optocoupled D/A-converters that generates the computer output to the same power group as the power supplies.

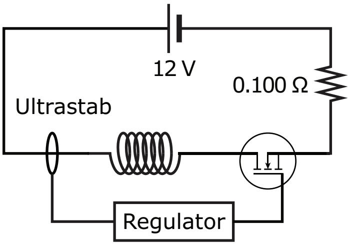

FIGURE 3.8: Regulation of y-shim coils when driven by a battery. The wire is wound 10 times through the Ultrastab to exploit the 200 A range of the transducer. The resistor is only included for monitoring.

Finally, another method for generating large, uniform fields has been implemented in the setup. Owing to the low resistance of the y-shim coils, a large current can be driven with only moderate voltage. We used a 12 V car battery as supply, since it produces a very pure DC voltage, devoid of 50 Hz noise. For this, a regulation circuit was built for the setup, where a MOSFET[5] regulated the current in the circuit using a Danfysik Ultrastab for probing. The circuit is shown in figure 3.8, where a 0.100 Ω resistor was include for monitoring the current.

The setup was able to produce ~ 10 A, but since the coils are not cooled, the current should only be pulsed for a short time. We have also tested the system with two batteries in series which worked fine for ~ 15 A, but only applied for 20 ms.

3.3 Optical traps

The optical traps are generated by diode lasers running at 914 nm. The lasers are not locked, but single-mode behaviour is monitored on an optical cavity. A master laser in Littrow configuration and a slave laser without external cavity together seed the three TAs as shown in figure 3.9. The Master laser is used to seed the y-TA for the vertical optical lattice, and the Slave laser seeds the x- and z-TAs that are used for the optical dipole trap. Each of the three TAs is seeded with 30-35 mW of light power.

Previously, the three TAs were all designed to generate optical lattices, but during the last four years, only the y-lattice has been in use. Furthermore, the x-TA was found to be damaged, and it was decided to completely redesign the x- and z-TAs for a crossed dipole trap in the beginning of 2014.

---

[5] APT10M-07-JVR, n-channel power MOSFET.

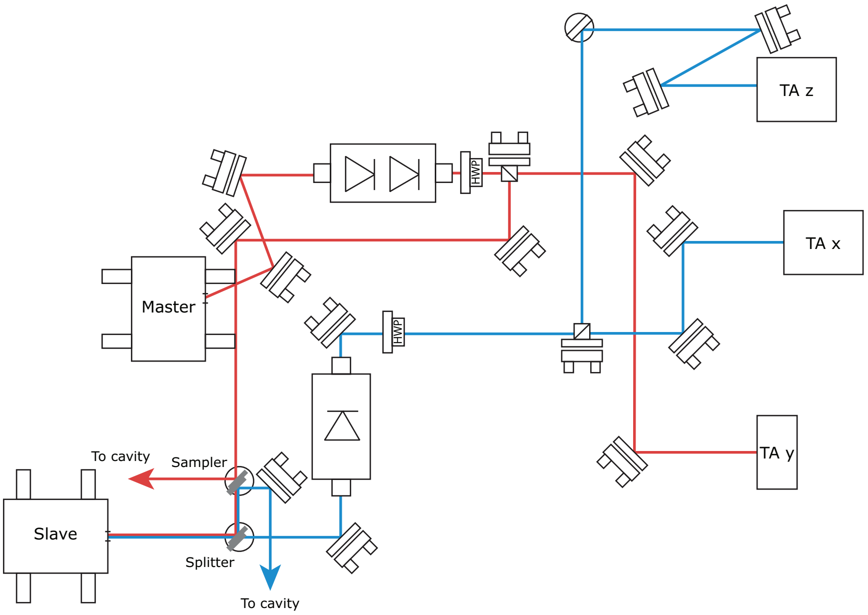

FIGURE 3.9: Laser setup for the optical traps. The Master laser (red beam) is a free-running 914 nm diode laser, and the Slave laser (blue beam) is a 914 nm external cavity laser diode with no external cavity. The Master laser is protected from reflected light from the Slave laser by a 60 dB optical isolator whereas the Slave only uses a 40 dB isolator.

Optical lattice

The y-TA generates around 375 mW after the optical isolator, which is enough for the lattice depths we are interested in. However, the TA is not saturated, so the output can be increased by diverting more power from the Master to the TA. After shaping the beam with a cylindrical lens, it is sent through an AOM before being transmitted to the Vacuum table through an optical fibre (see figure 3.10).

The lattice power is regulated by a home-built circuit that adjusts the AOM power from a signal obtained on the Vacuum table, and this allows the regulator to adjust for any polarisation fluctuations in the fibre. The setting of the regulator is controlled by an analog output from the computer which is added with the signal from an arbitrary waveform generator in an analog adding circuit. The waveform generator can also create a sinusoidal signal on the kHz scale which amplitude modulates the optical lattice.

The lattice beam has a piezo mirror before and after the chamber to help align

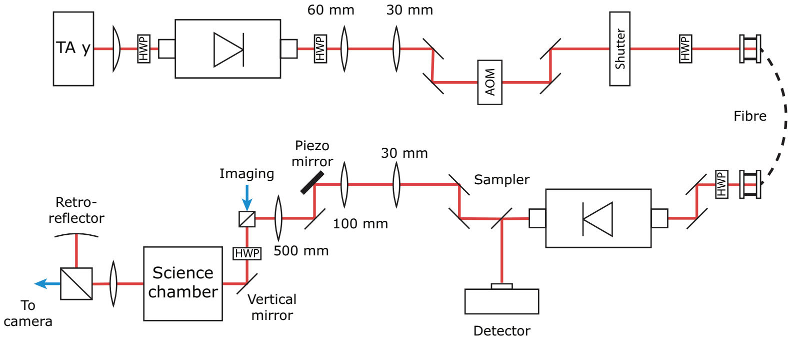

FIGURE 3.10: Sketch of beam path of y-lattice. The first telescope is used to match the beam profile of the light to that of the fibre. The second telescope is used to obtain the desired beam waist. Both the "piezo mirror" and the retro-reflector are equipped with a piezo motor that is controlled from the computer.

the lattice with the QUIC trap. The mirror may be tilted horizontally or vertically with a piezo controller which in turn is controlled from the experiment control computer. However, the piezo motor shows a large degree of hysteresis when it changes direction, and this can be a problem when aligning the lattice.

The lattice is typically aligned by pulsing the beam on for one or two milliseconds just as the cloud is released from the magnetic trap. The optical dipole force causes the cloud to accelerate and the position of the cloud after time-of-flight is mapped out as a function of the position of the light beam. The cloud position displays a dispersion-like profile, which is simply the gradient of the Gaussian profile of the lattice beam. The procedure is first to centre the incoming beam by placing the beam just at the zero-crossing of the "dispersion" (for this, the retro-reflector is blocked), and afterwards the procedure is repeated with the reflected beam.

This method works very well for a single optical lattice beam, and the alignment can be quantified by measuring the lattice depth. We use two different methods: parametric loss spectroscopy and Kapitza-Dirac oscillations. Both methods are discussed in greater detail in the thesis of Henrik Kjær Andersen [40].

Parametric loss spectroscopy measures the loss of atoms as the lattice is amplitude modulated. When the modulation frequency matches the energy difference between 0th and 2nd band, the atoms absorb a phonon and are excited to the 2nd band, see section 2.5. If this band is untrapped, the atoms will tunnel out of the lattice and lost from the system. From this resonance, the lattice depth can be calculated from a single-particle model as the band spectrum in figure 2.12.

However, this method is not precise, and it is limited to relatively low lattice

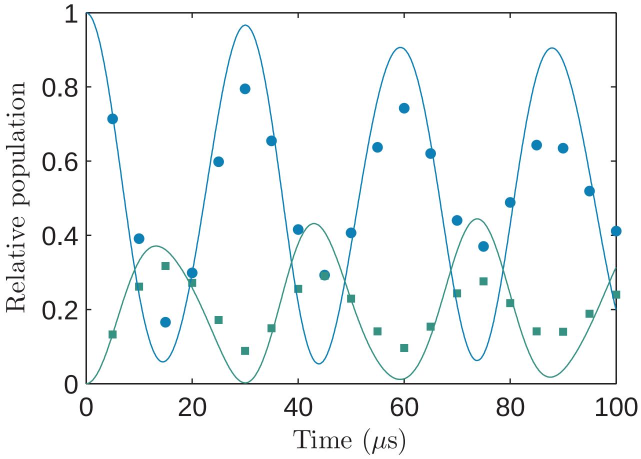

FIGURE 3.11: Kapitza-Dirac lattice calibration. The oscillation of the momentum orders $n = 0$ (blue, filled circles) and $n = 1$ (green, squares) is shown along with the fits. The values for s is 18.29(21) for $n = 0$ and $s = 18.29(25)$ for $n = 1$.

depths, as the atoms must be lost from the trap. Alternatively, the population in the 2nd band can be measured by performing a band mapping, but in general, we have only used this method for rough estimates, since the Kapitza-Dirac method seems more stable and precise.

The Kapitza-Dirac calibration uses the projection of a cloud onto the quasi-momentum and back to observe oscillations between the different momentum orders. When the lattice is switched on instantly, the free-space momentum is projected onto the crystal momentum, and while in the lattice, the cloud evolves according to the energy of the lattice bands. When the lattice is switched off again, the crystal momentum is projected back onto the free-space momentum, and the time evolution in the lattice amounts to an oscillation between the different momentum orders.

In general, these oscillations are complex functions of s. By numerically evaluating the time evolution of such a cloud, it is possible to construct a fit routine that returns the best guess for s from the evolution of atoms in the different momentum orders [40]. The result from such a calibration is shown in figure 3.11, and the oscillations in 0th and 1st order are clear. The robustness of the method is also good, since the oscillation frequency is insensitive to poor measurement of the population.

For the data shown in figure 3.11, the fit result is $s = 18.29(21)$ for the 0th order and $s = 18.29(25)$ for the 1st order. It is also possible to fit the 2nd order, but since the population in this order is small at these lattice depths, the result is more uncertain.

Finally, it should be mentioned, that the Kapitza-Dirac method requires a very pure condensate, since any thermal atoms smear out the orders, yielding much poorer fits.

Optical dipole traps

After finishing the spinor experiments that are the subject of chapter 5, it was decided to rebuild the two horizontal lattice beams to a crossed dipole trap. Two beams are necessary for good trapping of a BEC, since, for a single beam, the longitudinal confinement is much smaller than the radial confinement as seen in equation (2.98).

The two horizontal lattice beams had not been working for at least four years, and there were no plans for working with three-dimensional lattices in the near future. Rather, an optical dipole trap would be advantageous for loading the BEC to the lattice without the QUIC trap. Spinor physics depends crucially on the ability to change the magnetic field independently of the trap, and for our experiments, a uniform field was required. This meant that the QUIC trap had to be turned off, leading to cloud oscillations in the lattice and heating of the cloud. In this context, a dipole trap would be a useful stage after the QUIC trap, where a BEC could be achieved before loading it into the lattice.

Since the TA chip for the x-axis was damaged, it was replaced by a new chip from Eagleyard[6]. Both the x- and the z-TAs were placed in a new housing following a design from the Institut für Quantenoptik (Leibniz Universität Hannover), since the old design had thermal problems when increasing the current [40].

The new design features a smaller heat sink and an NTC resistor which is positioned further away from the chip (see figure 3.12). The chip is protected by four diodes (1N-4148) in series to avoid over-voltage and a single reversed diode (1N-5711) in parallel to avoid negative bias. The TA is cooled by a Peltier element (Global Component Sourcing ETC-071-14-11-E), and the light is coupled into the chip with a 4.51 mm aspheric lens and collimated with a 3.10 mm aspheric lens and a 50 mm rotatable cylindrical lens. The two aspherical lenses are mounted in a tube which allows them to be moved after they have been glued into the TA. Further details on the TA design can be found in the progress report by Romain Müller [71].

---

[6] EYP-TPA-0915, DA-04870

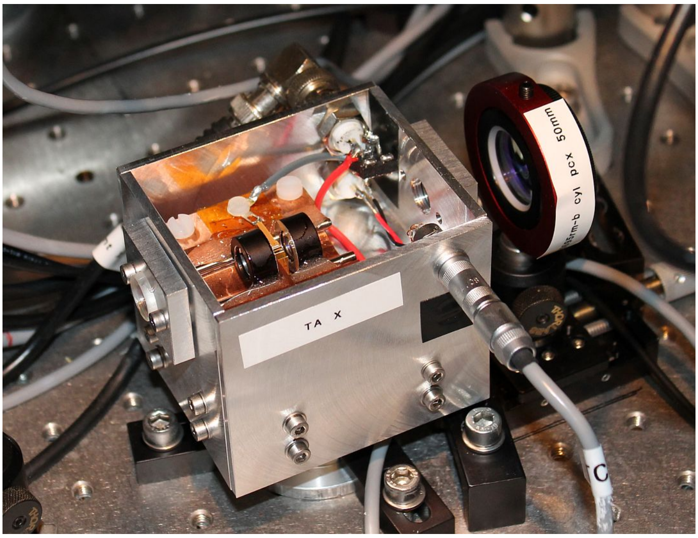

FIGURE 3.12: Tapered amplifier for dipole traps. The TA chip is mounted on a copper block that is connected to the positive lead of the supply current. The NTC resistor is mounted with heat-conducting glue in one of the corners of the copper block. Light is injected using an aspherical lens in a tube, and a similar lens is used for collimating the emitted light along the vertical axis. The final beam profile is produced by the cylindrical lens outside the casing.

The optical layout of the dipole traps is equivalent to that of the optical lattice. The beam path of the x-dipole trap is shown in figure 3.13, and the z axis is designed similarly. The beam waist was measured by means of a uEye camera that was working without filter; this was important for the very small spot sizes. To avoid saturation of the camera, the dipole beam was reduced in intensity by a OD4 reflective filter before the optical fibre.

The polarisation of the beam is cleaned on a polarising beam splitter after the fibre, and the detector only gets signal from light leaking through a mirror. In order to focus the dipole beam tightly, the beam is expanded in a Keplerian telescope before the final 500 mm lens. With an expected power of $\sim$ 300 mW at the chamber, we designed the trap to a depth of $30\,\mu$K which required a beam waist just below $45\,\mu$m. The design of the beam path is flexible, since the final 500 mm lens is mounted on a translation stage. This allows the beam waist at the position of the atoms to be varied.

The propagation of the beam is shown in figure 3.14, and the measured beam waists are $44\,\mu$m horizontally and $39\,\mu$m vertically indicating a small ellipticity of

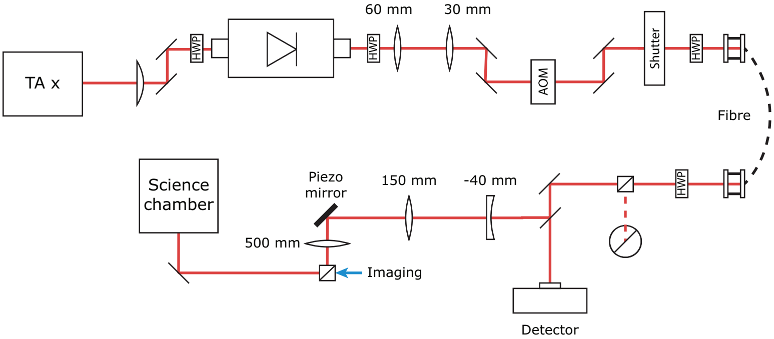

FIGURE 3.13: Sketch of beam path of the dipole trap along x. The first telescope is Galilean and matches the beam profile of the light with that of the fibre, and the second telescope is Keplerian and expands the beam in order to obtain a narrow beam waist at the location of the atoms. The detector is positioned behind a mirror and measures the transmitted light.

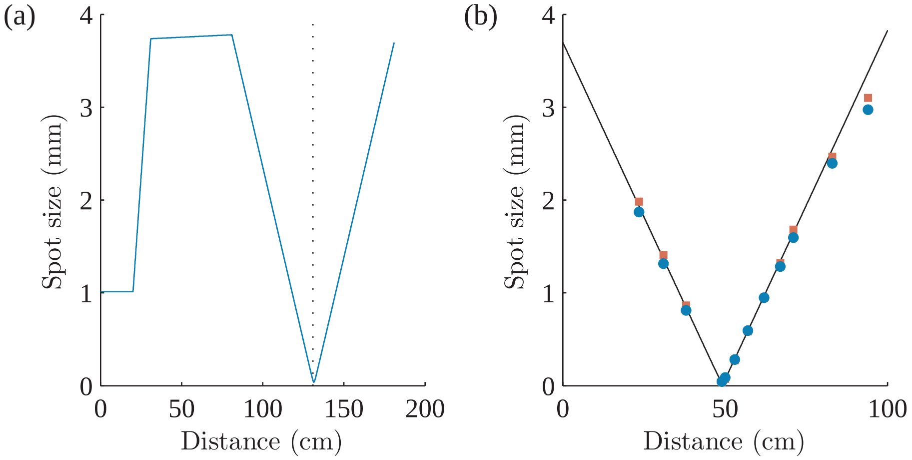

FIGURE 3.14: Spot size of dipole beam along x. *(a)* Propagation of beam after fibre outcoupler calculated with ABCD matrix. The dotted line marks the position of the atoms. *(b)* Measured spot size of the beam after the 500 mm lens. Horizontal data (blue dots) and vertical data (green squares) is plotted along with an ABCD matrix calculation (red line).

the beam profile. An ABCD matrix calculation matching the data points yields a beam waist of 38.8 µm as shown in figure 3.14 (b). This is in very good agreement with the value calculated for the entire setup in figure 3.14 (a): 38.9 µm.

For a crossed dipole trap it is important to avoid interference between the two beams as it can create a moving lattice structure which heats the cloud. This is avoided by choosing opposite orders for the AOM, such that one is shifted up in frequency and the other is shifted down in frequency. Since the AOM is working at 80 MHz, the beating between the two beams would be at 160 MHz which is too fast for the atoms to follow. To further eliminate interference, the two beams have opposite polarisation, which is achieved by inserting a half-wave plate in front of the chamber on the z-axis. This wave plate affects the polarisation of the imaging beam along z, but this has not been a problem so far.

When running the two dipole TAs[7] at 2.9 A, the z-TA delivers around 1 W of power whereas the x-TA only delivers 700 mW. Both are specified for 1.5 W, but none of the chips that have been used in this experiment have been able to output this power. The x-chip is from a new batch of the 914 nm TAs that was bought in early 2014, whereas the z-chip dates back to the first lattice setup that was built around 2008. Whether the new batch delivers less power is still unknown, but the amount of power is sufficient for the experiments that are planned in the near future.

At the Science chamber there is around 275 mW left in both beams, which is close to the expected 300 mW. Thus, the desired trap depth of $\sim 30\,\mu\mathrm{K}$ should be achievable with the current beam waists. The first experiments using this optical dipole trap are described in chapter 6.

3.4 Faraday laser system

The last laser in the setup is called the Faraday laser, since this laser is detuned to a regime, where the Faraday effect discussed in section 2.4 is relevant. The laser is built from the same design as the three "core lasers", i.e. a diode laser in a Littrow setup, and it is offset-locked to the Master laser. This makes it by default 212 MHz red detuned to the $F = 2 \rightarrow F' = 3$ transition, as the Master laser is locked to the $F = 2 \rightarrow F' = 1/3$ cross-over. The laser is further sent through a double-pass AOM to control the intensity of the laser, and since this AOM is running at 200 MHz, the laser has an overall blue detuning of 188 MHz. The setup is sketched in figure 3.15.

---

[7] They are specified for 3.0 A for maximum safe operation, but previously we have only run 2.5 A through them for safety.

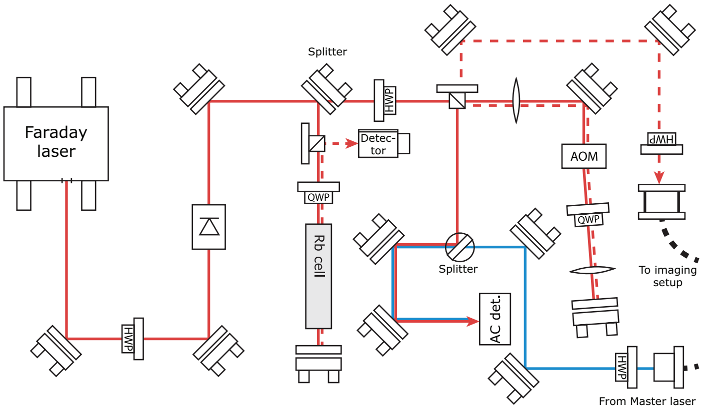

FIGURE 3.15: Drawing of the Faraday setup. The beam from the Faraday laser is shown in red, and the light from the Master laser used for the offset lock is shown in blue. Reflected beams are dashed. The two lenses before and after the AOM have the same focal length and serve to more efficiently couple light into the AOM.

Depending on the lock point of the offset lock, the laser can be detuned in the range −1.5 GHz to 1.8 GHz, where positive detuning is blue. Typically, the laser is operated in the blue regime, since the effect of molecular dynamics dominates in the red region, as has also been observed in [72].

The laser is combined with the z-imaging light before the fibre, so it impinges on the atoms along the Ioffe axis. The light is linearly polarised, and after the chamber, the light is split on a polarising beam splitter. The polarisation is chosen such that the intensity on the camera is minimised, and any rotation of the light owing to interaction with the atoms is diverted to the camera (see figure 2.8).

The camera is an Andor DU-888 which features very high quantum efficiency and an electron multiplying register (EM). It can also be cooled to −60°C without any external cooling circuit, and this decreases the dark noise considerably [73].

The imaging properties of the Faraday laser has been characterised, and both the scaling of the imaging signal as well as the destructiveness has been verified according to $1/\Delta$ and $1/\Delta^2$ respectively [59]. Furthermore, the imaging factor has been referenced to standard absorption imaging, and it was found to be constant over a large range of temperatures. The atom number obtained from Faraday does not match the atom number from absorption imaging exactly; there is a constant factor of $\sim 75\%$, which is attributed to imperfections in the setup. This holds as long as the temperature is above the critical temperature.

Axis	Camera	Resolution	Pixel size µm
x	Andor DU-885	1004 × 1002	1.96
y	Andor Luca	1004 × 1002	–
z	Andor DU-888	1024 × 1024	2.68

TABLE 3.3: Cameras in the experiment and their current location. The pixel size is the apparent pixel size as it looks after magnification.

3.5 Absorption imaging system

The original setup featured imaging along all three Cartesian axes. A DTA Chroma camera was aligned with the z-axis, an Andor DU-885 was on the x-axis and an Andor DU-888 camera was imaging along the y-axis. Of these, only the DU-885 has remained on the x-axis.

In the early phases of designing the Faraday experiments, it was clear that the DU-888 would be the best choice, and since a large integrated density was needed to get a good Faraday signal, the Andor was positioned on the z-axis. The DTA was used for occasional imaging along the y-axis, but as it became necessary to image the clouds along the vertical axis for the spinor experiments, the DTA camera was giving too much trouble. Interfacing the camera became increasingly difficult, and it was decided to abandon the DTA camera, and the Andor DU-888 was positioned on the y-axis once again.

In the meantime, another camera, an Andor Luca, has been purchased and it is planned that it will be installed on the y-axis once the spinor experiments are resumed. This will leave the Andor DU-888 permanently on the z-axis for Faraday experiments.

Apart from the primary cameras, the system was designed to flexibly incorporate a number of smaller, mobile cameras connected via FireWire. However, this depends crucially on the program designed to control the cameras, the *Camera Control System*, and since it was decided to abandon this program (see section 3.6), this option has not been used to any significant extent.

The x-axis is the primary imaging axis, since it gives a good overview of both the radial and axial directions of the QUIC trap. Therefore, it was decided to implement circularly polarised light along this axis at the expense of not having an optical lattice along this direction. The lattice requires a separation of imaging and lattice light on a polarising beam splitter after the chamber to reflect the lattice light. However, this beam splitter was removed to be able to use circular imaging light.

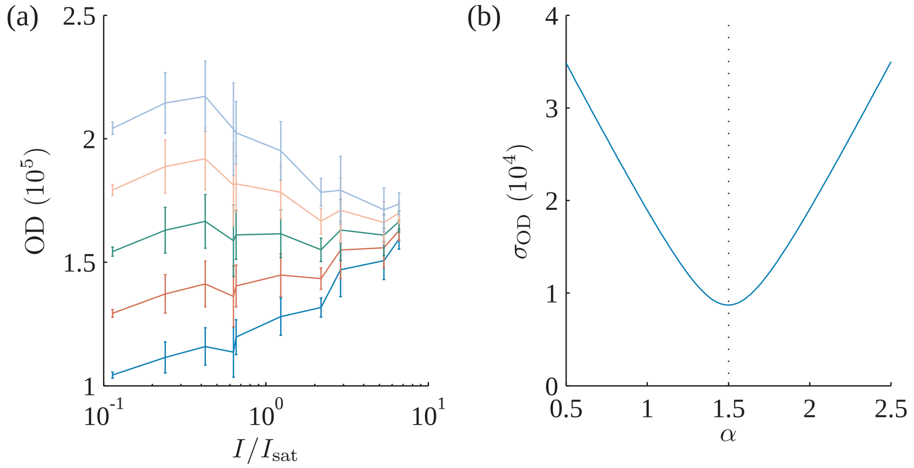

FIGURE 3.16: Calibration of effective saturation intensity. *(a)* The summed optical depth over each image evaluated with different values of α: 1.00 (dark blue), 1.25 (dark red), 1.50 (green), 1.75 (light red) and 2.00 (light blue). *(b)* The standard deviation of the summed optical depth taken over all images. The minimum occurs at $\alpha = 1.50$ (dotted line).

We have also made a calibration of the imaging system following the method of section 2.4 along this axis. The experimental procedure consists of imaging the same cloud with different light intensities a number of times. Here, the temperature was 1.0 μK to avoid saturation of large optical depth, and the duration of the imaging pulse was adjusted inversely with the intensity to keep the signal on the camera constant.

The images are then evaluated with different values of α according to equation (2.68) as is shown in figure 3.16 (a). Since the optical depth should be constant for all light intensities, the optimal value of α is the one with least variation over all images. From figure 3.16 (b) it is clear that the optimal value is 1.5. Perfect single-particle imaging would imply an α of one, but the obtained value indicates that non-ideal effects are not severe.

A similar calibration was performed for the Andor DU-888 when positioned on the y-axis, and here the value of α was 1.82 and the pixel size was 2.86 μm.

Furthermore, the amount of blurring caused by the imaging system was quantified by the *point spread function*, $\mathfrak{S}$ [74]. This was measured by inserting an aperture of 1 μm into the imaging beam, and measuring the width of the light on the camera. For the y-camera, $\mathfrak{S}$ had a $1/e^2$ waist of 5.72 μm.

In this setup, the DU-888 camera is exposed to vibrations, since it is mounted on top of two breadboards. The vertical vibrations were measured with a piezo element held down by a slab of steel, and the observed vibrations ranged from 75 to 300 Hz. These vibrations introduced fringes in the images, since the beam moves between the raw and reference images. So to avoid this, it was decided to increase the imaging speed by masking the camera and using it in fast-kinetics mode.

In this way, the time between the images was reduced to less than one millisecond, clearing the image of all fringes. However, on this time scale, the atoms do not have enough time to leave the field of view after the imaging pulse, and this leads to large blurring effects. Therefore, the Faraday laser was tuned to resonance ($F = 2 \rightarrow F' = 3$) and applied transversely to the imaging direction in order to remove the atoms by radiation pressure after the first image was taken. This method allowed for only 800 µs delays between the two images, and virtually no fringes were visible.

For the Faraday experiments, where the DU-888 was positioned on the x-axis, the camera was also operated in fast-kinetics mode. Here, the field of view is very small since imaging is performed in the QUIC trap, and therefore, the imaging rate of the camera can be very fast. Sub-millisecond imaging rates have already been achieved in this setup [59].

3.6 Experiment control

The whole experiment is controlled and kept synchronised by a single computer program called *Experimental Control System* (ECS). The program is written from scratch in Delphi 7 by Henrik Kjær Andersen specifically for this experiment, and it consists of more than 18.000 lines of code [40]. It features both digital and analog (0-5V) channels as well as built-in DDS programming. The resolution for digital channels is 1 µs and 50 µs for analog channels.

The system is designed to run in parallel with the *Camera Control System* which was also written in Delphi, but runs on a separate computer. Communication between the two programs is maintained via a TCP/IP protocol, and one can in principle keep all information about imaging in ECS and transmit it to CCS when a sequence is initiated. However, due to technical issues after updating firmware on the cameras, we have decided to abandon CCS and run all cameras with the Solis script environment delivered by Andor.

For each experimental sequence, ECS calculates all control signals for hardware, and outputs them via two DIO cards. Once the run is initiated, there is no control over the experiment from ECS, since all output is stored in the DIO cards. This means that e.g. GPIB signals cannot be transmitted during the run, which is problematic if a particular piece of hardware needs to be reprogrammed.

All GPIB commands are thus issued before the sequence is triggered by the MOT signal, and currently GPIB is only used for programming the arbitrary waveform generators that control the HighFinesse power supplies. An interface for Agilent waveform generators is implemented in ECS, and this has been extended to include the possibility of outputting a script that is directly transmitted via GPIB, or to generate a ramp by specifying a series of points. The ramp mode is typically used, since it allows for more direct control of the magnetic field. ECS interpolates the defined points into a ramp with the highest precision possible and programs the ramp as an arbitrary waveform in the Agilent. The precision is not perfect though, since the Agilent is designed for waveforms in relative values; not ramps in absolute values. Therefore, it is necessary to set the same “amplitude” for the waveform, which is achieved by adding a final point at e.g. 5V at the end of the ramp. This point should be the largest value in the ramp, so the waveform will be scaled by this value.

Currently, only the y-shim is controlled through ECS, but it should be possible to extend ECS with another “Agilent control module”, but this has not been necessary so far, since the z-shim current is rarely changed.

One particularly useful feature in ECS is that the information needed to generate all ramps and triggers for each experimental sequence is saved into a “run” file that is identified by a unique run number for each day. In that way, one can always load an old sequence and repeat the run. Furthermore, the file can also be used by external software to extract information about any sequence, and since the file is written when the sequence is triggered, the appearance of an run file is also used as a trigger for other scripts.

3.7 Microwave generation

To address the hyperfine transition $F = 2 \rightarrow F = 1$ in ^{87}Rb, microwave radiation of 6.834 682 GHz is needed. This frequency is beyond the capability of most microwave synthesizers, so in order to generate this frequency, frequency doubling is often employed.

The experiment was originally equipped with a Wiltron 6717B synthesizer connected to an AM53 amplifier from Microwave Amplifiers Ltd. The Wiltron synthesizer is able to produce 6.8 GHz directly, and the AM53 is able to amplify by 38 dB to 42 dBm. However, the Wiltron is slow in reprogramming the oscillator fre-

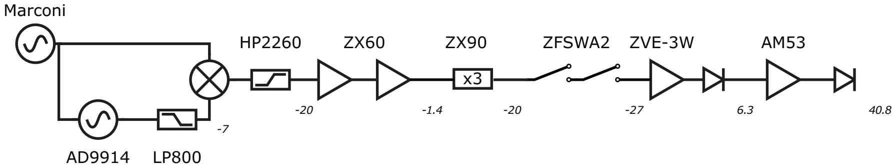

FIGURE 3.17: Microwave signal chain. The Marconi synthesizer runs at 1.75 GHz and serves as both the clock for the AD9914 board and the local oscillator for the mixer. The two final amplifiers are protected by a circulator working as an isolator, i.e. with a 50 Ω terminator on the reflected port. Numbers in italic refer to powers in dBm. All components in the chain except the AM53 are supplied by Mini Circuits.

quency, and its sweeping capability was limited by the digitisation of the steps (20 ms). Therefore, it was decided to replace the synthesizer by a more flexible setup.

The new setup consists of a programmable DDS synthesizer (AD9914) which is able to generate signals up to 700 MHz with a precision of 0.163 Hz [75]. The signal is then mixed with a local oscillator from a Marconi 2024 synthesizer running at 1.75 GHz yielding a signal around 2.28 GHz. The signal is amplified in several steps, tripled and filtered before reaching the AM53 amplifier. The signal chain is shown in figure 3.17.

The mixing and the tripling reduces the power significantly, so a number of pre-amplifiers has been applied in the signal chain. The signal is also switched by two Mini Circuits ZFSWA2 switches in order to get a good suppression. The exact choice of pre-amplifiers was based on availability.

This setup gives good suppression of other orders in the mixing procedure. The only critical element in the chain was the location of the tripler. If the tripler was placed after the switches, a lot of noise was apparently generated which lead to poor condensates. As long as the tripler was separated from the ZVE-3W amplifier by a switch, there were no problems.

The Marconi synthesizer is used both to mix with the AD9914 and to clock it. The Marconi itself is clocked at 10 MHz by an external atomic reference. The AD9914 can be controlled through a USB port using a C++ interface written by bachelor student Theis Skalmstang. The desired frequencies are programmed into ECS, and the contents are extracted by a LabVIEW script that is triggered when a new file is written by ECS. The LabVIEW script extracts the frequencies and executes the C++ interface which ultimately programs the AD9914.

The DDS chip is able to output 8 different frequencies in static mode, and this is identified by eight “profiles”. The profile is selected by applying a 3.3 V TTL signal

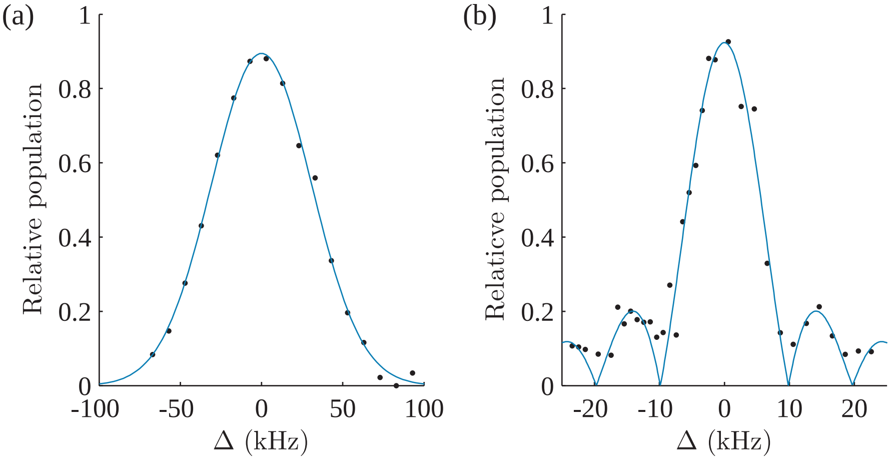

FIGURE 3.18: Microwave spectrum. *(a)* Spectrum of a 10 μs pulse. The data is fitted with a Gaussian with a HWHM of 36.3 kHz. *(b)* Spectrum of a 135 μs pulse at lower power, displaying the structure of a sinc function.

on the three “profile select” inputs PS0-2 using binary counting [75].

The AD9914 can also perform sweeps between two predefined frequencies. A sweep is triggered by a 3.3 V TTL signal to the “TRG” channel, and depending on the slope of the trigger, the sweep will go from low to high or vice versa. We have observed full transfer between the two hyperfine manifolds using the microwave sweep, but in general, it is easier to use a short, intense pulse. However, microwave sweeps are useful for localising a hyperfine transition, since it is easy to see a small population in $F = 1$ when sweeping across the resonance – even with a sweep of several MHz.

In pulsed mode, the high power of the AM53 yields π-pulses of as little 10 μs, which makes the Fourier width of the spectrum very broad compared to the magnetic noise. Such a spectrum is shown in figure 3.18 (a). The data has been fitted with a Gaussian yielding a HWHM of 36.3 kHz, which is in reasonable agreement with the 39.0 kHz expected from equation (2.70). A longer pulse of 135 μs of lower power was used for the spectrum in figure 3.18 (b), and the main peak is clearly narrower. Also, the side peaks from the sinc function are visible in this spectrum.

When driving the transition with very long pulses, the oscillation slowly dephases as seen in figure 3.19 (a). A time constant of 1.5(4) ms is observed, but around 2 ms, the oscillation is effectively damped out. The spectrum was measured with a pulse duration of 2 ms using full power, and the result is shown in

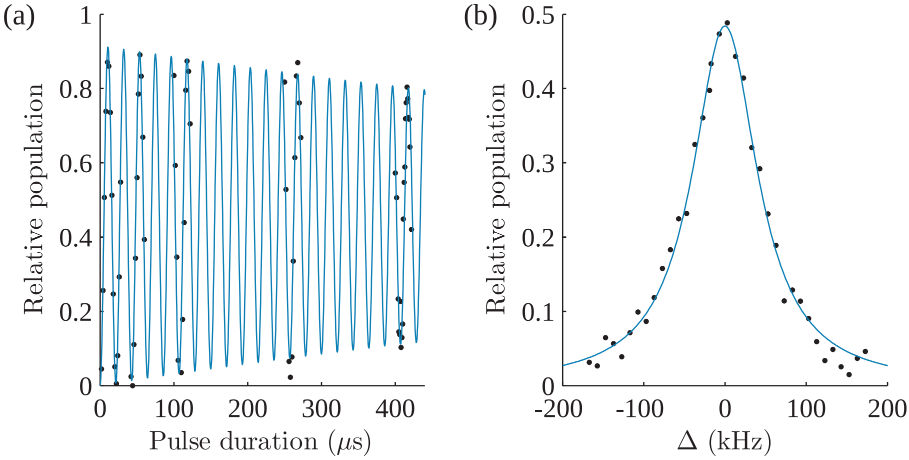

FIGURE 3.19: Long microwave pulses. *(a)* Rabi oscillations at full power showing a slow dephasing of 1.5(4) ms. *(b)* Spectrum of a 2 ms pulse at full power. The Rabi oscillation is dephased, and the high power causes broadening of the spectrum. The data is fitted with a Lorentzian with a HWHM of 46 kHz.

figure 3.19 (b). The width of the resonance is much wider here than what is seen in figure 3.18 (b), although the Fourier width is much smaller. This is due to power broadening, as discussed in section 2.4.

The previous remarks are important for using microwave transitions to measure the magnetic field stability. While high power and short pulses are good for reliable state preparation, the opposite limit is useful for measuring the stability of the magnetic field. Since the magnetic dipole transition is very weak, we attribute the width of the transition spectrum to noise in the magnetic field.

To measure the width induced by the ambient magnetic field noise, a long pulse with low power is needed, in order to resolve the width. We used a 600 µs pulse at a very low power setting, and the Fourier width of such a pulse is 0.65 kHz according to equation (2.70). While the microwave pulse was applied, the BEC was held in the optical lattice, and a constant field of ~ 1 G was maintained along the z axis.

At this time scale, the microwave pulses deliver a very fluctuating result due to the noise; i.e. in one realisation there is high transfer, but in the next there is no transfer. This indicates that the noise is slow compared to the pulse, since it amounts to an unpredictable shift in the resonance frequency.

The results of this measurement are shown in figure 3.20. The data was fit-

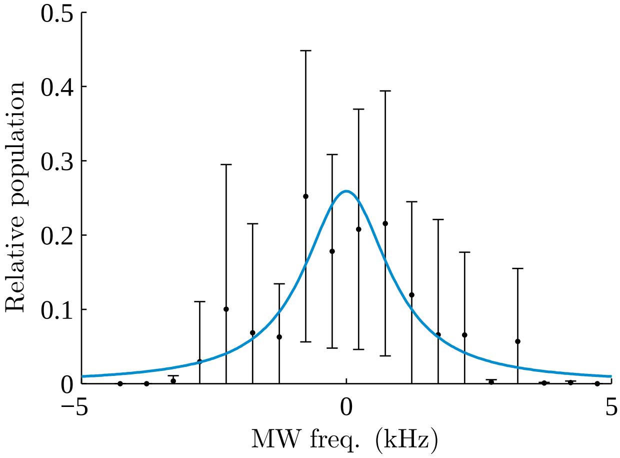

FIGURE 3.20: Microwave spectrum of the $|2,2\rangle \rightarrow |1,1\rangle$ transition with a 600 µs pulse at very low power. The data was fitted with a Lorentizian yielding a HWHM of 1.0(2) kHz. The data is shown binned in widths of 0.5 kHz.

ted with a Lorentzian yielding a HWHM of 1.0(2) kHz, which is above the Fourier width of the pulse. According to equation (3.1), this noise corresponds to 0.5(1) G of noise.

CHAPTER 4

WAVE PACKETS AND LOCALISED STATES IN AN OPTICAL LATTICE

Wave packets have been an essential concept in quantum mechanics since its formulation in the 1920s. For example, the simplest way of describing a free particle that is spatially localised is by a wave packet of plane waves, i.e. a coherent superposition of momentum eigenstates. To this day, the concept remains useful in many areas of physics research, an example of which is pump-probe experiments in molecular physics. Here, a vibrational wave packet is excited with a pump light pulse and later probed with a second pulse, yielding information about the structure and time evolution of the system [76].

In this chapter, I shall show how to create wave packets of ultracold atoms and how to obtain information about lattice structure in direct analogy with pump-probe spectroscopy. Here, the pump and probe are not laser pulses as in molecular physics, but modulation pulses – or phonons – in an optical lattice. Similar experiments have been carried out in the group of Klaus Sengstock using a degenerate Fermi gas instead of a BEC [77]. This system displayed behaviour analogous to photoconductivity, where the phonon acted as the excitation mechanism, and due to the Pauli principle, the system showed rephasing of the “holes” after wave packet excitation.

In our experiments, a BEC is prepared in a QUIC trap and then transferred to a vertical optical lattice while maintaining a weak magnetic trap potential. The lattice is amplitude modulated, leading to wave packets in the combined potential, as illustrated in figure 4.1. Such a system has been studied by Ott et al. [78], who discovered that this system supports localised states. Here, localised means that there is no spreading of these states over long time scales due to the suppression of tunnelling between lattice sites. We observe similar localisation when coupling the wave packets to distant lattice sites. This chapter is based on the work presented in [79, 80].

At a lattice depth of $s = 16$, the 2nd band is partially trapped as is apparent

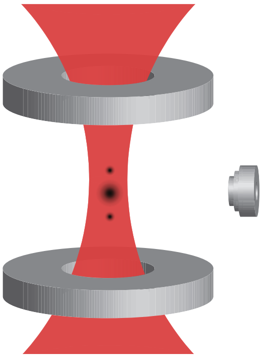

FIGURE 4.1: Sketch of the setup for the experiments presented in this chapter. A BEC is loaded into a one-dimensional lattice while keeping the magnetic potential from a decompressed QUIC trap. The lattice beam is aligned to the symmetry axis of the quadrupole coils.

in figure 4.2 (a). Furthermore, the QUIC trap is decompressed to an axial trapping frequency of $\omega_{\mathrm{ax}} = 2\pi \times 12.2\,\mathrm{Hz}$ and a radial trapping frequency of $\omega_{\mathrm{r}} = 2\pi \times 40.6\,\mathrm{Hz}$. This extremely decompressed system was simulated numerically by diagonalising the single-particle Hamiltonian of both potentials in position space,

$$\hat{H}_0 = -\frac{\hbar^2}{2M}\frac{d^2}{dy^2} + s E_{\mathrm{r}} \cos^2\left(k y\right) + \frac{1}{2} M \omega_{\mathrm{r}}^2 y^2, \tag{4.1}$$

where M is the mass of a single particle, k is the wave number of the lattice, and ω_{r} is the radial trapping frequency of the QUIC trap. Any structure due to the Rayleigh range of the beam is neglected, since it is a few centimetres, and the atoms are distributed over $\sim 100\,\mu\mathrm{m}$.

The resulting spectrum is shown in figure 4.2 (a) and shows a band structure shaped by the harmonic potential. The high-energy region shows a state spacing of $\sim 30\,\mathrm{Hz}$, which is to be compared to the band separation, which is in the range of tens of kilohertz. Hence, beyond the 2nd excited band, the system features a quasi-continuum where atoms are only trapped in the magnetic trap. Furthermore, the system displays a high degree of localisation around the edges, where the band gap acts as a potential barrier that separates a state into several localised regions.

The experimental procedure was to create an almost pure BEC of $\sim 10^5$ atoms in the QUIC trap. The trap was then decompressed by reducing the current in the QUIC coils to 150 A while increasing the z-shim current by 4 A over 500 ms. This cloud was loaded into an optical lattice over 100 ms. Afterwards, the lattice was

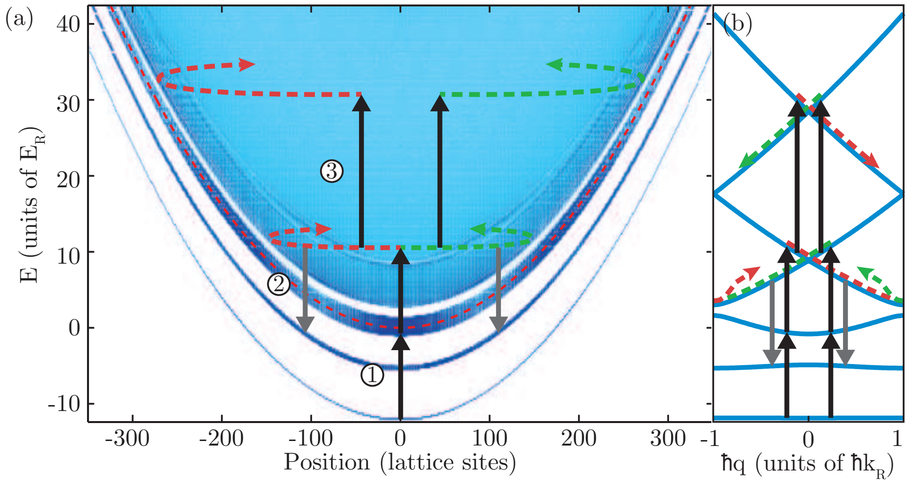

FIGURE 4.2: Simulated spectrum of optical lattice and magnetic trap. *(a)* Spectrum of the combined potential in position space. The states have been binned in regions of width $h \times 664$ Hz and dark blue corresponds to high density of states, whereas white denotes a vanishing density of state. The boundary set by the depth of the trap potential (coinciding with $E = 0$ in the centre) is marked by a red dashed line. Excitation and deexcitation processes through modulation of the lattice are shown as solid arrows, and motion of wave packets is shown as dashed arrows. *(b)* Spectrum in momentum space at the centre of the trap. Arrows are identical to (a).

amplitude modulated, with an amplitude ϵ such that the total lattice potential was

$$V_{\text{latt}}(y,t) = s E_{\text{r}} [1 + \epsilon \cos(\omega_{\text{mod}} t)] \cos^2(ky). \tag{4.2}$$

Afterwards, the system was left to evolve for a short time, before imaging the cloud in-trap.

The cloud was imaged along the x-axis using linearly polarised light at a bias field of 11 G. This was accounted for by calibrating the imaging against the standard procedure involving circularly polarised light described in section 2.4. Although the bias field was large, the trap was sufficiently decompressed for the imaging to be independent of position.

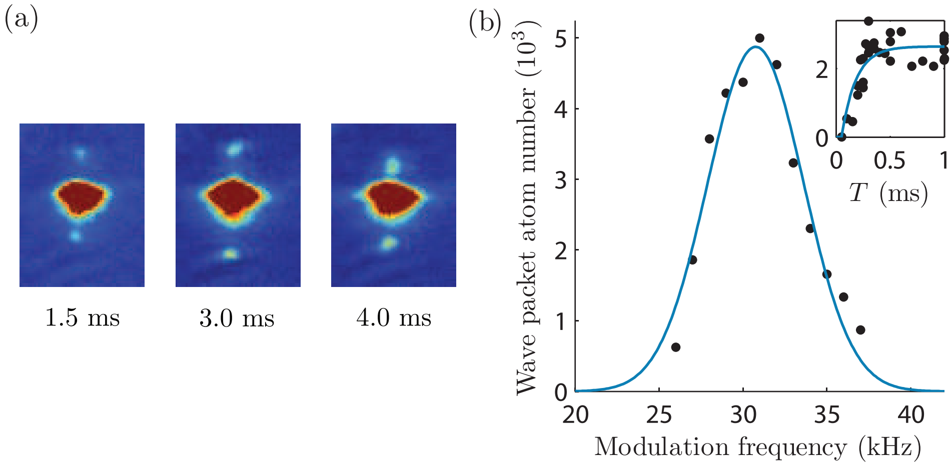

FIGURE 4.3: *(a)* Typical experimental pictures after excitation of a wave packet. Vertical axis is the lattice axis and images are taken along the x-axis. *(b)* Atom number in lower wave packet after 3 ms evolution when the modulation frequency is varied. The data is fitted with a Gaussian function with a centre frequency of $\nu_{\mathrm{mod}} = 30.8\,\mathrm{kHz}$, and a $1/e^2$ width of $5.7\,\mathrm{kHz}$. *(Inset)* Atom number in lower wave packet when varying the modulation time at a modulation frequency of 33 kHz. The data is fitted with an exponential saturation function (4.3) with time constant $\tau = 130\,\mu\mathrm{s}$. Both data sets were taken with $\epsilon = 0.165$. Vertical axis has the same units as (b).

4.1 Creation and motion of wave packets

When the optical lattice is modulated, it is possible to transfer atoms into the partially trapped 2nd excited band. Here, a further excitation is possible, transferring the atoms into the quasi-continuum (figure 4.2 (a), arrows 1). In nearly free space, the atoms evolve as wave packets and move away from the main BEC. This two-step excitation forms the basis for all the work in this chapter.

Following the procedure in previous section, we obtain images as shown in figure 4.3 (a), featuring two distinct wave packets moving in the quasi-continuum. The fact that two wave packets are produced is a consequence of the symmetry of the system; thus the band structure in momentum space shows two identical resonance points (figure 4.2 (b)).

Due to the two-step nature of the excitation process, it will be limited by the width of the 2nd excited band. This was verified by measuring the number of atoms in the wave packets as a function of modulation frequency as shown in figure 4.3 (b). Here, wave packets were excited at a variable frequency and left to evolve for 3 ms before imaging them. The wave packets appear only in a band of width 5.7 kHz which is comparable to the 7 kHz resulting from the band structure calculation.

The inset of figure 4.3 (b) shows the dependence of wave packet atom number on the duration of the lattice modulation. The data was fitted with the function

$$f(t) = A\big[1 - \exp((t - t_0)/\tau)\big]\Theta(t - t_0), \tag{4.3}$$

where A is the amplitude, τ is the time constant, t_0 is the onset time, and Θ is a step function. The atom number saturates with a time constant of 130 µs, and based on this, we choose a pulse duration of 500 µs as the standard value. In the following, a pulse duration of 500 µs is used unless other is stated.

The slope of the bands in momentum space sets the group velocity (2.109), and from figure 4.2 (b) it is clear that the wave packets will start moving. The harmonic confinement induces an oscillatory motion at the (radial) trap frequency, but at the potential barriers caused by the band gaps, the atoms either undergo Landau-Zener transitions to another band or follow the avoided crossing into the next Brillouin zone. The latter option corresponds to Bragg reflection from the potential barrier. We calculate the Landau-Zener transition probability to be $\sim 1 \times 10^{-3}$ [81], and hence, Bragg reflection is the dominant mechanism.

The sinusoidal motion is thus "cut" by a reflection on the band gap. The first reflection happens at t_{ref}, and at $2t_{\text{ref}}$, the wave packet traverses the main BEC and is reflected again at the opposite band gap at $3t_{\text{ref}}$. To refine the model, the reflection is assumed to have a duration of τ_{ref} due to the finite width of the wave packet.

This motivates the somewhat cumbersome expression for the wave packet position

$$y = \begin{cases} A\sin(\omega_{\text{r}} t + \phi_0) & 0 \le t < t_{\text{ref}} - \frac{\tau_{\text{ref}}}{2} \\ A\sin(\omega_{\text{r}}(t_{\text{ref}} - \tau_{\text{ref}}/2) + \phi_0) & t_{\text{ref}} - \frac{\tau_{\text{ref}}}{2} \le t < t_{\text{ref}} + \frac{\tau_{\text{ref}}}{2} \\ A\sin\big(\omega_{\text{r}} t + \phi_0 + \phi_{\text{ref}}\big) & t_{\text{ref}} + \frac{\tau_{\text{ref}}}{2} \le t < 3t_{\text{ref}} - \frac{\tau_{\text{ref}}}{2} \\ \cdots \end{cases} \tag{4.4}$$

where $\phi_{\text{ref}} = \pi - 2\omega_{\text{r}} t_{\text{ref}}$ is the phase shift due to reflection. The first line of equation (4.4) describes the wave packet's position before the first reflection, the second line describes its position during reflection (which is stationary) and the third line describes its position after the first reflection and before the second reflection.

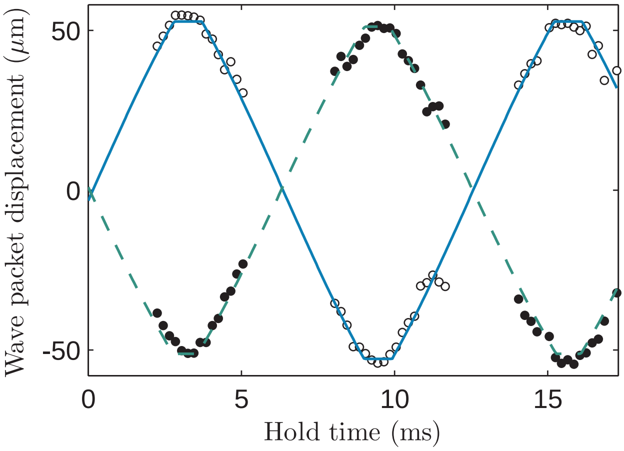

FIGURE 4.4: Motion of wave packets after excitation at 30 kHz. The initial upper wave packet (open circles) and the initial lower wave packet (filled circles) are plotted. Both sets of data are fitted with equation (4.4): Initial upper wave packet (blue, solid) and initial lower wave packet (green, dashed).

A comparison of equation (4.4) to experimental data is shown in figure 4.4. Here, the data was obtained by exciting a wave packet at 30 kHz and an image was taken in-trap after a variable evolution time. For the fit, the trap frequency was kept constant at the measured 40.6 Hz, and all other variables were varied for fitting. The reflection duration τ_{ref} yields a fitted value of 0.9(1) ms which is consistent with a quick estimate given by $2\sigma/v$, where σ is the $1/e^2$ width of the wave packet, and v is the velocity. Assuming a velocity of $3\hbar k_{\mathrm{r}}/m$ at the band gap, $v = 15\,\mathrm{mm\,s^{-1}}$, and since $\sigma = 6.6\,\mu\mathrm{m}$, the estimated reflection duration is 0.88 ms in good agreement with the fitted value.

The motion of the wave packets is also affected by the excitation frequency. The motion up to the point where the wave packet crosses the BEC is shown in figure 4.5 (a) for modulation frequencies 28, 32, and 36 kHz. It is clear that the wave packet moves further out at higher modulation frequencies as expected, owing to the larger kinetic energy obtained by the excitation.

The effect of varying the modulation frequency may be estimated by noting that the turning point follows the band gap between the 2nd and 3rd bands. This band gap is quadratic in position due to the magnetic trap, but is offset by the transition energy from 0th to 3rd excited band, $h\,\nu_{03}$. Energy balance thus requires that at the reflection point, the potential energy matches the modulation energy

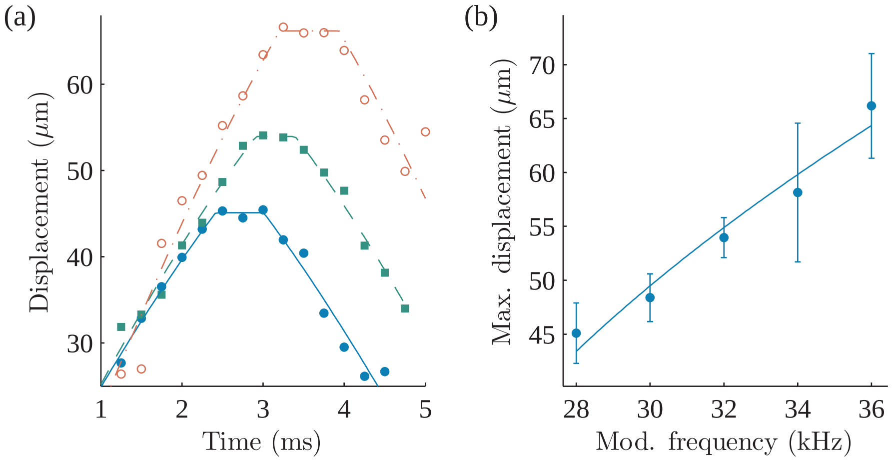

FIGURE 4.5: Motion of the upper wave packet at different excitation frequencies. *(a)* Traces of wave packet motion during the first half oscillation for $\nu_{\mathrm{mod}} = 28\,\mathrm{kHz}$ (blue, filled circles, solid), 32 kHz (green, squares, dashed), and 36 kHz (red, open circles, dot-dashed). *(b)* Maximal displacement for the wave packet at different modulation frequencies. Error bars are extracted from fits.

$2h\,\nu_{\mathrm{mod}}$

$$2h\,\nu_{\mathrm{mod}} = h\,\nu_{03} + \tfrac{1}{2} M \omega_{\mathrm{r}}^2 y^2. \tag{4.5}$$

This may be solved for the position

$$y = \sqrt{\frac{4h}{M\omega_{\mathrm{r}}^2}\left(\nu_{\mathrm{mod}} - \tfrac{1}{2}\nu_{03}\right)}. \tag{4.6}$$

Since the trap frequency is well-known, the only variable in this expression is the transition frequency ν_{03}, which was used for fitting in figure 4.5 (b). The resulting value of ν_{03} is 42.6(6) kHz and 40.2(8) kHz for the upper and lower wave packet, respectively. The fitted values agree with the value of 41.1 kHz obtained from the band structure calculation.

4.2 Deexcitation of wave packets

Localised states

The process of creating wave packets may be reversed by applying lattice modulation to wave packets oscillating in the quasi-continuum. This deexcites the

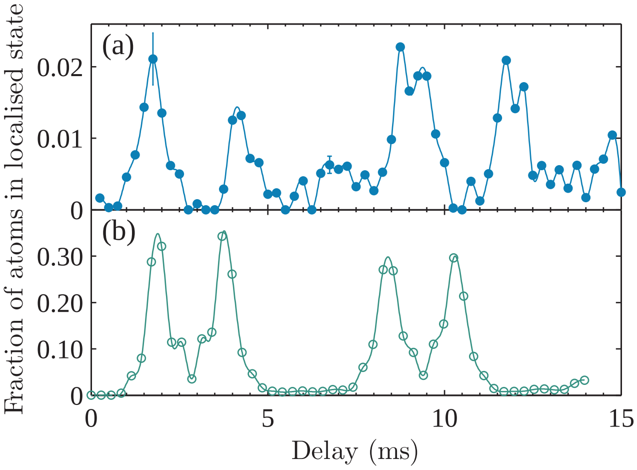

FIGURE 4.6: Deexcitation of wave packet versus evolution time. *(a)* Experimental data using a modulation frequency of 32 kHz. *(b)* Simulated data using a modulation frequency of 28 kHz (see text).

wave packet into a lower lattice band in a process similar to stimulated emission. The process is illustrated in figure 4.2 by arrows 2, and for a given modulation frequency, the deexcitation is only possible in a narrow spatial region. Furthermore, the deexcited states are localised, having a large density of states only in a region given by the band width. The deexcited atoms would hence be trapped at this position, unable to interact with the main condensate.

To test this interpretation, wave packets were excited at 32 kHz and another modulation pulse was applied after a variable evolution time. The atom number in the localised state was normalised to the total atom number, and is shown in figure 4.6 (a). The data shows a double peak structure centred at the wave packet reflection time, corresponding to resonant deexcitation before and after Bragg reflection. The process repeats itself after the wave packets have traversed the main peak.

The simulations shown in figure 4.6 (b) exhibit the same behaviour. The process was simulated by a single-particle time-dependent Schrödinger approach, starting from the spectrum of the time-independent Hamiltonian shown in figure 4.2. Using the ground state, $q = 0$ in the 0th band, as initial state, the atom is coupled to the quasi-continuum via the 2nd excited band using the matrix element $\langle f|\cos^2(ky)|i\rangle$ in accordance with equation (2.113). The population in the quasi-continuum is then evolved under the time-independent Hamiltonian for a variable time before coupling it back to the localised states. The data shown in figure 4.6 (b) is the resulting population in the localised states versus time.

The simulations were performed at a lower modulation frequency than the experiments in order to observe dynamics. At 32 kHz, no coupling to the continuum was observed, so a frequency of 28 kHz was chosen. We attribute this discrepancy to the fact that only $q = 0$ was chosen as the starting point for the simulations. For a real BEC, the extent of the condensate allows excitation to occur at other values of q as indicated by the arrows in figure 4.2 (b).

The simulations show qualitatively the same behaviour as the experiments, but there are two key differences: Firstly, the timing of the localised population does not match. This we attribute to the difference in modulation frequency between experiments and simulations. The simulations use a lower frequency, so it is expected that the Bragg reflection occurs earlier in the simulations than in the experiments.

The second difference between experiment and simulation is the large discrepancy in the deexcitation efficiency. For the experimental data, only a few percent of the total population is deexcited to localised states whereas the simulations show a factor of ten larger population. We attribute this discrepancy to interaction effects.

To control the deexcitation process, three parameters are available: The frequency, amplitude and duration of the modulation pulse. Each of these may be adjusted to tune the properties of the resulting localised states.

The effect of varying the deexcitation frequency was investigated by exciting wave packets, letting them evolve for 2 ms and then applying a deexcitation pulse with variable frequency. The results are shown in figure 4.7 as a deexcitation spectrum.

In the spectrum, three peaks are visible: 19.1(1), 31.10(7) and 47.7(7) kHz. These three peaks may be identified with transfer to the 2nd excited, 1st excited and 0th band respectively. A comparison with figure 4.2 shows that the expected transition energies are 6.3, 11.8 and $18.1 E_\mathrm{r}$, respectively; these correspond to 17.3, 32.4 and 49.7 kHz in good agreement with data.

The experimental method for obtaining the data in figure 4.7 was modified to prevent atoms from tunnelling out of the partially trapped 2nd band. To this end, the lattice was ramped to $22.5 E_\mathrm{r}$ over 1 ms right after the modulation pulse, in order to keep atoms in the lattice. Following this, the magnetic trap was ramped down over 5 ms, and the atoms were held for another 12 ms in the lattice to remove the remaining wave packet before imaging.

Another complication was the possibility of transferring atoms to the 1st band in a two-step process when addressing the 2nd band. We have verified that there are no atoms in the 1st band when using the low modulation amplitude of $\epsilon = 0.15$.

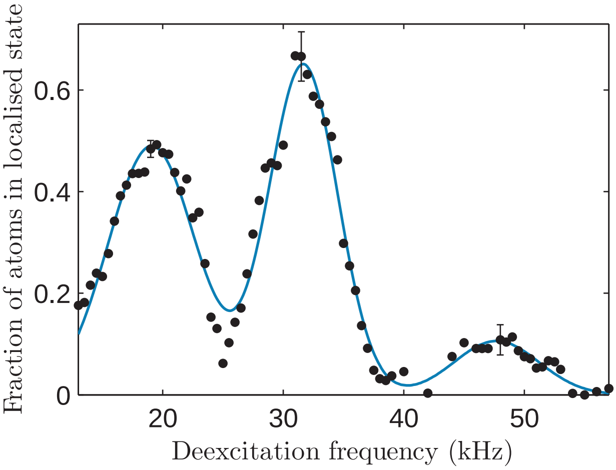

FIGURE 4.7: Deexcitation spectrum. Wave packets were deexcited with a lattice modulation pulse of variable frequency. The data has been fitted with a triple Gaussian function yielding resonance 19.1, 31.7, and 47.7 kHz. Representative error bars are shown at 19.0, 31.5 and 48 kHz.

It should also be noted that the transfer of atoms from the 3rd to the 2nd band in figure 4.7 does not violate the selection rule of $\Delta n = 2$. This rule only applies strictly for parity eigenstates, but here the effect is to lower the transfer rate for odd Δn.

In figure 4.8, the amplitude of the modulation pulse was varied for each of the transitions shown in figure 4.7. The deexcitation efficiency increases approximately linearly with modulation amplitude, but beyond $\epsilon = 0.2$, the efficiency saturates. This is attributed to non-linear effects such as reexcitation of atoms into the wave packet. The 1st excited band can be populated with highest efficiency owing to the fact that it is a $\Delta n = 2$ transition. In contrast, the 0th and 2nd excited band are limited at 15% and 50% respectively. Nonetheless, the data shows that the amplitude of the lattice modulation may be used to split the wave packet into a stationary and a moving part. The inset of figure 4.8 shows the effect of varying the duration of the deexcitation pulse when using 32 kHz and $\epsilon = 0.17$. A fit using equation (4.3) yields a time constant of $\tau = 132\,\mu\text{s}$ in agreement with the excitation pulse. This result also validates the choice of $500\,\mu\text{s}$ pulses for deexcitation.

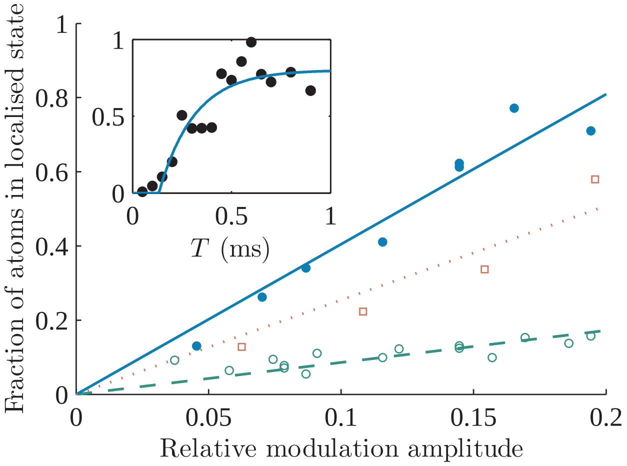

FIGURE 4.8: Deexcitation efficiency for different modulation amplitudes. Data is shown for the fraction of atoms transferred to the 0th band (open circles, red) for the 1st excited band (filled circles, blue) and for the 2nd excited band (squares, green). A linear fit has been applied to each of the data series, and only the linear regime is shown. *(Inset)* Deexcitation efficiency versus modulation pulse duration. The vertical axis is the same for both figures. The data has been fitted with an exponential saturation function yielding a time constant of $\tau = 132\,\mu\text{s}$.

Position control of localised states

From figure 4.2 (a), it is clear that the deexcitation frequency changes with the position of the wave packet. Conversely, the position of the deexcited state may be controlled by choosing the correct delay between excitation and deexcitation and the corresponding modulation frequency.

In figure 4.9, the potential of the trap has been mapped out by varying the modulation frequency. A pair of wave packets were excited by sweeping the modulation frequency from 27.5 to 28.5 kHz. This makes the wave packets temporally broad, which was advantageous for finding the optimal deexcitation frequency. For delays between 0.1 and 2 ms, the deexcitation frequency was scanned, and the cloud was held for another 10 ms only in the lattice to let the remainder of the wave packet tunnel out. Afterwards, the optimal frequency was found from the maximal transfer, and the position of the localised states was found by fitting a Gaussian profile to the cloud.

The trap potential shows a significant anharmonicity which can be quantified

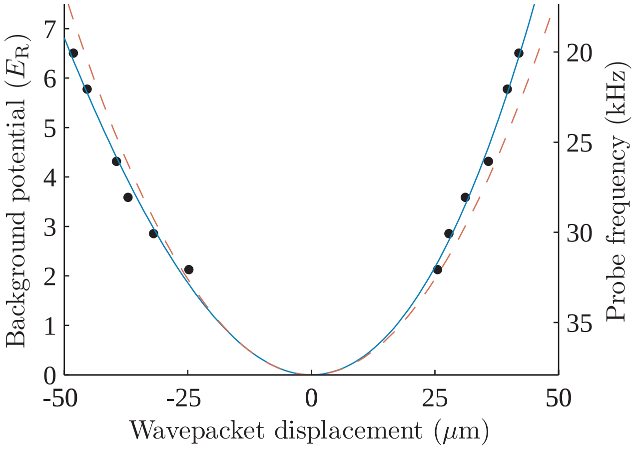

FIGURE 4.9: Spectroscopy of the trap potential by varying the deexcitation frequency. Two fits have been applied to the data: a cubic equation (blue, solid) and a quadratic equation (green, dashed).

by fitting a cubic polynomial

$$E_{\mathrm{bg}} = a y^3 + b y^2 + c, \tag{4.7}$$

where the linear term has been omitted in order to keep the centre of the trap fixed. Comparing this to a normal quadratic equation $E_{\mathrm{bg}} = b' y^2 + c'$, shows that the quadratic fit yields a χ^2 value that is 9.3 times larger than the one obtained from the cubic fit, i.e. the cubic equation gives a better fit, and the trap is anharmonic.

The anharmonicity is caused by several factors such as gravity (since the wave packets always travel along the vertical lattice) and misalignment of the optical lattice with respect to the magnetic trap. Simulations of the magnetic trap show that the anharmonicity caused by gravity is three orders of magnitude lower than what is measured in the experiments, so the primary cause of the anharmonicity must be due to misalignment of the optical lattice with respect to the magnetic trap.

The timing between the excitation and deexcitation pulse may also be exploited to create more complicated structures. If a first modulation pulse is applied at a large frequency and using a short delay and low amplitude, a pair of localised states will be created close to the main BEC and around 50% of the wave packet will propagate onwards. A second modulation pulse may be applied later using a lower frequency and high amplitude in order to deexcite all remaining atoms to a localized state at the edge of the trap.

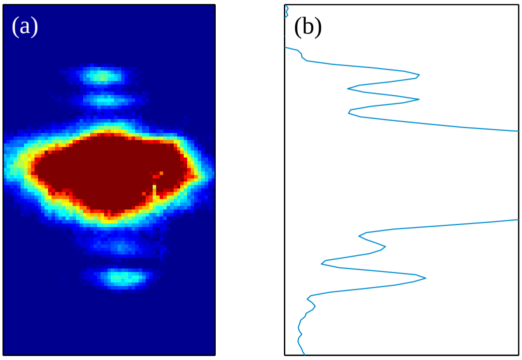

FIGURE 4.10: Double peaks created by splitting a wave packet with lattice modulation. *(a)* Absorption image of the cloud. *(b)* Optical density summed along the x axis, showing the relative size of the peaks.

This was realised by exciting wave packets at 33 kHz, and deexciting first at 36 kHz after 1.5 ms and then at 26 kHz after 2.0 ms. The result is the double-peak structure shown is figure 4.10. This demonstrates the ability to store two sets of atoms in a register, and the mechanism could be extended to more clouds by using a more decompressed trap.

A final tool to manipulate the localised atoms is by applying RF radiation in order to expel atoms from the trap. This is possible due to the large gravitational sag in the decompressed trap,

$$y_{\mathrm{sag}} = \frac{g}{\omega_{\mathrm{r}}^2} = 173\,\mu\mathrm{m}, \tag{4.8}$$

where g is the gravitational acceleration. The atoms are hence dragged far away from the centre of the magnetic trap, and they are located on a magnetic gradient that balances gravity as shown in figure 4.11. Due to the magnetic gradient, the atoms experience a unique magnetic potential which can be used for RF addressing.

Sweeping the frequency of RF radiation makes it possible to remove the atoms in a given region of space. This is done experimentally by first applying a lattice modulation at 30 kHz for 10 ms. This produces a large population in the 4th band rather than the distinct wave packets, and as the atoms move into resonance with deexcitation at 30 kHz, they are transferred to the 1st band, creating a large population in the localised states.

Afterwards, a variable RF sweep was applied for 80 ms at the same power used for evaporative cooling. The effect of different sweeps is shown in figure 4.11. In

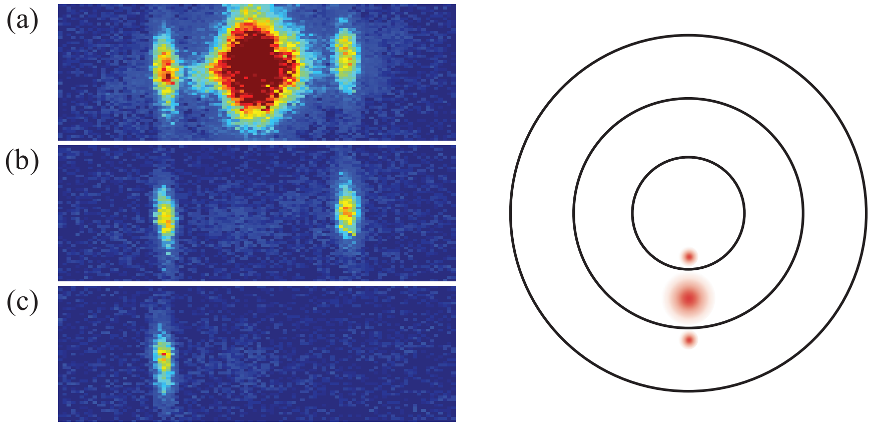

FIGURE 4.11: Localised states after RF sweep. *(Left)* Images have been turned 90° counter-clockwise, such that the upper wave packet is to the left. *(a)* No RF sweep. Localised states were created with 10 ms lattice modulation at 30 kHz. *(b)* RF sweep from 7650 to 7566 kHz. *(c)* RF sweep from 7700 to 7565 kHz. *(Right)* Sketch of the position of the clouds in the magnetic potential; the black lines indicate equipotential lines. The atoms are shifted away from the centre of the trap due to the gravitational sag. The clouds are thus located on a magnetic gradient.

(a), no sweep was applied, in (b) a sweep from 7650 to 7566 kHz removes the main BEC, and in (c) a sweep from 7700 to 7565 kHz removes both the lower wave packet as well as the main BEC.

This demonstrates the ability to manipulate localised states, and in the context of a quantum register, the RF cut can be thought of as a way of erasing an entry. Even though the RF sweep is relatively long, there is no clear effect of broadening or losses [78].

4.3 Multiply excited states

Another interesting aspect of the wave packets is the ability to create oscillating states of large momentum by applying additional excitation pulses. Conservation of momentum only allows further excitation in a small region of momentum space as indicated in figure 4.2 (a) by the arrows marked 3.

When wave packets are created, they start in the 4th exited band, but quickly move into the 3rd excited band. From there, another excitation transfers the atoms to the 5th excited band by absorbing two phonons carrying $2\hbar k_r$ of momentum.

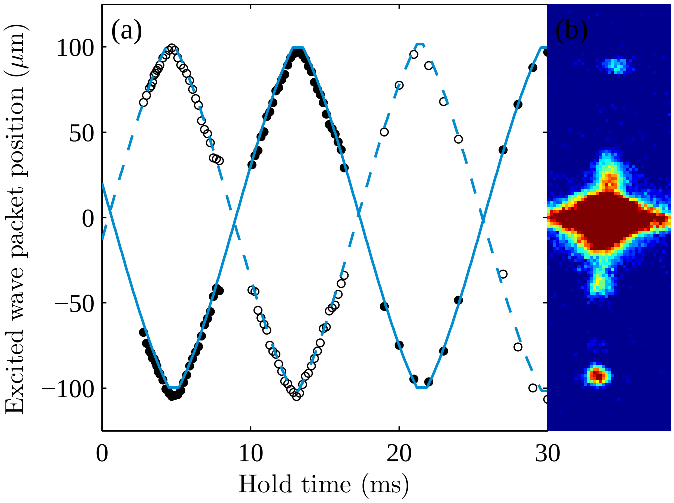

FIGURE 4.12: Multiply excited wave packets. *(a)* Position of lower wave packet (filled circles, solid line) and upper wave packet (open circles, dashed line). Both sets of data were fitted with equation (4.4). *(b) In situ* absorption image of the system after 4.5 ms hold time.

The atoms are thus transferred to the 5th Brillouin zone and the process is drawn as a "vertical transition" in the first Brillouin zone as shown in figure 4.2 (b).

This has been verified experimentally as shown in figure 4.12. Here, a wave packet pair was created by modulating the lattice at 31 kHz, and after 2 ms evolution another lattice modulation pulse at 52 kHz was applied. The large oscillation amplitude due to the absorption of two phonons is clear in the figure, and the path has an almost triangular shape due to the large momentum.

The larger oscillation amplitude agrees with the position space picture in figure 4.2 (a), since the band gap is shifted further outwards at the higher energy. It also agrees with the band pictures, since it will take the atoms longer time to reach the band gap from the 5th excited band.

The fact that the resonance depends on the position of the wave packet has been verified by repeating the excitation at different hold times. For each hold time, the excitation frequency was varied in order to map out the resonance structure. The result is shown as a spectrum in figure 4.13, and there are two trends: The resonance frequency decreases with increasing hold time, and the width increases with increasing hold time.

The decreasing centre frequency is consistent with the band structure in fig-

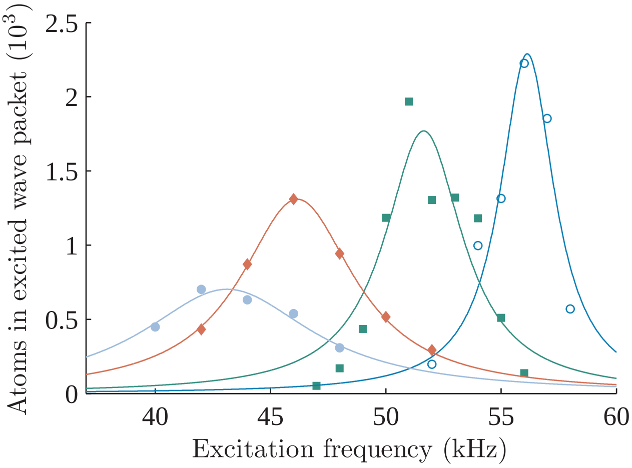

FIGURE 4.13: The excitation spectrum for multiply exciting a wave packet at different hold times. The initial wave packets were excited using 31 kHz, and for each hold time the number of atoms in the excited wave packet was measured for varying modulation frequencies. Data is shown for 0.6 ms (dark blue, open circles), 2.0 ms (green, squares), 2.9 ms (red, diamonds), and 3.3 ms (bright blue, filled circles). The data has been fitted with a Lorentzian to extract a centre frequency and a width.

ure 4.2 (b). The transition is marked with the arrows “3”, and the upper band is sloping more than the lower band, since the energy difference between the two bands will decrease as the wave packet “rolls down” the band.

The effect is shown more clearly in figure 4.14, where the resonance frequency is plotted against the delay between the two modulation pulses. The data may be analysed by assuming that the wave packet is propagating freely in a harmonic potential. For an atom in the q’th band, the momentum is $q\hbar k_\mathrm{r}$, and the modulation pulse adds another $2\hbar k_\mathrm{r}$ to the momentum. If the particle is free, the energy difference in the excitation process is

$$\frac{E'-E}{E_\mathrm{r}} = (q+2)^2 - q^2 = 4\big(1 + q_\mathrm{max}\cos[\omega_\mathrm{r}(t-t_0)]\big), \tag{4.9}$$

where q_max is the maximal momentum of the particle oscillating in the harmonic potential, and t_0 is a time offset to account for any delays in the excitation processes. Using this analytic model for fitting the data in figure 4.14 yields a maximal momentum of $q_\mathrm{max} = 4.16(1) k_\mathrm{r}$ and an offset of $t_0 = 0.21(2)\,\mathrm{ms}$. The fit is shown in red in figure 4.14 and matches the data well.

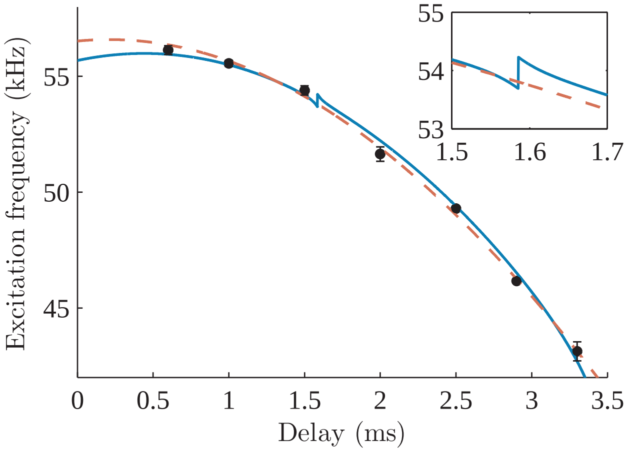

FIGURE 4.14: Centre frequency for the second excitation of a wave packet as function of time. Two fits are plotted: one using the analytical, free-space model, equation (4.9) (red, dashed), and one using the calculated band structure (blue, solid). *(Inset)* Zoom-in of the curve showing the kink in excitation frequency due to the crossing from the 4th to the 3rd excited band.

Alternatively, the data may be fitted using a numerical expression based on the calculated band structure of the system. Using the single-particle band structure calculation, the energy is calculated numerically for every value of the momentum $q_{\max}\cos[\omega_r(t-t_0)]$. The fit values are $q_{\max}=4.18(2)k_r$ and $t_0=0.44(4)\,\mathrm{ms}$.

The expected value of $q_{\max}$ is found by matching the 31 kHz of the excitation pulse with the band structure in figure 4.2, and extracting the corresponding momentum. This is found to be $4.22k_r$ in good agreement with both methods. The time offset indicates that the further excitation of a wave packet takes a finite time, and the difference in the value of t_0 suggests that the band structure has an influence on the duration.

The numerical fit exhibits a small kink in the dispersion (see inset of figure 4.14) which originates from the small band gap between the 3rd and 4th excited bands. This also shows that a transition from 4th to 6th band is driven for $t<1.5\,\mathrm{ms}$, and the transition is from 3rd to 5th band for $t>1.5\,\mathrm{ms}$.

In summary, a method for creating and storing wave packets in an optical lattice was presented. The experiments and the presented model show good agreement, indicating a good understanding of the system and the ability to control the excitation and deexcitation processes. The number of atoms localised after deexcitation can be controlled through the amplitude and duration of the modulation pulse, and the band where the atoms are localised can be chosen through the frequency of the pulse.

The system's ability to store atoms in the lattice makes it a candidate for a quantum register. It was shown that the number of localised states may be extended, and that the localised atoms can be manipulated by applying an RF sweep to expel atoms from the trap.

Finally, it was demonstrated that the opposite of the deexcitation – namely a further excitation of the wave packets – is possible. This allows for access to high momentum states in the magnetic trap, and the frequency of the modulation acts as a tool for band structure spectroscopy.

CHAPTER 5

SPIN DYNAMICS IN A TWO-DIMENSIONAL GEOMETRY

Spin-changing collisions lie at the heart of the field of spinor physics in degenerate quantum gases. Following the demonstration of coherent spin collisions [30, 31], the process has been studied under a wide variety of circumstances. The central phenomenon for coherence studies has been the spin oscillation, where a non-equilibrium spin state is prepared and allowed to evolve, showing oscillation between different spin states. The so-called single-mode approximation (SMA) is crucial for spin oscillations since it prevents any decoherence caused by population transferred to other spatial modes. The SMA is valid when the spin-healing length ξ_s is larger than the extent of the condensate, [82]

$$\xi_{\mathrm{s}} = \frac{2\pi\hbar}{\sqrt{2m|c|}}, \tag{5.1}$$

where c is the interaction energy associated with spin-changing collisions. The healing length describes the length scale over which excitations occur, so when it is larger than the condensate, no excitations are allowed [42, 44].

Using the SMA in the $F = 1$ manifold, the Chapman group observed spin oscillations and were able to interpret them using the model of an anharmonic oscillator. As the applied magnetic field was increased, the oscillation period diverged in analogy with the quasi-stable equilibrium of an inverted pendulum [31]. Further increase of the magnetic field leads to oscillations of another kind, as was demonstrated by the Lett group [33]. Using non-destructive imaging techniques they observed the crossing of the separatrix between oscillating and running phase dynamics.

Another approach to varying the quadratic Zeeman energy is to use microwave dressing of the hyperfine states [83]. This has the advantage of not being limited by the sign of the quadratic Zeeman energy (refer to equation (2.39)) and both sides of the q axis become experimentally accessible.

Similar experiments have been carried out in the Hamburg group using a degenerate fermi gas rather than a BEC. Using ^{40}K, they were able to observe the same kind of spin oscillations in a Mott insulating lattice as was observed by the Bloch group [30, 84]. However, since they had a total of 10 magnetic states available, oscillations were also observed for high-spin systems. Another surprising result of the fermionic spinor system was the observation of long-lived spin oscillations in an ensemble loaded into an optical dipole trap [85]. Although one would expect the oscillations to couple to the spatial structure leading to an immediate decoherence, the opposite was observed. Due to the fast dynamics of the spatial degrees of freedom, the spatially-dependent interactions averaged to zero, which effectively put the system in a single-mode regime.

Regarding the question of spatial excitations in a spin-changing collision, the Hannover group took a different approach using BECs. Here, spontaneous spin dynamics appeared as instabilities of the $|2, 0\rangle$ state leading to population in $|2, \pm 1\rangle$ [34–37, 86]. They were able to identify various spatial modes as the magnetic field was varied including superpositions of nearly degenerate modes.

Our experiments are taken to an explicit multi-mode regime, where several modes are needed to account for the spatial structure. This leads to clouds that have a significantly different appearance than the eigenmodes observed in previous experiments. This chapter is based on the work presented in [87].

5.1 Theoretical description

In this section, we shall expand on the Hamiltonian that was derived in chapter 2 and apply it to a 2D setting. This leads to a spectrum of unstable modes and expressions for the time-evolution of the unstable modes. The content of this section is based on work by Frank Deuretzbacher [49].

Spinor Hamiltonian in 2D

Starting from the expression (2.34) on page 16, we can describe a spin-2 system in the linear regime. In this section, this Hamiltonian will be applied to a BEC in a deep one-dimensional lattice.

In a single lattice site, the atoms will form an independent BEC decoupled from the other sites. For such a site, the trapping frequencies are given by equation (2.101). For an optical lattice of 914 nm and a beam waist of 100 µm, the ratio $\omega_z/\omega_r \approx 500$, so for low energies, the atoms will be “frozen” along the lattice direction. We may write the fields as

$$\begin{aligned} \psi_0(\boldsymbol{r}) &\approx \phi_z(z)\psi_0\big(\boldsymbol{\rho}\big) \\ \delta\hat{\psi}_{\pm1}(\boldsymbol{r}) &\approx \phi_z(z)\delta\hat{\psi}_{\pm1}\big(\boldsymbol{\rho}\big), \end{aligned} \tag{5.2}$$

where ϕ_z is the harmonic ground state

$$\phi_z(z) = \frac{1}{\sqrt{\sqrt{\pi}\,l_z}} e^{-z^2/(2l_z)^2}, \tag{5.3}$$

and $l_z = 1/(s^{1/4}k)$ is the longitudinal harmonic oscillator length.

The explicit z-dependence allows for the integration along z in equation (2.34)

$$\begin{aligned} \hat{H} - \mu\hat{N} &= \int \mathrm{d}^2\rho\, \psi_o^* \bigg(\hat{\tilde{H}}_0 + \tfrac{1}{2}\hbar\omega_z + \tfrac{1}{2}U_0 \int \mathrm{d}z\, \left|\phi_z\right|^4 \left|\psi_0\right|^2 - \mu \bigg) \psi_0 \\ &+ \sum_{m=\pm1} \int \mathrm{d}^2\rho\, \delta\hat{\psi}_m^\dagger \bigg(\hat{\tilde{H}}_0 + \tfrac{1}{2}\hbar\omega_z + (U_0 + U_1) \int \mathrm{d}z\, \left|\phi_z\right|^4 \left|\psi_0\right|^2 - \mu + q \bigg) \delta\hat{\psi}_m \\ &+ U_1 \int \mathrm{d}z\, \left|\phi_z\right|^4 \int \mathrm{d}^2\rho\, \left|\psi_0\right|^2 \big(\delta\hat{\psi}_1^\dagger \delta\hat{\psi}_{-1}^\dagger + \delta\hat{\psi}_1 \delta\hat{\psi}_{-1} \big), \end{aligned} \tag{5.4}$$

where $\hat{\tilde{H}}_0 = -\frac{\hbar^2}{2M}\nabla^2 + \frac{1}{2}M\omega_r^2\rho^2$. Performing the integration, we may reduce the Hamiltonian to

$$\begin{aligned} \hat{H} - \mu\hat{N} = \int \mathrm{d}^2\rho\, \psi_o^* \big(\hat{\tilde{H}}_0 + \tfrac{1}{2}\tilde{U}_0 \left|\psi_0\right|^2 - \tilde{\mu} \big) \psi_0 & \\ + \sum_{m=\pm1} \int \mathrm{d}^2\rho\, \delta\hat{\psi}_m^\dagger \big(\hat{\tilde{H}}_0 + (\tilde{U}_0 + \tilde{U}_1) \left|\psi_0\right|^2 - \tilde{\mu} + q \big) \delta\hat{\psi}_m & \\ + \tilde{U}_1 \int \mathrm{d}^2\rho\, \left|\psi_0\right|^2 \big(\delta\hat{\psi}_1^\dagger \delta\hat{\psi}_{-1}^\dagger + \delta\hat{\psi}_1 \delta\hat{\psi}_{-1} \big), & \end{aligned} \tag{5.5}$$

where the effective 2D parameters $\tilde{U}_0$, $\tilde{U}_1$ and $\tilde{\mu}$ have been introduced

$$\begin{aligned} \tilde{U}_0 &= U_0 \int \mathrm{d}z\, \left|\phi_z\right|^4 = \frac{U_0}{l_z\sqrt{2\pi}}, \\ \tilde{U}_1 &= \frac{U_1}{l_z\sqrt{2\pi}}, \\ \tilde{\mu} &= \mu - \frac{\hbar\omega_z}{2}. \end{aligned} \tag{5.6}$$

As previously mentioned, the dynamics of $|0\rangle$ is decoupled from that of $|\pm 1\rangle$, which means that we can include the influence of $|0\rangle$ on $|\pm 1\rangle$ without having to consider the back-action of $|\pm 1\rangle$ on $|0\rangle$. Taking the first line in equation (5.5) and minimising the energy leads to a Gross-Pitaevskii type equation

$$\left(-\frac{\hbar^2}{2M}\nabla^2 + \tfrac{1}{2}M\omega_r^2\rho^2 + \tilde{U}_0\left|\psi_0\right|^2\right)\psi_0 = \tilde{\mu}\psi_0. \tag{5.7}$$

This equation may be taken to the Thomas-Fermi regime as in section 2.1, which yields the radial structure of atoms in $|0\rangle$

$$n_0(\rho) = \frac{\tilde{\mu}}{\tilde{U}_0}\left(1 - \frac{\rho^2}{\rho_0^2}\right), \tag{5.8}$$

where ρ_0 is the Thomas-Fermi radius

$$\rho_0 = \sqrt{\frac{2\tilde{\mu}}{M\omega_\rho^2}}. \tag{5.9}$$

The effective chemical potential and Thomas-Fermi radius is given by the normalisation criterion

$$\begin{aligned} N &= \int \mathrm{d}^3\rho\, n_0(\boldsymbol{\rho}) = \frac{\pi\tilde{\mu}^2}{M\omega_\rho^2\tilde{U}_0}, \\ \tilde{\mu} &= \hbar\omega_\rho\left(\frac{8}{\pi}\right)^{1/4}\sqrt{\frac{Na_{\mathrm{av}}}{l_z}}, \\ \rho_0 &= \sqrt{2}\left(\frac{8}{\pi}\right)^{1/8} l_z\left(\frac{Na_{\mathrm{av}}}{l_z}\right)^{1/4}, \end{aligned} \tag{5.10}$$

where a_{av} is the scattering length associated with U_0 described by the linear combination (2.35).

Turning our attention to $|\pm 1\rangle$, we may write only the Hamiltonian for this part of the system

$$\begin{aligned} H_{\pm 1} = &\sum_{m=\pm 1}\int \mathrm{d}^2\rho\, \delta\hat{\psi}_m^\dagger\left(\hat{\tilde{H}}_0 + (\tilde{U}_0 + \tilde{U}_1)n_0(\rho) - \tilde{\mu} + q\right)\delta\hat{\psi}_m \\ &+ \tilde{U}_1\int \mathrm{d}^2\rho\, n_0(\rho)\left(\delta\hat{\psi}_1^\dagger\delta\hat{\psi}_{-1}^\dagger + \delta\hat{\psi}_1\delta\hat{\psi}_{-1}\right). \end{aligned} \tag{5.11}$$

If expression (5.8) is inserted into equation (5.11), the term $\tilde{U}_0 n_0$ exactly cancels the terms from the harmonic trap and the chemical potential for $\rho < \rho_0$. This

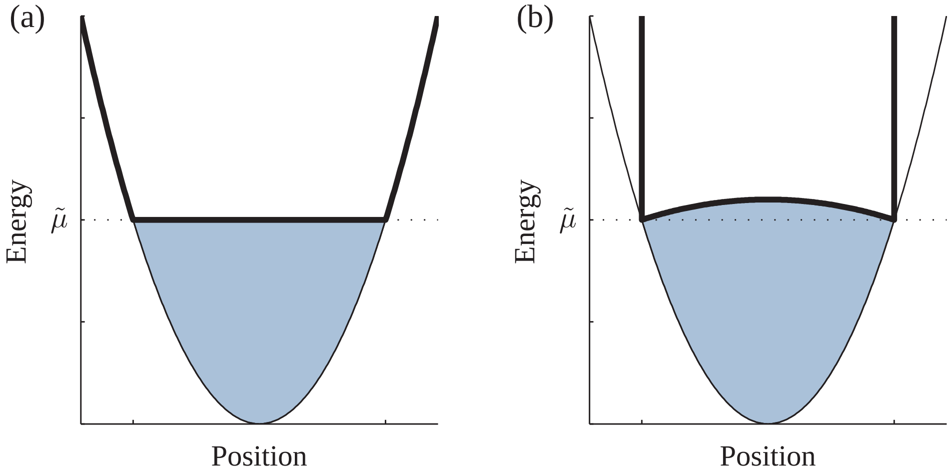

FIGURE 5.1: Effective potential in Thomas-Fermi approximation. *(a)* Potential experienced by a $|0\rangle$ atom. The trap potential is the thin black line, the $|0\rangle$ condensate is the blue area, and the effective potential is the wide black line. *(b)* Potential for $|\pm1\rangle$ in the hard-wall approximation. The repulsive term has been exaggerated for clarity.

is illustrated in figure 5.1 (a). The remaining non-linear term adds an additional repulsion of the same functional shape as n_0, but scaled by $\tilde{U}_1/\tilde{U}_0$. The decoupling of the $|0\rangle$ and $|\pm1\rangle$ amounts to an effective potential as shown in figure 5.1 (b).

To gain more insight into the eigenstates of the Hamiltonian, we make the *hard-wall approximation*, i.e. we approximate the harmonic trap potential by an infinite potential as shown in figure 5.1 (b). This is reasonable since over the energies we are interested in, $|q| < 500\,\mathrm{Hz}$, the trap radius is approximately constant.

Thus, when restricted to $\rho < \rho_0$, we may write the Hamiltonian as

$$\begin{aligned} H_{\pm1} = \sum_{m=\pm1} \int \mathrm{d}^2\rho\, \delta\hat{\psi}^\dagger_m \left(-\frac{\hbar^2}{2M}\nabla^2 + \tilde{U}_1 n_0(\rho) + q\right) \delta\hat{\psi}_m \\ + \tilde{U}_1 \int \mathrm{d}^2\rho\, n_0(\rho) \left(\delta\hat{\psi}^\dagger_1 \delta\hat{\psi}^\dagger_{-1} + \delta\hat{\psi}_1 \delta\hat{\psi}_{-1}\right). \end{aligned} \tag{5.12}$$

The great advantage of the hard-wall approximation is that the eigenstates of the effective potential are easily found. For the infinite cylindrical well, the eigenstates are

$$\phi_{nl}(\rho,\varphi) = \frac{1}{\sqrt{\pi}\rho_0 J_{|l|+1}(\beta_{nl})} J_{|l|}\left(\beta_{nl}\frac{\rho}{\rho_0}\right) e^{il\varphi} \tag{5.13}$$

with the corresponding eigenenergies

$$\epsilon_{nl} = \frac{\hbar^2 \beta_{nl}^2}{2m\rho_0^2}. \tag{5.14}$$

Here, J_l is the Bessel function of the first kind of l'th order and β is the n'th zero point of J_l.

There are a few important remarks to be made about this class of functions. Firstly, there is no boundary on n given the choice of l and vice versa; for all functions, $l = 0, \pm 1, \pm 2, \ldots$ and $n = 1, 2, 3, \ldots$. Secondly, there is degeneracy between $\pm l$, since the two functions only differ in sign. Hence, the only difference between $\pm l$ is in the phase factor, and one may identify l as the angular momentum. This is also supported by the observation that only $l = 0$ has a non-zero value at $\rho = 0$ consistent with the appearance of vortices in a rotating condensate. Lastly, the phase factor $e^{il\varphi}$ ensures orthogonality in l and the radial part of the Bessel functions are orthogonal in n for a given l.

The field operator $\delta\hat{\psi}_m$ can be expanded on the functions ϕ_{nl},

$$\delta\hat{\psi}_m = \sum_{nl} \phi_{nl} \hat{a}_{nlm}, \tag{5.15}$$

where $\hat{a}_{nlm}$ is the annihilation operator for an atom in the spatial state ϕ_{nl} and spin state m. Insertion of this expansion into equation (5.13) is trivial for the kinetic energy term, since this yields the eigenenergy ϵ_{nl}, and also for the q term, since ϕ_{nl} are orthonormal. The matrix element $\tilde{U}_1 \langle \phi_{nl} | n_0 | \phi_{n'l'} \rangle$ however, requires closer inspection.

It is clear, that since n_0 is real, the phase factor in ϕ_{nl} still ensures orthogonality. We may thus write the matrix element in terms of a dimensionless integral $I_{nn'l}$

$$\tilde{U}_1 \langle \phi_{nl} | n_0 | \phi_{n'l'} \rangle = \delta_{ll'} \frac{U_1}{U_0} \tilde{\mu} I_{nn'l}, \tag{5.16}$$

where the integral is given by

$$\begin{aligned} I_{nn'l} &= \int \mathrm{d}^2\rho \, \phi_{nl}^*(\rho) \, n_0(\rho) \, \phi_{n'l}(\rho). \\ &= \frac{2}{\rho_0^2 J_{|l|+1}(\beta_{nl}) \, J_{|l|+1}(\beta_{n'l})} \int_0^{\rho_0} \mathrm{d}\rho \, \rho \left(1 - \frac{\rho^2}{\rho_0^2}\right) J_{|l|}\!\left(\beta_{nl} \frac{\rho}{\rho_0}\right) J_{|l|}\!\left(\beta_{n'l} \frac{\rho}{\rho_0}\right) \\ &= \frac{2}{J_{|l|+1}(\beta_{nl}) \, J_{|l|+1}(\beta_{n'l})} \int_0^1 \mathrm{d}u \, u (1 - u^2) J_{|l|}(\beta_{nl} u) \, J_{|l|}(\beta_{n'l} u). \end{aligned} \tag{5.17}$$

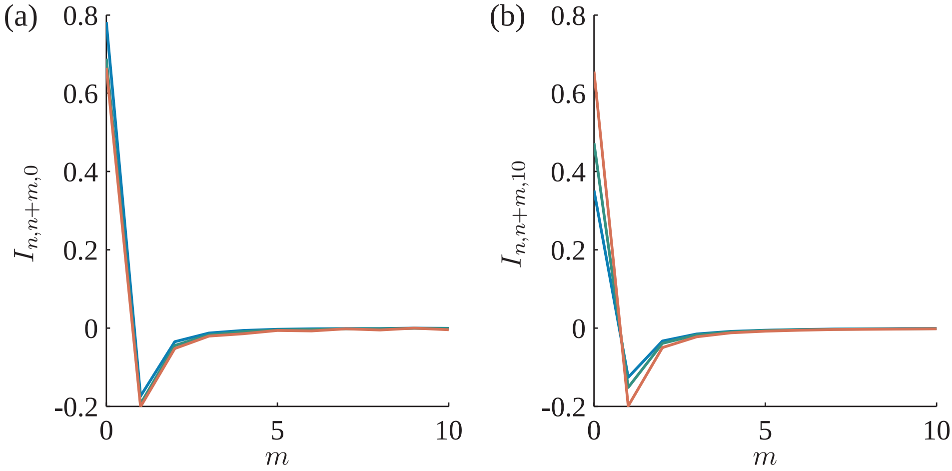

FIGURE 5.2: Numerical evaluation of the overlap integral for increased difference between n and $n' = n + m$. *(a)* $l = 0$. *(b)* $l = 10$. For both figures: $n = 1$ (blue), $n = 2$ (green), $n = 20$ (red). It is clear that the integral quickly converges towards zero for increasing m.

A numerical evaluation of the integral shows that for $n \neq n'$, the integral assumes a much smaller value than for $n = n'$ (figure 5.2). As the difference between n and n' is increased, $I_{nn'l}$ quickly converges to zero, which is illustrated for $l = 0$ in figure 5.2 (a) and for $l = 10$ in figure 5.2 (b). It is therefore reasonable to approximate the matrix element by

$$\tilde{U}_1 \langle \phi_{nl} | n_0 | \phi_{n'l'} \rangle = \delta_{ll'} \delta_{nn'} \frac{U_1}{U_0} \tilde{\mu} I_{nn'll'} \equiv \frac{U_1}{U_0} \tilde{\mu} I_{nl} \tag{5.18}$$

The physical content of this approximation is that the particles that undergo spin-changing collisions always populate the same spatial mode. Each collisional event will thus be spatially symmetric.

Applying this approximation yields the simplified Hamiltonian

$$\begin{aligned} H_{\pm 1} = & \sum_{nl} \left(\epsilon_{nl} + \tilde{U}_1 \langle n_0 \rangle_{nl} + q \right) \left(\hat{a}^\dagger_{nl1} \hat{a}_{nl1} + \hat{a}^\dagger_{nl-1} \hat{a}_{nl-1} \right) \\ & + \tilde{U}_1 \sum_{nl} \langle n_0 \rangle_{nl} \left(\hat{a}^\dagger_{nl1} \hat{a}^\dagger_{n-l-1} + \hat{a}_{nl1} \hat{a}_{n-l-1} \right). \end{aligned} \tag{5.19}$$

From this equation it is clear that the dynamics of spin-changing collisions is governed by the matrix element $\langle n_o \rangle_{nl}$ which basically is set by the overlap between

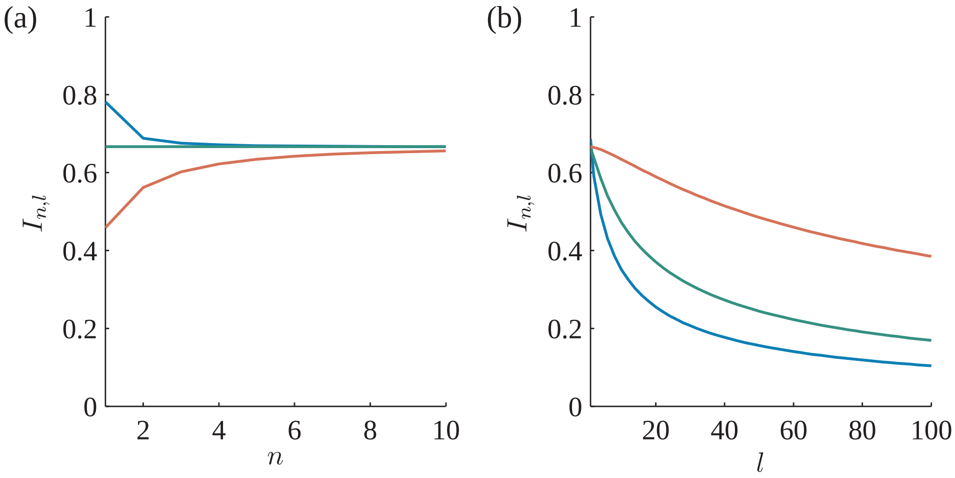

FIGURE 5.3: Numerical evaluation of the diagonal integral I_{nl}. *(a)* Dependence on n for $l = 0$ (blue), $l = 1$ (green), and $l = 5$ (red). *(b)* Dependence on l for $n = 1$ (blue), $n = 2$ (green), $n = 10$ (red). The convergence towards $2/3$ is clear in (a), whereas (b) shows that convergence towards zero is slower with increasing n.

an exited state ϕ_{nl} and the $|0\rangle$ condensate. However, this is an overlap of densities, and therefore I_{nl} does not converge to zero for large n, as is the case for wave functions in general.

This behaviour is illustrated in figure 5.3 (a), where the integral clear converges towards $2/3$ with increasing n. This limit changes slowly with l as shown in figure 5.3 (b), so the overlap only vanishes in the limit of l approaching infinity.

Bogoliubov spectrum

So far, the spinor Hamiltonian of $|\pm1\rangle$ has been simplified by making a number of approximations. The resulting Hamiltonian (5.19) can be simply diagonalised by a Bogoliubov transformation[1].

To do this, the Hamiltonian needs to be in a symmetric form. The current form contains terms of both $\hat{a}_{nl1}$, $\hat{a}_{nl-1}$ and $\hat{a}_{n-l-1}$, so we start by rearranging the terms, to make the symmetry apparent. First, we define the quantities

$$\begin{aligned} D_{n,l} &\equiv \epsilon_{nl} + \tilde{U}_1 \langle n_0 \rangle_{nl} + q, \\ U_{n,l} &\equiv \tilde{U}_1 \langle n_0 \rangle_{nl} . \end{aligned} \tag{5.20}$$

---

[1] The details of the Bogoliubov transformation are covered in appendix A.

This allows for the shorter expression

$$\hat{H} = \sum_{n,l} D_{n,l} \left(\hat{a}^{\dagger}_{nl1} \hat{a}_{nl1} + \hat{a}^{\dagger}_{nl-1} \hat{a}_{nl-1} \right) + \sum_{n,l} U_{n,l} \left(\hat{a}^{\dagger}_{nl1} \hat{a}^{\dagger}_{n-l-1} + \hat{a}_{nl1} \hat{a}_{n-l-1} \right). \tag{5.21}$$

As mentioned earlier, the $\pm l$ modes are degenerate, so $D_{n,-l} = D_{n,l}$, and the sums may be taken only over positive l

$$\begin{aligned} \hat{H}_{\pm 1} = & \sum_{n,l>0} D_{n,l} \left(\hat{a}^{\dagger}_{nl1} \hat{a}_{nl1} + \hat{a}^{\dagger}_{nl-1} \hat{a}_{nl-1} + \hat{a}^{\dagger}_{n-l1} \hat{a}_{n-l1} + \hat{a}^{\dagger}_{n-l-1} \hat{a}_{n-l-1} \right) \\ & + \sum_{n,l>0} U_{n,l} \left(\hat{a}^{\dagger}_{nl1} \hat{a}^{\dagger}_{n-l-1} + \hat{a}_{nl1} \hat{a}_{n-l-1} + \hat{a}^{\dagger}_{n-l1} \hat{a}^{\dagger}_{nl-1} + \hat{a}_{n-l1} \hat{a}_{nl-1} \right) \\ & + \sum_{n} D_{n,0} \left(\hat{a}^{\dagger}_{n01} \hat{a}_{n01} + \hat{a}^{\dagger}_{n0-1} \hat{a}_{n0-1} \right) + \sum_{n} U_{n,0} \left(\hat{a}^{\dagger}_{n01} \hat{a}^{\dagger}_{n0-1} + \hat{a}_{n01} \hat{a}_{n0-1} \right). \end{aligned} \tag{5.22}$$

These terms may be rearranged into the symmetric form

$$\begin{aligned} \hat{H}_{\pm 1} = & \sum_{n,l>0} \Big[D_{n,l} \big(\hat{a}^{\dagger}_{nl1} \hat{a}_{nl1} + \hat{a}^{\dagger}_{n-l-1} \hat{a}_{n-l-1} \big) + U_{n,l} \big(\hat{a}^{\dagger}_{nl1} \hat{a}^{\dagger}_{n-l-1} + \hat{a}_{nl1} \hat{a}_{n-l-1} \big) \\ & + D_{n,l} \big(\hat{a}^{\dagger}_{n-l1} \hat{a}_{n-l1} + \hat{a}^{\dagger}_{n-l-1} \hat{a}_{n-l-1} \big) + U_{n,l} \big(\hat{a}^{\dagger}_{n-l1} \hat{a}^{\dagger}_{nl-1} + \hat{a}_{n-l1} \hat{a}_{nl-1} \big) \Big] \\ & + \sum_{n} \Big[D_{n,0} \big(\hat{a}^{\dagger}_{n01} \hat{a}_{n01} + \hat{a}^{\dagger}_{n0-1} \hat{a}_{n0-1} \big) + U_{n,0} \big(\hat{a}^{\dagger}_{n01} \hat{a}^{\dagger}_{n0-1} + \hat{a}_{n01} \hat{a}_{n0-1} \big) \Big]. \end{aligned} \tag{5.23}$$

Each line of equation (5.23) is now self-contained, and each may undergo a Bogoliubov transformation. The double degeneracy of the system is also apparent in this form – both $\pm l$ and $m = \pm 1$ have the same energy. For simplicity, we only consider the first line of equation (5.23) in the following.

The Bogoliubov transformation applies to an interacting system of two kinds of particles and mix the particle operators into quasi-particle operators that do not interact. The transformation is famous from liquid helium where the pairing of particles with opposite momenta leads to superfluidity [44]. Equation (5.23) has the same form as the superfluidity Hamiltonian.

The Bogoliubov quasi-particle operators are defined as

$$\begin{aligned} \hat{\alpha} &= u \hat{a}_{nl1} + v \hat{a}^{\dagger}_{n-l-1}, \\ \hat{\beta} &= u \hat{a}_{n-l-1} + v \hat{a}^{\dagger}_{nl1}, \end{aligned} \tag{5.24}$$

where u and v are scalars that quantify the mixing of the constituent particles. Requiring commutativity between α and β leads to the convenient parametrisation

$$\begin{aligned} u &= \cosh(t), \\ v &= \sinh(t). \end{aligned} \tag{5.25}$$

Using the definition of the quasi-particle operators, the inverse transformation can be isolated and substituted back into the Hamiltonian, leading to the expression

$$\begin{aligned} H_{n,l} =& 2v^2 D_{n,l} - 2uvU_{n,l} + \left[D_{n,l}(u^2+v^2) - 2U_{n,l}uv\right](\hat{\alpha}^\dagger\hat{\alpha} + \hat{\beta}^\dagger\hat{\beta}) \\ &+ \left[U_{n,l}(u^2+v^2) - 2uvD_{n,l}\right](\hat{\alpha}^\dagger\hat{\beta}^\dagger + \hat{\alpha}\hat{\beta}). \end{aligned} \tag{5.26}$$

The cross-term may be eliminated through the freedom in choosing t. The resulting Hamiltonian may be put into the simple form

$$H_{n,l} = \sqrt{D_{n,l}^2 - U_{n,l}^2} - D_{n,l} + \sqrt{D_{n,l}^2 - U_{n,l}^2}\left(\hat{\alpha}^\dagger\hat{\alpha} + \hat{\beta}^\dagger\hat{\beta}\right). \tag{5.27}$$

From this expression it is clear, that the excitations are given by the number of quasi-particles $\hat{\alpha}^\dagger\hat{\alpha} + \hat{\beta}^\dagger\hat{\beta}$ and the addition of each particle increases the energy by $\sqrt{D_{n,l}^2 - U_{n,l}^2}$ which takes the form

$$E_{n,l} = \sqrt{(\epsilon_{nl} + \tilde{U}_1 \langle n_0\rangle_{nl} + q)^2 - (\tilde{U}_1 \langle n_0\rangle_{nl})^2}. \tag{5.28}$$

Since the quadratic Zeeman energy q is negative, the first term can be smaller than the second term, and the energy becomes imaginary. This is interpreted as an instability of the system, and in the linear regime, it manifests itself as en exponential growth or decrease in the population of $|\pm 1\rangle$.

The functional form of $\text{Im}\{E_{n,l}\}$ is that of a semicircle. The energy becomes imaginary when $q + \epsilon_{nl} = 0$, i.e. when the quadratic Zeeman energy is equal to the energy of ϕ_{nl}, and it reaches its maximal value of $\tilde{U}_1 \langle n_0\rangle_{nl}$ when $q + \epsilon_{nl} + \tilde{U}_1 \langle n_0\rangle_{nl} = 0$. The energy becomes real again when $q + \epsilon_{nl} + 2\tilde{U}_1 \langle n_0\rangle_{nl} = 0$, so the density n_0 sets the width of the resonances.

In an optical lattice, the density is typically very large due to the strong longitudinal confinement compared to the transversal direction. Thus, it is easy to design a setup where the width of the resonances is larger than the mode spacing. The resulting "instability spectrum" is shown in figure 5.4, for $\sim 9 \times 10^3$ atoms confined in a lattice of $w_0 = 102\,\mu\text{m}$ and $s = 18$. It is also clear that the stability rate converges towards a fixed value. This is due to the convergence of I_{nl} as seen in figure 5.3.

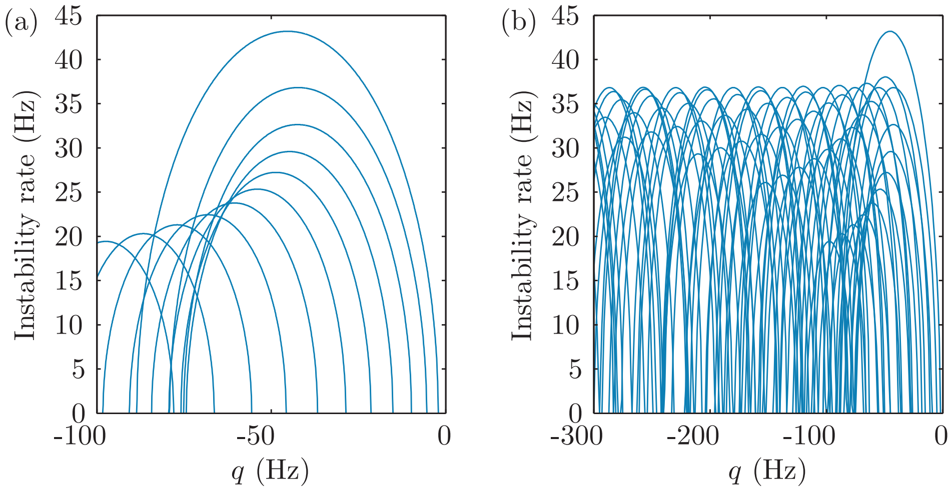

FIGURE 5.4: Instability rates for $|0\rangle$ in a single lattice site. Atom number: $\sim 9\times10^3$, $w_0 = 102\,\mu\text{m}$ and $s = 18$. *(a)* The modes $n = 0$, $l = 0, 1, \ldots, 10$. *(b)* All modes up to $B \approx 2$ G. The modes converge towards a finite value due to the behaviour of I_{nl}.

Time evolution of unstable modes

To investigate the time evolution of the unstable modes, it is advantageous to select a different Bogoliubov transformation [49, 86]

$$\begin{aligned} u &= \frac{e^{i\theta}}{\sqrt{2\sin(2\theta)}}, \\ v &= \frac{e^{-i\theta}}{\sqrt{2\sin(2\theta)}}, \\ \cos(2\theta) &= D_{n,l}/U_{n,l}. \end{aligned} \tag{5.29}$$

This choice of u and v fulfils the slightly altered commutation relation

$$u^2 - (v^*)^2 = i, \tag{5.30}$$

but the energy of the quasi-particles remains the same, as can be checked by inserting the back-substitution into the Hamiltonian (5.23). In matrix form, one may write the transformation as

$$\begin{pmatrix}\hat\alpha\\ \hat\beta^\dagger\end{pmatrix} = A\begin{pmatrix}\hat a\\ \hat b^\dagger\end{pmatrix} \qquad A = \frac{1}{\sqrt{2\sin(2\theta)}}\begin{pmatrix} e^{i\theta} & e^{-i\theta} \\ e^{-i\theta} & e^{i\theta}\end{pmatrix}, \tag{5.31}$$

where we have defined $\hat{a} \equiv \hat{a}_{nl1}$ and $\hat{b} \equiv \hat{a}_{n-l-1}$ for simplicity. This choice of Bogoliubov coefficients leads to the commutator

$$\left[\hat{\alpha},\, \hat{\beta}\right] = \left[\hat{\alpha}^{\dagger},\, \hat{\beta}^{\dagger}\right] = i, \tag{5.32}$$

whereas all other commutator combinations are zero. This unorthodox commutator yields to the simple Hamiltonian

$$\hat{H}_{n,l} = -iE_{n,l}\left(\hat{\alpha}^{\dagger}\hat{\beta}^{\dagger} + \hat{\alpha}\hat{\alpha}\right) + \frac{iE_{n,l}}{\tan(2\theta)}. \tag{5.33}$$

The commutator relations of the quasi-particle operator with the Hamiltonian are then

$$\begin{aligned} \left[\hat{H}_{n,l},\, \hat{\alpha}\right] &= E_{n,l}\hat{\alpha}, & \left[\hat{H}_{n,l},\, \hat{\alpha}^{\dagger}\right] &= E_{n,l}\hat{\alpha}^{\dagger}, \\ \left[\hat{H}_{n,l},\, \hat{\beta}\right] &= -E_{n,l}\hat{\beta}, & \left[\hat{H}_{n,l},\, \hat{\beta}^{\dagger}\right] &= -E_{n,l}\hat{\beta}^{\dagger}, \end{aligned} \tag{5.34}$$

and these are inserted in the Heisenberg equation of motion

$$\frac{d\hat{\alpha}(t)}{dt} = \frac{i}{\hbar}\left[\hat{H},\, \hat{\alpha}(t)\right] = -\frac{i}{\hbar}E_{n,l}\alpha(t). \tag{5.35}$$

Since $E_{n,l}$ is purely imaginary in this regime, the time evolution is not harmonic but exponential

$$\hat{\alpha}(t) = \hat{\alpha}(0)\, e^{\operatorname{Im} E_{n,l}\, t/\hbar}, \tag{5.36}$$

and similarly for $\hat{\alpha}^{\dagger}(t)$, whereas the time evolution for $\hat{\beta}$ and $\hat{\beta}^{\dagger}$ is decreasing as

$$\hat{\beta}(t) = \hat{\beta}(0)\, e^{-\operatorname{Im} E_{n,l}\, t/\hbar}. \tag{5.37}$$

This shows that the Bogoliubov mode $\hat{\beta}$ shows squeezing at the expense of stretching of $\hat{\alpha}$. This phenomenon is well-known from non-linear optics, where parametric down-conversion produces states where the quadratures are squeezed and stretched in similar fashion.

In the Bessel mode basis, the states mix under the time evolution operator. To see this, we use the Bogoliubov transformation (5.31), evolve the state in the quasi-particle basis and apply the back-transformation

$$A\begin{pmatrix} \hat{a}(t) \\ \hat{b}^{\dagger}(t) \end{pmatrix} = T(t)\begin{pmatrix} \hat{\alpha}(0) \\ \hat{\beta}^{\dagger}(0) \end{pmatrix} \tag{5.38}$$

$$\begin{pmatrix} \hat{a}(t) \\ \hat{b}^{\dagger}(t) \end{pmatrix} = A^{-1}T(t)A\begin{pmatrix} \hat{a}(0) \\ \hat{a}^{\dagger}(0) \end{pmatrix} \equiv M(t)\begin{pmatrix} \hat{a}(0) \\ \hat{a}^{\dagger}(0) \end{pmatrix} \tag{5.39}$$

The matrix M represents the time evolution operator in the Bessel mode basis and has the elements

$$M(t) = \begin{pmatrix} O(t) & \tilde{O}(t) \\ O^*(t) & \tilde{O}^*(t) \end{pmatrix} \tag{5.40}$$

that are defined by

$$\begin{aligned} O(t) &= -i\left(e^{\operatorname{Im} E_{n,l}\, t/\hbar} u^2 - e^{-\operatorname{Im} E_{n,l}\, t/\hbar} v^2\right) \\ &= \frac{1}{i\sin(2\theta)} \sinh\left(\frac{\operatorname{Im} E_{n,l}\, t}{\hbar} + i2\theta\right) \end{aligned} \tag{5.41}$$

and

$$\begin{aligned} \tilde{O}(t) &= -i\left(e^{\operatorname{Im} E_{n,l}\, t/\hbar} - e^{-\operatorname{Im} E_{n,l}\, t/\hbar}\right)|u|^2 \\ &= \frac{1}{i\sin(2\theta)} \sinh\left(\frac{\operatorname{Im} E_{n,l}\, t}{\hbar}\right). \end{aligned} \tag{5.42}$$

So under time-evolution, the modes a and b evolve as

$$\hat{a}(t) = O(t)\,\hat{a}(0) + \tilde{O}(t)\,\hat{b}^\dagger(0), \tag{5.43}$$

$$\hat{a}^\dagger(t) = O^*(t)\,\hat{a}^\dagger(0) + \tilde{O}^*(t)\,\hat{b}(0). \tag{5.44}$$

We may now calculate the expected atom number in mode a evolving from a vacuum state

$$\begin{aligned} N_a(t) &= \langle 0|_a \langle 0|_b\, \hat{a}^\dagger(t)\,\hat{a}(t)\,|0\rangle_a |0\rangle_b \\ &= \langle 0|_a \langle 0|_b \left(O^*(t)\,\hat{a}^\dagger(0) + \tilde{O}^*(t)\,\hat{b}(0)\right)\left(O(t)\,\hat{a}(0) + \tilde{O}(t)\,\hat{b}^\dagger(0)\right)|0\rangle_a |0\rangle_b\,. \\ &= \left|\tilde{O}(t)\right|^2 \\ &= \frac{\sinh^2\left(\operatorname{Im} E_{n,l}\, t/\hbar\right)}{\sin^2(2\theta)} \approx \frac{\exp\left(2\operatorname{Im} E_{n,l}\, t/\hbar\right)}{\sin^2(2\theta)}, \end{aligned} \tag{5.45}$$

since the $\hat{a}$ terms contribute nothing when acting on vacuum. This shows that the population rises exponentially on a time scale of $\hbar/2\operatorname{Im} E_{n,l}$. Also, since the initial state is vacuum, the process can be understood as a parametric amplification where the seed is vacuum fluctuations [35].

It now only remains to compute the distribution in a given mode after an evolution time t. For this, we construct an eigenvalue equation from the vacuum state

$$\hat{a}\,|0\rangle_a |0\rangle_b = 0. \tag{5.46}$$

This is true for all times, so application of the time evolution operator $e^{-i\hat{H}t/\hbar}$ yields

$$e^{-i\hat{H}t/\hbar}\hat{a}\,|0\rangle_a\,|0\rangle_b = 0. \tag{5.47}$$

Inserting the identity $e^{i\hat{H}t/\hbar}e^{-i\hat{H}t/\hbar}$ leads to the equation

$$\left(e^{-i\hat{H}t/\hbar}\hat{a}\,e^{i\hat{H}t/\hbar}\right)\left(e^{-i\hat{H}t/\hbar}\,|0\rangle_a\,|0\rangle_b\right) = 0. \tag{5.48}$$

The first parenthesis is actually the operator $\hat{a}$ evolved backwards in time, so this can be written as

$$\hat{a}(-t) = O(-t)\,\hat{a}(0) + \tilde{O}(-t)\,\hat{b}^\dagger(0). \tag{5.49}$$

The second parenthesis is exactly the time evolved state that we are looking for. Designating this state by $|\zeta(t)\rangle$, we may expand it in two-mode Fock states, because the Hamiltonian only contains terms that creates and annihilates particles in a and b simultaneously,

$$|\zeta(t)\rangle = \sum_{k=0}^{\infty} C_k(t)\,|k\rangle_a\,|k\rangle_b\,. \tag{5.50}$$

Equation (5.48) then takes the form

$$\sum_{k=0}^{\infty} C_k(t)\big[O(-t)\,\hat{a} + \tilde{O}(-t)\,\hat{b}^\dagger\big]|k\rangle_a\,|k\rangle_b = 0, \tag{5.51}$$

The coefficients may be calculated by requiring that equation (5.51) is true for each term,

$$|\zeta(t)\rangle = C_0 \sum_{k=0}^{\infty}\left[-\frac{\tilde{O}(-t)}{O(-t)}\right]^k |k\rangle_a\,|k\rangle_b\,, \tag{5.52}$$

where C_0 is a normalisation constant.

Equation (5.52) defines the decomposition on Fock states of the wave functions of $|\pm1\rangle$ after time evolution. We may also interpret this as the probability distribution for finding k atoms after time evolution

$$P(k) = |C_0|^{-2}\left|-\frac{\tilde{O}(-t)}{O(-t)}\right|^{2k}. \tag{5.53}$$

This is illustrated in figure 5.5, where the probability function is plotted for three different times. For $t = 0$, the function reduces to a delta function at $k = 0$, but as time progresses, the distribution flattens out towards larger k. At large t, the probability is distributed over a large region in k, which reflects the random nature of the process.

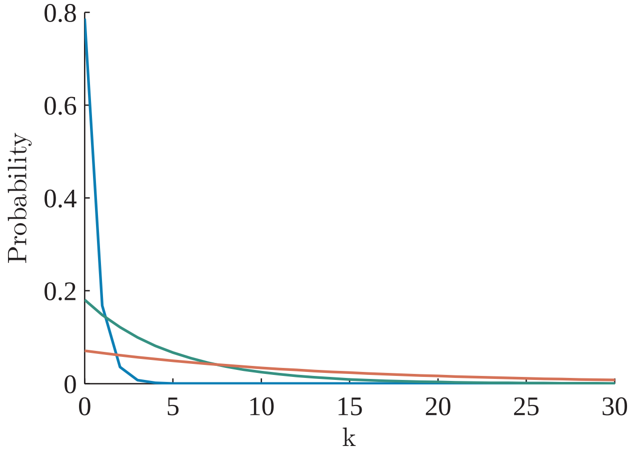

FIGURE 5.5: Probability function for finding k atoms after time evolution, $\mathrm{Im}\, E_{n,l}\, t/\hbar = 0.5$ (blue), 1.5 (green) and 2 (red).

This may also be interpreted in terms of the vacuum fluctuations. As a parametric amplification process, the starting time is determined by the seed, and since the seed is fluctuations of vacuum, the onset of amplification is random.

5.2 Experimental sequence

To experimentally realise the situation sketched in the previous section, we start by making a BEC in the $|2, 2\rangle$ state in the QUIC trap. There is typically around 2×10^5 atoms in the condensate and a negligible amount of atoms in the thermal fraction. The atoms are transferred to the vertical optical lattice by simultaneously ramping up the lattice potential and ramping down the QUIC potential over 110 ms. The transfer is not perfectly adiabatic with respect to the trapping frequency along z, but any motion induced along z can be cancelled by adjusting the ratio of currents in the QP and Ioffe coils.

The optical lattice potential follows an s-curve [67], whereas the QUIC potential follows a linear that has been smoothened with exponential start and end (figure 5.6 (a)).

The optical lattice is ramped to $s = 18$, which is in the isolating regime. The atoms are then distributed between the different lattice sites, where they make up individual condensates. To calculate the atom number in a given site, the distribution of atoms is assumed to be static at $s = 10$, and the atom number in each

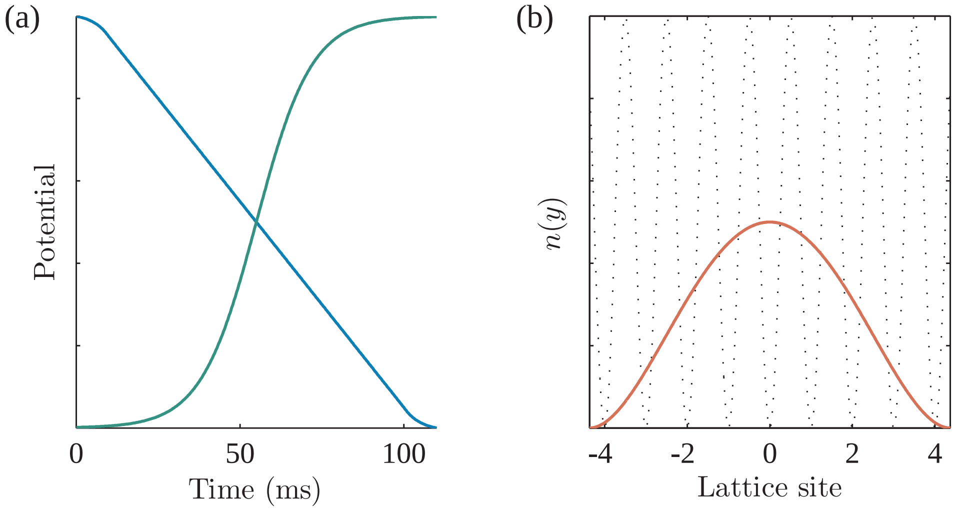

FIGURE 5.6: Lattice loading. *(a)* Ramp of QUIC potential (blue) and lattice potential (green). *(b)* Spatial distribution of atoms along the lattice. The one-dimensional density (red, solid) and the lattice potential (black, dotted) are sketched.

site is then simply the integral of the one-dimensional density over the lattice site. In the Thomas-Fermi approximation, this is

$$N_i = \frac{\pi \mu x_0 z_0}{2g} \int_{y_i-\lambda/4}^{y_i+\lambda/4} \left[1-\left(\frac{y}{y_0}\right)^2\right]^2 \mathrm{d}y\,, \tag{5.54}$$

where y_i is the centre of the i'th lattice site, g is the interaction strength, μ is the chemical potential in the magnetic trap at $s=10$, and $x_0, y_0.z_0$ are the Thomas-Fermi radii at $s=10$. Evaluation of equation (5.54) shows that only ~ 10 lattice sites are occupied due to the strong radial confinement in the QUIC trap.

During the transfer to the optical lattice, a significant heating is observed. A thermal fraction of $1.2(2)\times 10^5$ at a temperature of $\sim 120\,\mathrm{nK}$ appears, leaving on average $4.2(7)\times 10^4$ in the condensed phase.

After ramping down the QUIC potential, the only magnetic field left is a bias field along z of magnitude $B_z = 285\,\mathrm{mG}$. Choosing this direction as quantisation axis is advantageous for the subsequent microwave transitions, since the microwave antenna radiates primarily σ-polarisation along this direction.

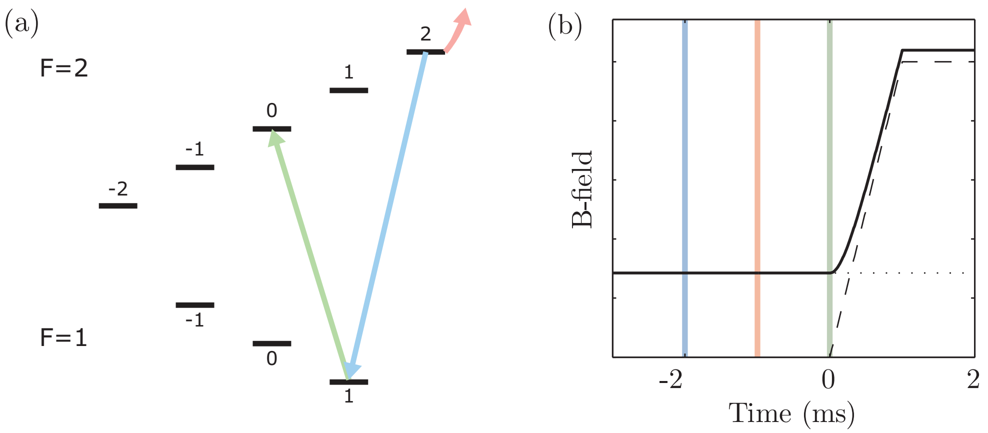

FIGURE 5.7: Microwave preparation. *(a)* Transition pulses, $|2, 2\rangle \rightarrow |1, 1\rangle$ (blue), $|1, 1\rangle \rightarrow |2, 0\rangle$ (green) and optical transition $|S_{1/2}, F = 2\rangle \rightarrow |P_{3/2}, F = 3\rangle$ (red). *(b)* Timing of pulses and magnetic fields, B_z (black, dotted), B_y (black, dashed) and total field (black, solid). The end of the second microwave pulse marks the start of spinor dynamics ($t = 0$) and coincides with the start of the B_y ramp.

The preparation of the $|2, 0\rangle$ state occurs 20 ms after turning off the QUIC trap. The state is reached by two microwave pulses as shown in figure 5.7, and the two π-pulses are 12 µs and 20 µs long respectively. Between the two pulses, the imaging laser is pulsed on for 60 µs to remove any atoms that might be left in the $|2, 2\rangle$ state. These atoms might have a seeding effect on the amplification process, so they should be avoided.

After the 2nd microwave pulse, a magnetic field is applied along y. The field is ramped to a final value over 1 ms, and the y axis is chosen because the y-shim coils have low inductance, so there is no significant induced current when ramping the current quickly. The start of the B_y ramp marks the start of the *spinor evolution time*, which is varied between 2 and 20 ms. In this time interval, the $|0\rangle$ atoms collide and produce atoms in $|\pm 1\rangle$.

Just before releasing the atoms from the trap, a third microwave pulse is applied on the clock transition $|2, 0\rangle \rightarrow |1, 0\rangle$ to reduce the density of the remaining $|0\rangle$ atoms. This is not a π-pulse, but closer to $\pi/10$, and if the exact phase of the pulse is known through calibration, one can calculate the original amount of atoms [88].

After the third microwave pulse, the cloud is released from the lattice by switching off the AOM controlling the lattice. This abrupt way of turning off the light causes a lattice projection as described in section 2.5. During time-of-flight, a magnetic field gradient is applied along the z-axis for 5 ms using the Ioffe coil. The gradient acts as a differential force on the individual spin components and makes them separate in time-of-flight (Stern-Gerlach separation).

The different spin clouds are imaged after 20 ms along the lattice direction using absorption imaging. The light is linearly polarised to be compatible with the lattice optics, and the imaging method is that described in section 3.5. The time between the raw and reference images is only 800 µs to avoid fringes in the imaging beam to shift, and the Faraday laser is tuned to resonance and used to actively remove the atoms before the reference image.

5.3 Results: Ring structure and visibility

Following the scheme described in the previous section, the populations in $|\pm1\rangle$ show the expected exponential increase with time. To quantify the number of atoms in $|\pm1\rangle$ we use the relative population

$$p_{\pm1} = \frac{N_{+1} + N_{-1}}{N_{+1} + N_0 + N_{-1}} \tag{5.55}$$

where N_i is the population of the i'th spin state.

The fraction of atoms in $|\pm1\rangle$ versus time at $q = -67\,\mathrm{Hz}$ is shown in figure 5.8, and the data is fitted with an exponential function. The exponential model works well for short times, but begins to deviate at $t \approx 10\,\mathrm{ms}$, which is interpreted as the break-down of the linear regime. At this point, the depletion of the $|0\rangle$ condensate cannot be neglected anymore.

The exponential fit yields a time scale of $\tau = 3.0(2)\,\mathrm{ms}$, which is to be compared to the theoretical value found in equation (5.45), $\tau = h/4\pi\,\mathrm{Im}\,E_{n,l}$. Comparing to figure 5.4 b, the instability rate is seen to be $\sim 35\,\mathrm{Hz}$ leading to a time scale of $\tau = 2.7\,\mathrm{ms}$ in good agreement with our data.

In order to investigate the effect of q in the spinor dynamics, the spinor evolution time was fixed at 8 ms in order to stay in the linear regime. The vertical magnetic field B_y was varied from 216 mG to $\sim$ 3 G leading to a range of $|q|$ from 9.2 Hz to $\sim$ 650 Hz. The resulting graph in figure 5.9, shows a rapid growth in the population in $|\pm1\rangle$ around $|q| \simeq 25\,\mathrm{Hz}$, peaking at $|q| \simeq 100\,\mathrm{Hz}$. After this point, the population slowly decreases.

The effect of varying q is also seen in the cloud structure, as shown in figure 5.10. At -48 Hz, the clouds are clearly peaked, but the structure gradually changes to ring structure around 200 Hz. Furthermore, there is a striking structure along the circumference, which is similar to a modulation of the density at even larger $|q|$.

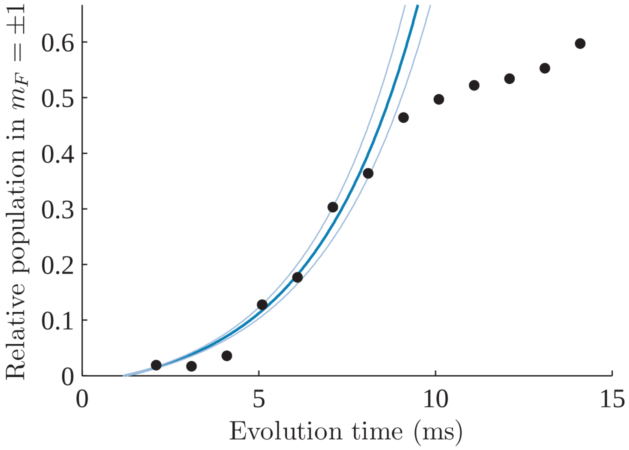

FIGURE 5.8: Time evolution of spinor dynamics at $B_y = 0.902$ G, $q = -67$ Hz. An exponential fit is shown (dark blue) along with error bars on the fit (light blue). The collapse of the linear regime is clear around 10 ms. The fitted value of τ was 3.0(2) ms.

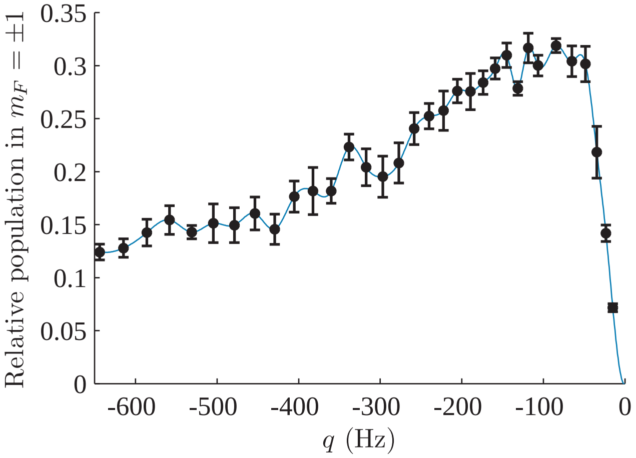

FIGURE 5.9: Mean population in $|\pm 1\rangle$ after 8 ms evolution time. Data (black dots) is shown with standard deviation as error bars and an interpolated line a guide to the eye (blue).

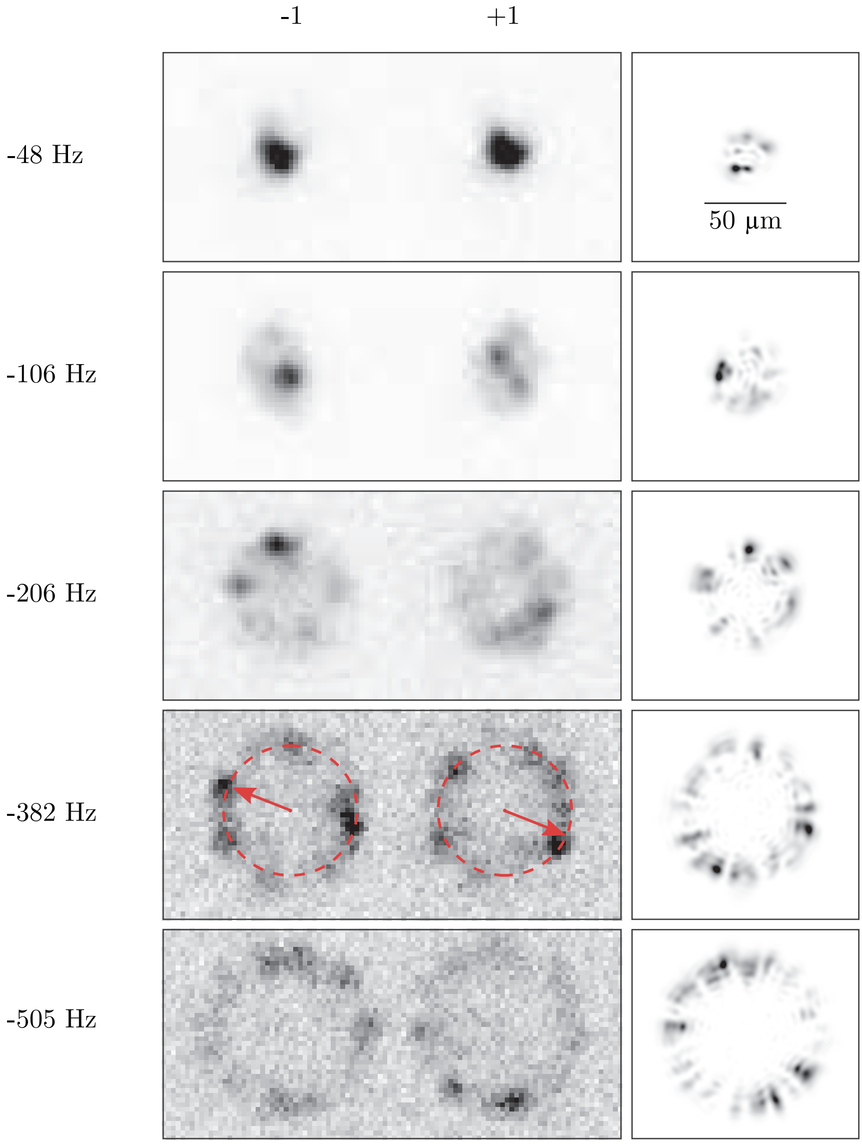

FIGURE 5.10: Cloud structure after 8 ms evolution time at different values of q. *(left)* Experimental images of only the $|\pm 1\rangle$ atoms. At $q = -382$ Hz, arrows have been added to show the anti-correlation of the ring structure. *(right)* Simulations, these will be discussed in section 5.4.

The appearance of ring structures is typically associated with angular momentum, since the coherent nature of a BEC requires the pivot point to have zero density in the centre. A ring (or cylinder) is then the manifestation of a circulation around the centre, and this structure is usually kept after time-of-flight as a result of *self-similar expansion*. This is, however, not necessarily the case in two dimensions, because a ring can result from ballistic expansion. If a cloud is given a momentum of well-defined magnitude but random direction, it will turn into a ring in time-of-flight, irrespectively of the spatial distribution in the trap. In three dimensions, the corresponding system will produce a spherical shell after time-of-flight.

To test this interpretation, it is interesting to look at the transition from peak structures to rings which may be quantified by the *visibility* of the ring. In this setting, the visibility can be defined as

$$\mathcal{V} = \frac{n(R) - n(0)}{n(R)}, \tag{5.56}$$

where $n(R)$ is the density on the circumference of the ring and $n(0)$ is the density at the centre of the ring. For a peaked structure, the radius of the ring will be ~ 0 leading to a visibility of zero, whereas the visibility for a ring with no density in the centre will be one.

The actual evaluation of the visibility is more complicated, since both the centre and the radius of the ring need be known. To that end, the data has been fitted with a two-dimensional ring, and the cloud is then transformed by interpolation into a cylindrical frame. Here, it is simple to find the average density as a function of radius $n(r)$. However, the centre of the ring needs careful evaluation, since that value in principle is determined by a single pixel. Therefore, the centre value was extrapolated by a linear fit for the first few pixels.

In figure 5.11, the visibility is shown for a range of q values. For $|q|$ lower than $\sim 150\,\text{Hz}$, the visibility is constant at zero, indicating a peak structure. Beyond this point, $\mathcal{V}$ quickly rises and settles at a value of ~ 0.75 at $q \approx -200\,\text{Hz}$. This suggests that the dominant mode is the first Bessel mode $n = 1$, $l = 0$ up to $q \sim -150\,\text{Hz}$, since this is the only mode to show a peak-like structure.

However, a comparison with the mode spectrum in figure 5.12 (a) shows that the (1, 0) mode vanishes already at $q \approx -90\,\text{Hz}$. This suggests that the ring structures are not the eigenstates of the effective potential, but probably a superposition that leads to a ring structure in time-of-flight.

As an indication of such superposition phenomena, the multi-mode character of the system can be evaluated as $\delta E/E$, where δE is the energy separating different modes, and E is the mean energy of the modes. If $\delta E/E \ll 1$, the modes

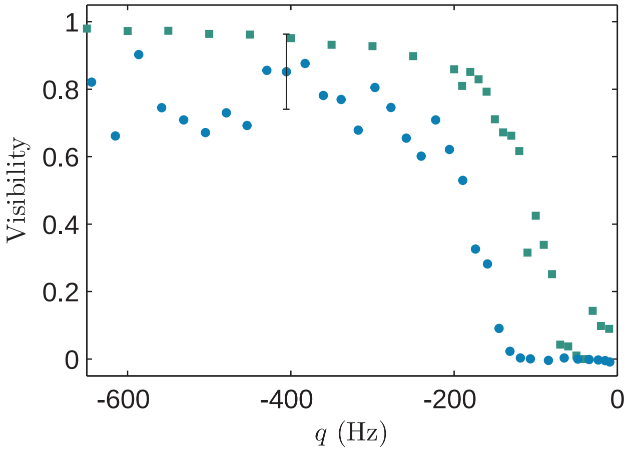

FIGURE 5.11: Visibility of the ring structure after 8 ms evolution time. Data is shown in blue (dots) and simulations are shown in green (squares). A representative error bar is shown for the data.

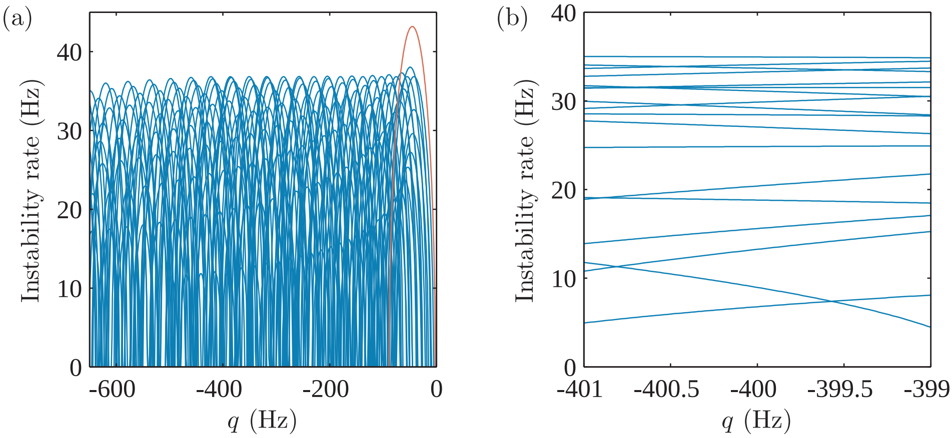

FIGURE 5.12: Instability spectrum. *(a)* Full spectrum of the instability rates. Note the prominence of the $n = 1$, $l = 0$ mode (red). *(b)* Unstable modes at $q = -400\,\text{Hz}$. In order of decreasing instability, the modes are $(n, l) = (7, 7)$, $(10, 0)$, $(8, 5)$, $(9, 2)$, $(6, 9)$, $(5, 12)$, $(9, 3)$, $(8, 4)$, $(10, 1)$, $(4, 15)$, $(6, 10)$, $(3, 18)$, $(7, 6)$, $(2, 22)$, $(4, 14)$, $(5, 11)$, $(5, 13)$, $(1, 26)$.

are effectively degenerate on the time scale of $h/4\pi E$, and they will grow with almost equal rate, placing the system in the multi-mode regime. Since the quantised nature of the modes is vanishing in this limit, it is also called the *free-space regime*.

Figure 5.12 (b) shows all unstable modes at $q = -400\,\mathrm{Hz}$, and here $E \approx 25\,\mathrm{Hz}$ and $\delta E \approx 1.5\,\mathrm{Hz}$, showing that the system is highly multi-mode. In order to see a difference in the growth of the various modes, one needs to look on a time scale of $h/4\pi\delta E \sim 50\,\mathrm{ms}$ which is far beyond the linear regime and therefore not of relevance to the current experiments.

5.4 Simulations: Ring size and correlations

Given that the system is multi-mode, and the fact that the individual modes grow identically in the linear regime, we may treat each mode separately. This, together with the model presented in section 5.1, forms the basis of our simulations of the spinor dynamics.

Starting from the transfer from the QUIC trap to the lattice, the number of atoms in each lattice site can be calculated by equation (5.54). Taking each site as an independent condensate, we apply the Thomas-Fermi approximation to each site, and calculate the chemical potential from equation (2.20).

The system can then be taken to 2D using the definitions (5.6), which makes it easy to calculate the instability spectrum for each lattice site. The Bessel mode energy spectrum is shown in figure 5.13 (a) for different lattice sites, and it is clear that the central sites have almost the same spectrum, and the effect of the lower atom number (and hence lower chemical potential) is to shift the states up in energy.

In order to find the relevant modes that contribute to the $|\pm1\rangle$ states, one just needs to find the modes with a finite instability rate, create a superposition and repeat this for each site to construct the total cloud. To this end, the expansion of the state in the Fock basis, equation (5.53), is used to give the population in each mode. The expansion coefficients may be seen as a probability distribution, and by summing the terms up to a given atom number k, one can construct a cumulative probability function (figure 5.13 (b)).

For each mode it is thus possible to simulate the experiment by drawing a uniform random number between zero and one, and from the cumulative probability function, this is translated into an atom number for that particular mode. At a given q, this is done for each unstable mode in a lattice site, and the modes are given a random phase and added. Repeating this procedure for each lattice site,

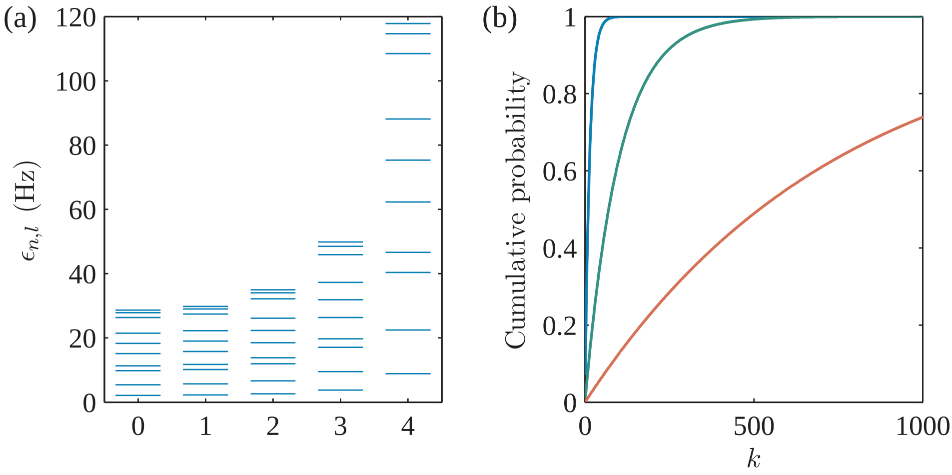

FIGURE 5.13: *(a)* The effect of additional lattice site. The lowest 10 Bessel modes in different lattice sites. Zero is the central site. *(b)* Cumulative probability function for different evolution times, $\operatorname{Im} E_{n,l}\, t/\hbar = 2$ (blue), 3 (green) and 4 (red).

the spatial profiles from all sites are added coherently[2] to obtain the atomic distribution when the lattice is turned off.

To find the cloud shape after time-of-flight, the total cloud is taken to momentum space by a 2D Fourier transform. It is straightforward to evolve the cloud under the free-space Hamiltonian in the momentum basis as

$$\psi(\boldsymbol{p}, t) = \psi(\boldsymbol{p}, 0) \exp\left(\frac{-i\boldsymbol{p}^2}{2m\hbar} t\right) \tag{5.57}$$

and afterwards, the cloud is transformed back to position space by the inverse Fourier transform.

The final step is to take the modulus squared of the distribution, and in order to simulate the effect of the imaging system, the cloud structure is filtered with a Gaussian filter with the width of the point spread function (section 3.5 on page 68). This leads to the pictures shown along with the experimental images in figure 5.10 on page 112.

The simulations show the same qualitative features as the experiments. At low $|q|$, the cloud is strongly peaked at the centre, whereas it shows a clear ring struc-

---

[2] Although the lattice sites are separated in space, the expansion after release from the trap is much larger than the original size of the cloud, so the sites may be taken as overlapping.

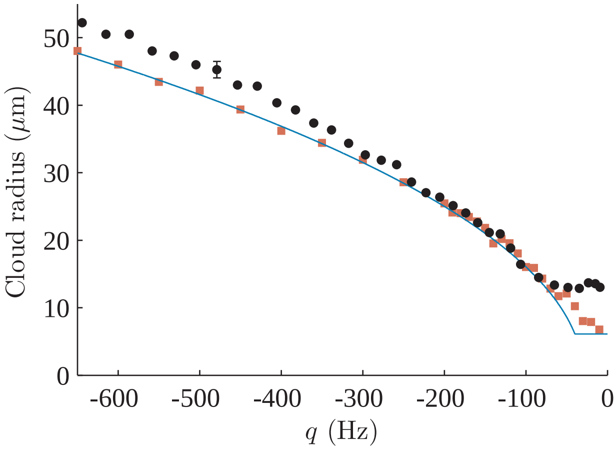

FIGURE 5.14: Cloud radius at different values of q. Data is shown in black (bullets), simulations in red (squares), ballistic model in blue (solid). Representative error bar is shown for data.

ture at large $|q|$. Furthermore, the simulations also feature peaks along the circumference of the ring, although the angular structure is finer than what is observed experimentally.

A more quantitative comparison is obtained by analysing the visibility in the same fashion as for the experimental pictures (figure 5.11). There are two differences between experiments and simulations here: Firstly, the onset of rings occurs earlier, around 80 Hz (as opposed to the 150 Hz for experiments), and secondly the visibility goes to unity for large $|q|$.

The appearance of rings in the simulated clouds coincides well with the vanishing instability of the lowest mode (figure 5.12), and this indicates that the primary contributor to the peak is the lowest Bessel state. There seems to be some smearing or coarsening angularly, and if a similar phenomenon is present in the radial direction, this would make it more difficult to resolve the ring structure and hence shift the onset of rings to a larger value of $|q|$.

Another comparison between experiments and simulations is obtained by investigating the size of the cloud which is given by the expectation value of the position from the atomic distribution. To this end, the image is transformed to a cylindrical basis, the angular coordinate is integrated out, and finally, the first moment of the distribution is calculated. For the simulated images, the second moment of the spatial distribution was calculated, and the results are shown in figure 5.14.

The simulations show good agreement with data, especially in the region $q =$

-100 to $q = -200\,\mathrm{Hz}$. The deviation at both high and low $|q|$ indicates that the box model is not valid in this region. For high $|q|$, the hard-wall approximation is inaccurate, since the finite slope of the potential boundaries produces larger clouds in trap. For low $|q|$, the simulations underestimate the cloud size which we interpret as caused by the repulsion from the $|0\rangle$ atoms, $\tilde{U}_1 n_0 \sim 50\,\mathrm{Hz}$.

Interestingly, the data also shows an increase in cloud size just below the point $|q| = 100\,\mathrm{Hz}$, which coincides with the vanishing instability of the lowest Bessel mode. This supports the hypothesis that the this mode is dominant in the formation of peaked clouds, and that the "ring regime" actually sets in when this mode vanishes.

One interpretation is that there occurs a spontaneous symmetry breaking during the spin-changing collisions in each site. This is to be understood as a bosonic stimulation of the spin-changing collisions, such that a region of space where a large population in $|\pm 1\rangle$ is present will have an increased probability for undergoing more spin-changing collisions. Such spatial inhomogeneity would arise due to random fluctuations and would lead to the formation of a single (or few) wave packet(s) in each site. Such an effect would explain that the structure observed experimentally is coarser than what is predicted by simulations.

In the free-space regime, the effect of increasing $|q|$ amounts to increasing the momentum of each wave packet by $p_{\mathrm{rms}} = \sqrt{2M|q|}$. If one assumes a purely ballistic expansion, the radius after time-of-flight is

$$\langle \rho \rangle = \sqrt{\rho_0^2 + \left(\frac{p_{\mathrm{rms}}\, t}{M} \right)^2}, \tag{5.58}$$

where ρ_0 is the in-trap radius, and t is the time-of-flight. This expression does not take the effect of the repulsion from $|0\rangle$ into account, so in order to improve the model, the mean value of the repulsion is subtracted from q

$$\langle \rho \rangle = \begin{cases} \rho_0 & q \le \langle \tilde{U}_1 n_0 \rangle \\ \sqrt{\rho_0^2 + \left(\frac{\tilde{p}\, t}{M} \right)^2} & q > \langle \tilde{U}_1 n_0 \rangle, \end{cases} \tag{5.59}$$

where $\tilde{p} = \sqrt{2M|q - \langle \tilde{U}_1 n_0 \rangle|}$. Equation (5.59) is plotted in figure 5.14 in blue and shows good agreement with data except for extreme values of q. For low $|q|$, the ballistic model strongly underestimates the size, but this is because it neglects any mean field expansion and is "frozen" at the in-trap Thomas-Fermi radius.

If there really is only a single wave packet in each site, a strong spatial anticorrelation between the two spin components $|\pm 1\rangle$ is expected. This is clearly seen in the spin-changing term in the Hamiltonian (5.19), where the field operators of

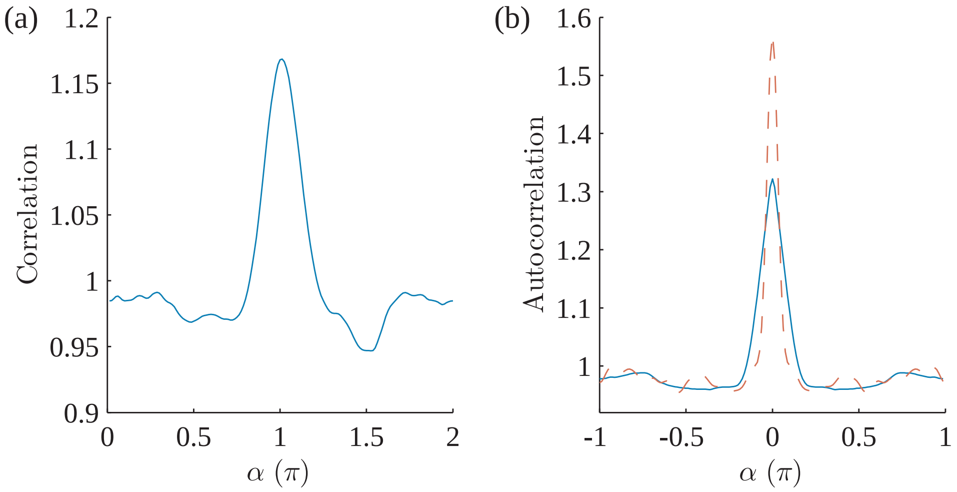

FIGURE 5.15: Angular correlation of cloud. *(a)* Correlation of $|\pm1\rangle$. *(b)* Autocorrelation of data (blue, solid) and of simulations (dashed, red).

$|\pm1\rangle$ only appear in pairs of $l = \pm1$ in order to preserve angular momentum. The same is true for linear momentum, so if a wave packet of momentum $\boldsymbol{p}$ is observed in $|+1\rangle$, a similar wave packet of momentum $-\boldsymbol{p}$ must be present in $|-1\rangle$.

This motivates the introduction of the correlation function

$$c(\alpha) = \frac{\langle \tilde{n}_{-1}(\theta)\,\tilde{n}_{+1}(\theta-\alpha)\rangle}{\langle \tilde{n}_{-1}\rangle\langle \tilde{n}_{+1}\rangle}, \tag{5.60}$$

where $\tilde{n}_i(\theta)$ is integrated radially, and brackets denote the angular mean. The correlation is shown in figure 5.15 (a) for $q = -297\,\text{Hz}$ where the function is averaged over 54 realisations. Clearly, the dominant correlation is at $\alpha = \pi$ corresponding to the expected anti-correlation.

Comparison with theory is difficult in this case, since only one of the spin components is simulated. However, the autocorrelation gives an indication of whether there is agreement in radial structure, and this is shown in figure 5.15 (b) for experimental data and simulations. Here, it is clear that simulations show stronger and narrower correlation than experiments in agreement with the observed difference in angular structure. The fact that the experiments feature wider spikes indicates that not all of the allowed modes contribute to the structure. Apparently, some of the high-l modes are not present.

Nonetheless, a large number of modes are included and interfere destructively to create the flat structure away from $\alpha = 0$. This is consistent with the wave packet interpretation, and indicates that a spontaneous symmetry breaking really is present.

To summarise, a theoretical and experimental analysis of a spinor gas in a two-dimensional setting was presented. The theoretical model predicts an exponential amplification of the number of atoms in the $|\pm1\rangle$ states through the non-linear interaction in the $|0\rangle$ state – even when starting from a vacuum state.

A large number of spatial modes in the trap are expected and due to the near degeneracy of many of these modes, the system is in a multi-mode regime. A numerical simulation of the system employing a random amplification of each mode shows that the clouds are expected to increase in size after time-of-flight as the magnetic field is increased. The structure of the clouds changes from a central peak to a ring-like structure. Although the onset of rings does not match in simulations and experiments, the increase in radius is well captured by the simulations. Furthermore, owing to the almost free-space nature of the trap modes, a simple ballistic model describes the expansion of the rings well.

An analysis of the angular structure also shows anti-correlation between the two clouds in the $|+1\rangle$ and $|-1\rangle$ state as expected from theory. Furthermore, the angular autocorrelation reveals that only a subset of the allowed modes contribute to the radial structure, and this indicates that the atoms bunch together to create coarser structure.

CHAPTER 6

EVAPORATION AND SPIN DYNAMICS IN A CROSSED OPTICAL DIPOLE TRAP

In this chapter, the first results of using the crossed dipole trap for spinor experiments will be presented. In the first section, I shall discuss the creation of a BEC in the crossed dipole trap, and in the following section, I shall present applications of the trap. These preliminary investigations display the prospects for using the crossed dipole trap in spinor physics experiments.

6.1 Evaporation in dipole trap

Creation of condensates in an optical dipole trap is a standard method. The typical approach is to load a laser cooled cloud into a magnetic trap, and evaporatively cool it before transferring it to an optical dipole trap. Here, the light intensity is slowly lowered to cool it to degeneracy. This approach requires careful overlap of the magnetic trap and the dipole trap to ensure good transfer efficiency. In the dipole trap, gravity lowers the bottom edge of the potential as showed in figure 2.10, so evaporation will primarily occur along the vertical axis. An alternative approach is known as the hybrid trap, where the gradient is provided by a magnetic field, but since a uniform magnetic field is requires for the spinor experiments, we have not chosen this method.

First, the crossed dipole trap has to be aligned with the QUIC trap. We use the "kick" method as described in section 3.3 for a rough alignment of each of the two beams. Afterwards, the position of the cloud is measured, when it was held in the trap, and the beams were adjusted to overlap it with the position in the QUIC trap. This was only possible, because a Semrock notch filter (780 nm) with an OD 5–6 protected each of the cameras.

For the evaporation, a cloud was cooled by standard RF evaporative cooling to

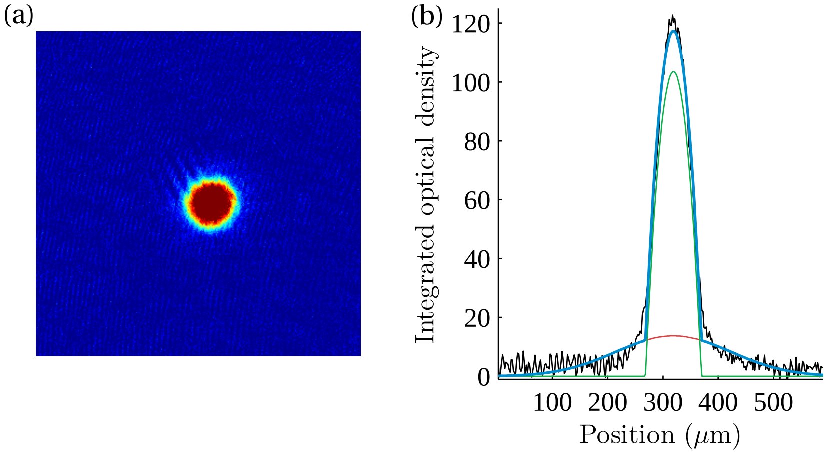

FIGURE 6.1: Production of a BEC in a crossed dipole trap. *(a)* Absorption image of the cloud taken along the x-axis after 15 ms time-of-flight. *(b)* The profile integrated along the vertical axis. Data is shown in black and the bimodal fit in blue. The constituting parts of the bimodal fit are plotted; the Thomas-Fermi profile in green, and the Gaussian part in red.

a frequency roughly 100 kHz above the trap bottom, well before any sign of condensation appears. The cloud was then transferred to the crossed dipole trap by ramping the QUIC current down and the dipole light intensity up over 100 ms, similar to the procedure in section 5.2.

The two dipole beams deliver $P_x \approx P_z \approx 130\,\mathrm{mW}$ when the cloud is loaded. This is significantly less than the power available, but the atomic density appears to be too large when loading the cloud at full power. For larger beam powers, there were significant losses over ~200 ms, hence the given power was chosen.

After loading the dipole trap, the light power was decreased in two steps: A short and deep cut to 33% of the initial power over 500 ms, and a slow cut to 20% of the initial power over 1.75 s. This yielded a BEC of $\sim 5 \times 10^4$ atoms in the BEC and a temperature of 85 nK. An absorption image of the cloud taken along the x-axis is shown in figure 6.1 (a) and the integrated signal is plotted in figure 6.1 (b) along with a bimodal fit to the profile.

Following the production of a BEC in the crossed dipole trap, the trapping frequencies were measured. For this purpose, the power of the two dipole beams was set slightly above the BEC value (22% of the initial power), and the z-beam was

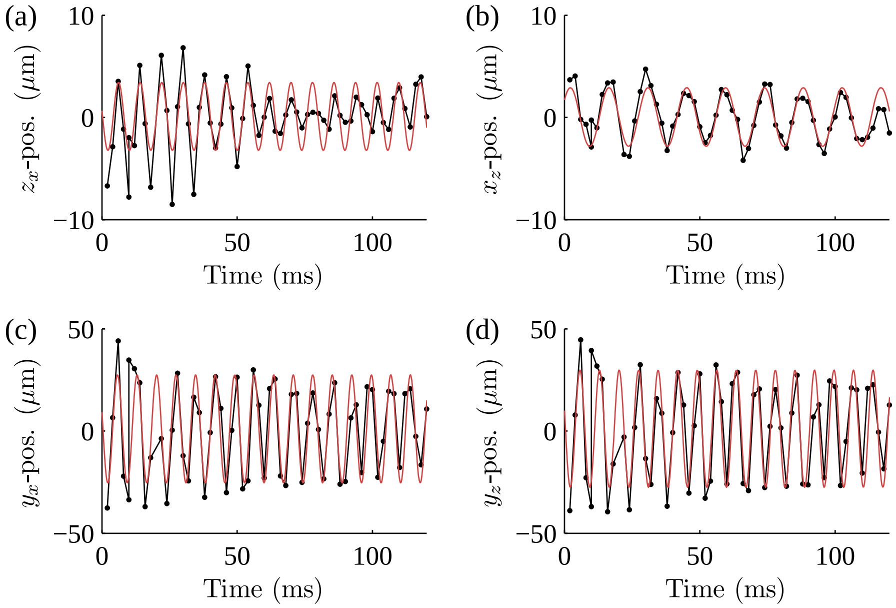

FIGURE 6.2: Trapping frequencies in the crossed dipole trap. The subscript on the coordinate indicates which camera was used for the data. Oscillations were initiated by reducing the power of the z-dipole beam, which leads to stronger oscillations along the vertical axis compared to the horizontal axes. *(a)* Oscillations along z, imaged on the x-camera. Fitted oscillation frequency: $\omega_z = 2\pi \times 125.6(5)\,\mathrm{Hz}$. *(b)* Oscillations along x, imaged on the z-camera. Fitted oscillation frequency: $\omega_x = 2\pi \times 69.7(3)\,\mathrm{Hz}$. *(c)* Oscillations along y, imaged on the x-camera. Fitted oscillation frequency: $\omega_y = 2\pi \times 138.6(4)\,\mathrm{Hz}$. *(c)* Oscillations along y, imaged on the z-camera. Fitted oscillation frequency: $\omega_y = 2\pi \times 138.6(4)\,\mathrm{Hz}$.

turned off[1] for 1 ms to allow gravity to displace the cloud slightly. The response of the cloud was measured for 110 ms, which yielded a strong oscillation along the vertical direction (y), but also a significant oscillation in the horizontal plane. For each point in time, the cloud was imaged simultaneously along z and x, and the resulting oscillation is shown in figure 6.2.

To obtain these curves, the images were turned by 8° for the x-images and 5° for the z-images to resolve the independent oscillations. This is due to small

---

[1] In practice, the power was set to a small but finite value to avoid any spikes from the regulating circuit: When the power is set to zero, the circuit goes out of regulation, and when it starts regulating again, the response overshoots.

imperfections in the dipole trap beam: alignment, astigmatism, ellipticity of the beam profile, etc. These imperfections turn the primary axes of the trap, but the effect can be minimised by optimising the beam path of the dipole light. Still, even a change in the ratio of power in the dipole beams will cause the primary axis to turn [89].

In the natural frame of oscillation, the trapping frequencies are $\omega_x = 2\pi \times 69.7\,\mathrm{Hz}$, $\omega_y = 2\pi \times 138.6\,\mathrm{Hz}$ and $\omega_z = 2\pi \times 125.6\,\mathrm{Hz}$. The vertical trapping frequency is the same on the two cameras, but the z trapping frequency is considerably larger than the x trapping frequency. Since the same power is used in the two beams, the beam waists of the two dipole beams cannot be equal. Using a quadratic fit of the potential from the two beams, a simple trial and error approach shows that beam waists $w_x = 54\,\mu\mathrm{m}$ and $w_z = 40\,\mu\mathrm{m}$ yield trapping frequencies that are very similar to the ones observed experimentally. So most likely, the spot size along x is larger than expected, and a future optimisation of the dipole setup will determine whether this is because the focus of the x-beam does not overlap with the z-beam, or because the beam waist simply is larger than what was originally measured.

Furthermore, before using the dipole trap for spinor experiments, the beam waist of both beams at the position of the atoms should be increased to exploit the full intensity of the dipole beams. This can be easily done by adjusting the position of the 500 mm lens or reducing the beam expansion in the telescopes.

6.2 Applications

After the production of our first BEC in the crossed dipole trap, a number of experiments was performed to test the prospects of using this setup in spinor experiments. The results in this section are preliminary and should only be regarded as feasibility studies.

In the first set of experiments, a BEC in the crossed dipole trap was transferred to the $|2, 0\rangle$ state and allowed to evolve in the same fashion as the experiments presented in chapter 5. In this way, the experiment recreates the general experimental setup from the Hannover group [34–36].

These experiments were carried out as follows: A condensate was created in the crossed dipole trap by ramping the power to 22% of the initial power at a background field of 0.53 G along the z direction. After the BEC was formed, two consecutive pulses transferred the condensate to the $|2, 0\rangle$ state; first a $11\,\mu\mathrm{s}$ pulse at 6835.800 MHz and afterwards a pulse of $20\,\mu\mathrm{s}$ duration at 6835.055 MHz. Directly after the second microwave pulse, the magnetic field along the y-direction was

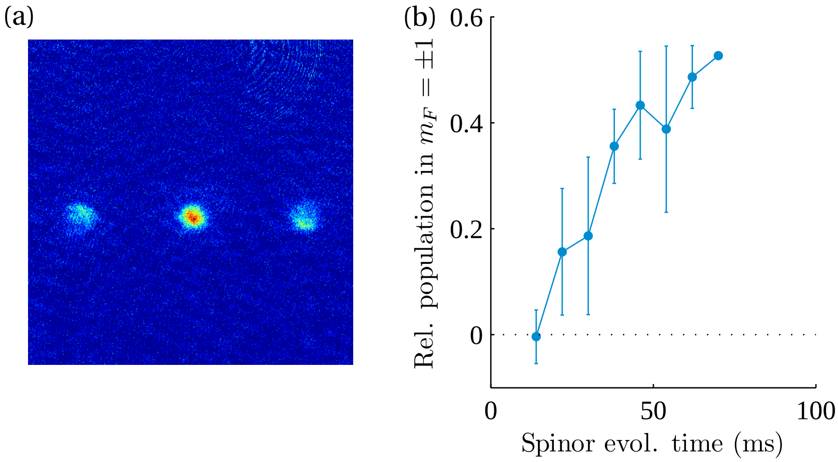

FIGURE 6.3: Spin dynamics in a crossed dipole trap. *(a)* Absorption image of $|2, 0\rangle$ cloud following 64 ms hold at $q = -26\,\text{Hz}$. *(b)* Time evolution of the relative population in $m_F = \pm 1$ at $q = -26\,\text{Hz}$. The data was averaged in bins of width 8 ms.

ramped up over 1 ms to change the quadratic Zeeman energy. After a variable hold time in the dipole trap, the cloud was released and the spin states separated by a Stern-Gerlach gradient along z. The cloud was imaged by absorption imaging along the x-axis after 15 ms time-of-flight.

For hold times around 20 ms, a population in $|2, \pm 1\rangle$ appears, indicating that spin-changing collisions occur in the dipole trap. A typical image is shown in figure 6.3 (a), taken at $q = -26\,\text{Hz}$ after 64 ms hold time in the dipole trap. The structure of the $|2, \pm 1\rangle$ clouds indicates that the atoms are in an $n = 1$, $l = \pm 1$ mode, since the superposition of $l = \pm 1$ produces exactly such a cloud with a dark and bright pattern [36].

The time dependence of the relative population in $m_F = \pm 1$ as defined in equation (5.55) is shown in figure 6.3 (b). The data was taken in steps of 2 ms, but has subsequently been binned in groups of 8 ms width to gain better statistics. The graph clearly shows that the population in $|2, \pm 1\rangle$ grows on a much longer time scale compared to the lattice. This is due to the lower density in the dipole trap.

Figure 6.4 shows the result of experiments where the magnetic field was varied, while keeping a hold time of 50 ms. The relative population is shown along with images of the cloud profiles at each point illustrating some of the observed modes. The investigation is by no means complete, but it appears that the majority of the

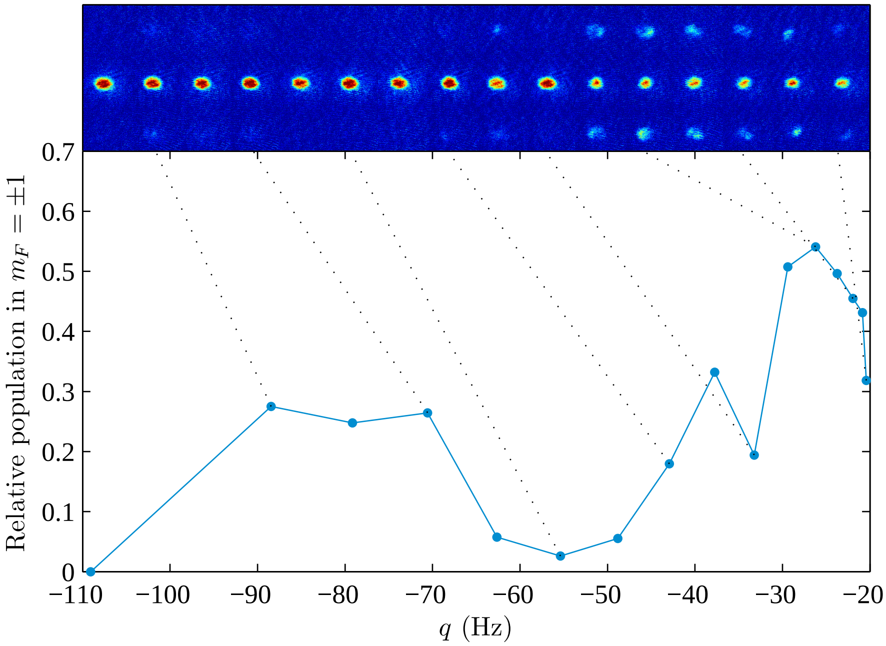

FIGURE 6.4: Different modes after spin dynamics in an optical dipole trap at different magnetic fields. The relative population of the $|2, \pm 1\rangle$ states is plotted along with the mode profile of each point.

spin dynamics happens from $q = -20$ to -40 Hz.

A further series of experiments focused on loading a cloud from the crossed dipole trap into an optical lattice. In this case, the polarisation of the lattice is important, since there is only one polarisation axis available where the lattice will not interfere with the dipole trap. Furthermore, the lattice beam is also using an 80 MHz AOM, so detuning from both beams is not possible. In order to compensate, the lattice AOM frequency was increased to 90 MHz and coupling was optimised for this setting.

When loading the BEC into the lattice, the lattice potential was ramped to $s = 9$ over 100 ms. The dipole trap remained at a constant value until the lattice had assumed half its final value, and then the dipole potential was ramped linearly to zero coinciding with the end of the lattice ramp. The cloud was held for another 10 ms before being released from the lattice in a projection-like manner to test for superfluidity.

After release from the lattice, the cloud displayed projection peaks as shown

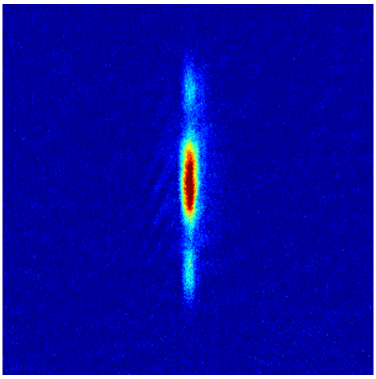

FIGURE 6.5: Loading the vertical optical lattice from the crossed dipole trap. The cloud was held for 10 ms in the optical lattice only, $s = 9$. Projection peaks indicate a coherent BEC.

in figure 6.5, indicating that a coherent BEC was transferred to the lattice. However, at lower lattice depths, faint or no projection peaks were visible, showing that the transfer is not yet ideal. Once the dipole trap is put into a final shape, lattice loading from the crossed dipole trap will be explored further.

A final set of experiments investigated the application of Faraday imaging in the dipole trap. Such a tool would be very powerful for measuring trapping frequencies, as only a single experimental run is enough to sample the entire oscillation. We have already made such an experiment in the QUIC trap, where the cloud was imaged 2000 times during a decompression of the trap [59].

However, the atomic density in the dipole trap is still too low to see any Faraday signal. This might be solved by optimising transfer to and evaporation in the dipole trap, since the interaction with more atoms would cause more rotation of the light. Of course, it is also possible to decrease the detuning of the Faraday laser, but this comes at the cost of destructiveness, so this path seems less fruitful. Another approach is just to increase the integrated atom number as seen from the camera by changing the aspect ratio of the dipole trap. This has been done to an extreme degree in the group of Morgan Mitchell, such that the cloud approaches one-dimensional behaviour [90].

CHAPTER 7

TOWARDS ATOM NUMBER STABILISATION USING FARADAY FEEDBACK

In this chapter, I shall discuss ongoing experiments into atom number stabilisation by feedback using Faraday imaging. The Faraday measurements have primarily been carried out by Miroslav Gajdacz, since he has performed the technical task of creating a combined imaging acquisition and real-time feedback loop on an FPGA. This project has been underway for some time, and a publication is expected within the next six months.

7.1 Non-destructive Faraday imaging

The use of non-destructive imaging allows for multiple imaging of the same atomic cloud. In the early experiments of Bose-Einstein condensation, dispersive imaging techniques were applied to gain *in situ* information about dense clouds [91]. However, the technique has also proved particularly useful for time-resolved imaging of single clouds [32].

Another interesting prospective application of non-destructive imaging is the possibility to apply feedback to an atomic ensemble. Feedback has previously been applied to trapped atoms in an optical lattice in order to cancel oscillations [92], but here the error signal was acquired by measuring the scattered light from the optical lattice.

Faraday measurements have previously been used to generate an error signal for feedback as a means of teleporting a light state onto an atomic state [93]. This was performed on room temperature samples held in vapour cells on the collective spin state of the ensemble. Later uses of feedback from Faraday signals include the controversial spin squeezing experiments performed in the Mabuchi group [94]. Here, the Faraday effect was exploited to gain information about the orientation of the spin of a system, but the observation of spin squeezing following the feedback was later retracted.

In our experiments, Faraday imaging is used to measure the spatial distribution of a cold atomic cloud, as discussed in section 3.4. In this chapter, our recent experiments towards stabilisation of the atom number of an atomic ensemble are discussed. Stabilisation of the atom number has great experimental prospects, as the smaller fluctuation in atom number improves shot-to-shot reproducibility, which can often be the dominant source of uncertainty in experimental data. Furthermore, the production of ultracold ensembles is the product of several stochastic processes, from laser cooling, evaporative cooling and density-dependent loss mechanisms. While these processes each lead to different uncertainties in the prepared atom number, Poissonian noise is typically taken as a benchmark leading to $\sqrt{N}$ fluctuations in the prepared atom number. Using feedback, it is possible to generate a ensemble with a precision surpassing the $\sqrt{N}$ noise.

In the present, we focus on preparing ultracold, thermal clouds. Typical parameters include an atom number of $N \sim 2 \times 10^6$ and a temperature of $T \sim 2\,\mu\mathrm{K}$. In future work, we shall extend the feedback to ensembles at the critical temperature in order to create condensates with high stability in atom number.

The working principle of the feedback scheme is to generate an error signal using Faraday imaging and then to apply a correction to the RF sweep during evaporative cooling. The system was originally designed for multi-step feedback, where the cloud is imaged repeatedly and feedback is applied as a response to each image, but so far only a single feedback step has been applied. This approach works very well, indicating that the primary problem in stabilising the atom number in a cold cloud the variation of atoms initially loaded into the trap.

Single-step feedback relies heavily on finding the correct feedback gain and is only useful in the so-called *unity-gain regime*. This amounts to matching the feedback to the “natural response” of the system, which allows the correction to be applied in a single step. Another regime is the *low-gain regime*, where the feedback deliberately undercompensates, but instead applies many repeated corrections to slowly reach the desired value. This regime is less likely to “overcompensate”, which could cause problems in a system like ours, where atoms can only be removed by the RF knife but not added, since the default evaporation sequence is optimised for maximum atom number.

The multi-step feedback is a good strategy if the quantity to be stabilised slowly drifts. In such a system – e.g. a diode laser that is heated from the environment – a continuous correction is required. On the other hand, if only an offset error needs to be corrected, a single-step feedback could be more efficient. The disadvantage of single-step feedback is that the gain needs to be known with high accuracy.

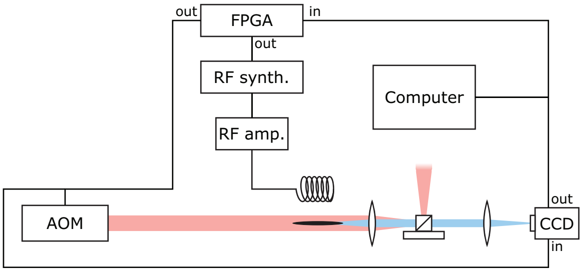

FIGURE 7.1: Experimental setup of feedback. Imaging is controlled from the FPGA that triggers the AOM. The image is transferred to the computer, but the FPGA reads the image in parallel, analyses it and generates a feedback signal to the RF synthesizer, which changes the evaporation ramp.

Feedback

Feedback to a cold atomic cloud requires fast imaging and data processing to work on the time scale of the atoms. To this end, a *field-programmable gate array* (FPGA) is employed to control imaging and RF radiation. The FPGA is a National Instruments PCIe-7852R running at a clock frequency of 40 MHz, and its setup is sketched in figure 7.1. The FPGA triggers the AOM and the camera, and when the image is transmitted to the computer, the FPGA reads the image in parallel. The image is not stored, but only processed to generate an error signal, so the FPGA only needs to access a minimal number of FIFOs. The error signal is passed on to the RF synthesizer, through the amplifier and to the RF coils used for evaporation.

The FPGA is controlled through a LabVIEW program that contains all settings for the Faraday laser and the camera. The program is executed when an ECS file appears on the hard drive as was done for the microwave setup. The FPGA then programs the camera by writing a file with the relevant camera settings to be read by a camera control script running in the Andor Solis environment.

In order to adjust the RF frequency for feedback, the FPGA must be able to control the RF synthesizer and generate the normal evaporation ramps. To this end, the RF ramp frequencies and durations are extracted from the current ECS file, and the FPGA calculates the ramps in a similar fashion as ECS does. To keep synchronisation with the DIO boards, each ramp of the RF is triggered by a TTL signal from the DIO boards. If the FPGA is faster than the DIO boards, it will keep the end frequency until receiving the next trigger.

For each of the sweeps defined in ECS, the FPGA is able to take a number of pictures. The number of pictures splits the sweep into the same number of sub-

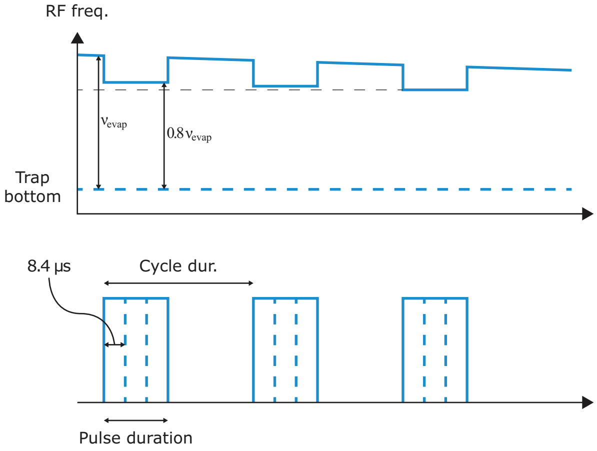

FIGURE 7.2: Application of RF cuts. A cut is triggered from the FPGA and is divided into a number of pulses of a given duration, and between each pulse is a delay set by the cycle duration. Both pulse duration and cycle duration is quantised in units of 8.4 µs. The cut always goes to a specified fraction of the effective trap depth.

sweeps, and in each sub-sweep, it is possible to apply feedback using settings that are defined for each sweep. It is also possible to vary the duration of the imaging pulse in each sweep, which is useful since more light is required to image hotter clouds at the beginning of the evaporation.

Although the FPGA operates at a clock frequency of 40 MHz, the RF synthesizers works at a lower clock rate, so it forces changes in the RF frequency to a quantisation of 8.4 µs. So far, this does not pose a problem, since the evaporation happens on a time scale set by the collision rate, which is around three orders of magnitude slower.

Adjustments in the RF frequency to effect the feedback are applied as “cuts” of a given duration and frequency. The frequency is determined as a fraction of the effective trap depth, $\nu_{\text{evap}} - \nu_{\text{bot}}$, where ν_{evap} is the current evaporation frequency and $\nu_{\text{bot}} = 540\,\text{kHz}$ is the trap bottom. This is to keep the effect of an RF cut approximately constant. The number of atoms lost in a single cut can be adjusted by varying the depth of the cut.

The effect of an RF cut is to transfer atoms to an untrapped state while not maintaining thermal equilibrium. Since the final state is lost from the trap, the effect of the RF cut is an exponential decrease in the atom number,

$$N' = N e^{-t/\tau}, \tag{7.1}$$

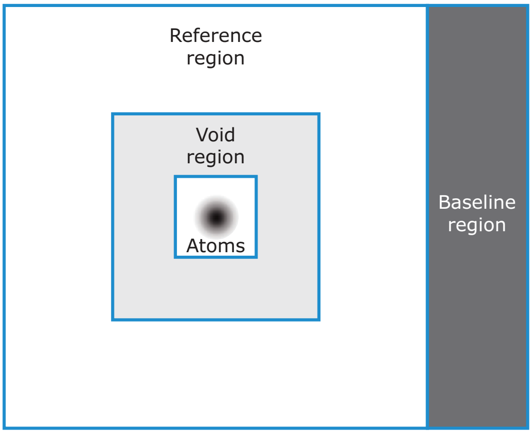

FIGURE 7.3: Imaging regions for Faraday detection. The atoms region is the inner square, the reference region excludes anything inside the void radius. The baseline region is shaded in dark grey.

where N is the initial atom number, N' is the final atom number, t is the duration of the RF pulse, and τ is the time constant for the loss. Following the principle behind evaporative cooling, only a small fraction will be resonant with the RF radiation, due to their Maxwell-Boltzmann distribution in the trap. Thus, the number of atoms lost with a deep cut is much larger than for a small cut due to the density of states, and the value of τ depends on the cut frequency.

When applying RF radiation to the ensemble, only a small spatial interval is addressed. By applying a long cut, it is easy to "saturate" the transition and remove all the atoms in a region. To avoid this, the cuts are divided into shorter pulses (see figure 7.2). The pulses are arranged in a cycle, and during the delay between pulses, atoms may repopulate the resonant region. Typically, a pulse is $1 \times 8.4\,\mu s$ and the cycle duration is $20 \times 8.4\,\mu s$, such that the atoms have $160\,\mu s$ to repopulate the spatial interval, where the cut is applied. The feedback quantity is thus the number of applied loss pulses.

For the actual imaging we use pulses of linearly polarised light that is 1 GHz blue detuned from the $F = 2 \rightarrow F' = 3$ transition. The incident light is shown in red in figure 7.1, and the interaction proceeds as described in section 3.4. After interacting with the atoms, some light is rotated to the perpendicular axis (blue in figure 7.1) due to the vectorial Faraday term in the Hamiltonian (2.75). The two polarisations are separated on a polarising beam splitter, and the rotated light is imaged on the CCD camera.

For the atom number analysis described in section 2.4 on page 31, two quantities are necessary: The intensity due to Faraday rotation $I(\theta)$ and the incident light intensity I_0. We may relate these to the experimental quantities as

$$I(\theta) = I'(\theta) - I_\mathrm{b} \tag{7.2}$$

$$I_0 = \frac{1}{\mathrm{CS}}\left(I'_0 - I_\mathrm{b}\right), \tag{7.3}$$

where $I'(\theta)$ is the signal from the camera, I_b is the baseline intensity, and I'_0 is the signal on the camera due to light leaking through the cube. These quantities may be extracted from an image, because the camera is masked. Three regions may be defined in an image, as shown in figure 7.3:

- *Atoms region*: A small region, where the atoms are present. This yields the intensity $I'(\theta)$.
- *Reference region*: This is taken further away from the cloud such that no atoms are present, and only the light leaking through the cube is detected, I'_0.
- *Baseline region*: This area is masked, so no light is present. The signal here defines the base level associated with camera noise, I_b.

7.2 Atom number estimation

In this section, the working principle behind calculating the atom number and finding the error function for feedback is discussed. More details are found in the progress report by Miroslav Gajdacz [95]

Image analysis

Using the leaking light in the reference region, the Faraday rotation angles may be calculated. However, it is faster for the FPGA only to work with the dimensionless, normalised signal defined as

$$S(\theta) \equiv \frac{I(\theta)}{I_0}. \tag{7.4}$$

As was shown in equation (2.81), the relevant quantity for studying the atom number is the rotation angle, so a conversion from signal to rotation angle is needed. This is given in equation (2.83).

Since the imaging light is incident along the Ioffe axis, the expected density profile is a symmetric Gaussian for a thermal cloud. For such a profile, the integrated rotation angle is [95]

$$\Sigma_\theta = \int r\,\mathrm{d}\phi\,\mathrm{d}r\,\theta(r) = 2\pi\sigma^2\theta_{\mathrm{max}}, \tag{7.5}$$

where θ_{max} is the peak rotation angle. Similarly, it may be shown that the integrated signal Σ_S is related to Σ_θ by

$$\Sigma_S = \Sigma_\theta\,\beta(\theta_{\mathrm{max}}), \tag{7.6}$$

where β is defined as

$$\beta(\theta) \equiv \frac{1}{\theta}\int_0^\theta \frac{\mathrm{d}\theta'\,\sin^2\theta'}{\theta'}. \tag{7.7}$$

All conversion information is thus contained in β. To make the FPGA faster, β is evaluated numerically as a polynomial, and it is used to fifth order

$$\beta(\theta) = \frac{\theta}{2} - \frac{\theta^3}{12} + \frac{\theta^5}{135} - \frac{\theta^7}{2520} + \ldots \tag{7.8}$$

However, it is easier to work in normalised error functions in order to determine the error function, which indicates how far the current atom number is from the reference. The error in atom number is given by

$$E_N = \frac{\Delta N}{N}, \tag{7.9}$$

where ΔN is the deviation from the desired atom number. This may be related to the relative error in the signal

$$E_N = \frac{\Delta\Sigma_S}{N}\frac{\partial N}{\partial\Sigma_S} = E_S\frac{\Sigma_S}{N}\frac{\partial N}{\partial\Sigma_S}, \tag{7.10}$$

where $E_S = \Delta\Sigma_S/\Sigma_S$ is the relative error in the signal. From equation (2.81) and equation (7.5) it is clear that

$$N \propto \theta_{\mathrm{max}}2\pi\sigma^2 = \theta_{\mathrm{max}}T, \tag{7.11}$$

where T is the temperature. Since the temperature is set by the RF evaporation, it will be constant for any image taken at a given point along the evaporation. Using this in equation (7.10) yields

$$E_N = E_S\frac{\Sigma_S}{\theta_{\mathrm{max}}}\frac{\partial\theta_{\mathrm{max}}}{\partial\Sigma_S}. \tag{7.12}$$

This relation shows that the relative error in atom number for a thermal cloud may be calculated by the relative error in signal translated by the proportionality factor α defined as

$$\frac{1}{\alpha} \equiv \frac{\Sigma_S}{\theta_{\max}} \frac{\partial \theta_{\max}}{\partial \Sigma_S}. \tag{7.13}$$

This is only a function of the peak rotation angle $\theta_{\max}$, so it may be computed from parameters that are extracted from the image.

To find the relation between α and β, we combine equations (7.6) and (7.11)

$$\Sigma_S \propto \beta(\theta_{\max}). \tag{7.14}$$

As the proportionality constants vanish when inserted in α, we obtain

$$\alpha = \frac{1}{\beta(\theta_{\max})} \frac{\partial}{\partial \theta_{\max}} \left[\beta(\theta_{\max})\,\theta_{\max}\right]. \tag{7.15}$$

This expression may be evaluated numerically yielding

$$\alpha = 2 - \frac{\theta_{\max}^2}{3} + \frac{\theta_{\max}^4}{250} + \ldots. \tag{7.16}$$

This shows that for small rotation angles, the conversion from error in signal to error in atom number just amounts to a division by 2.

Noise model

For the evaluation of the noise when measuring the atom number with this method, we derive a simple noise model. If we describe the number of electrons generated on a single CCD pixel as

$$N_{\mathrm{el}} = \eta N_{\mathrm{ph},0} S(\theta), \tag{7.17}$$

where η is the detection efficiency and $N_{\mathrm{ph},0}$ is the number photons incident on a single pixel. All loss process are taken into account by η, including the quantum efficiency of the camera. From equation (7.17), one finds the expression $S(\theta) = N_{\mathrm{el}}/\eta N_{\mathrm{ph},0}$, and by propagation of error, the variance in S is

$$\sigma_S^2 = \left(\frac{dS}{dN_{\mathrm{el}}}\right)^2 \sigma_{N_{\mathrm{el}}}^2 = \frac{1}{(\eta N_{\mathrm{ph},0})^2} N_{\mathrm{el}} = \frac{S(\theta)}{\eta N_{\mathrm{ph},0}}, \tag{7.18}$$

where Poissonian statistics were assumed for N_{el}.

To translate this into an uncertainty in atom number, we calculate the rotation angle θ, since, by equation (2.81), the angle is proportional to the atom number. If we assume that the angle is just

$$\theta = \arcsin\left(\sqrt{S}\right), \tag{7.19}$$

we may apply the propagation of error again. This yields

$$\begin{aligned}\sigma_\theta &= \left|\frac{d\theta}{dS}\right|\sigma_S = \frac{1}{2\sqrt{(1-S)S}}\sqrt{\frac{S}{\eta N_{\mathrm{ph},0}}} \\ &= \frac{1}{2\sqrt{(1-S)\eta N_{\mathrm{ph},0}}}.\end{aligned} \tag{7.20}$$

Since the number of photons is linear in the pulse duration τ

$$N_{\mathrm{ph},0} = \phi_0\tau, \tag{7.21}$$

where ϕ_0 is the photon flux.

This shows that the noise in atom number scales as $\tau^{-1/2}$, which is the equivalent of shot noise. Although the dependence of pulse duration is removed when calculating the signal, the shot noise caused by the pulse duration does not vanish. The effect of read-out noise may also be included in the model by adding a constant term to equation (7.17). This would appear as an additional term in equation (7.20) that is proportional to τ^{-1}. This is generally not relevant for our experiments, since we use EM gain, meaning that the number of photo-electrons is much larger than the read-out noise – even for very short pulses.

7.3 Experimental characterisation

Characterisation of imaging

The imaging setup was characterised following a sequence of two series of images separated by 9 s of evaporation. The first series of images was taken after 33 s of evaporation in the QUIC trap, and a total of 10 images was taken with a cycle time of 50 ms while keeping the evaporation frequency constant. The second series of images were taken after another 9 s of evaporation and consisted of 40 images also taken with a cycle time of 50 ms (see figure 7.4). This procedure was used to mimic a feedback sequence: First taking images to evaluate the error, applying feedback and afterwards evaluating the resulting atom number.

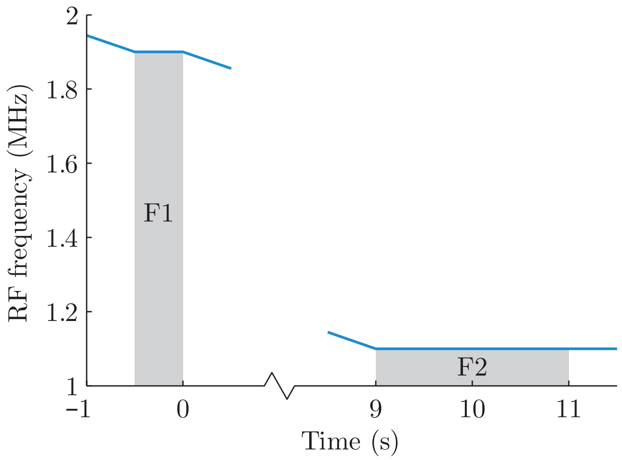

FIGURE 7.4: Sketch of the imaging procedure, where the grey areas mark the imaging series. When the evaporation frequency reaches 1.9 MHz, 10 images are taken (F1), while the RF frequency is kept constant. Afterwards, the evaporation continues, and at 1.1 MHz, another 40 images are taken.

The procedure was repeated for different imaging pulse durations and matching EM gains in order to exploit the full dynamic range of the camera, and for each setting, 15 repetitions were made. For every pulse duration, the first series (F1) used three times longer pulses than the second series (F2). In the following, i denotes the image number in the sequence, and j denotes different realisations of the same experimental sequence.

The destructiveness is defined as the relative decrease in atom number per image,

$$\Gamma \equiv \frac{1}{N}\frac{dN}{di}, \tag{7.22}$$

To characterise this slope, the atom number is calculated as the Faraday rotation angle summed of the image, Σ_θ. For each set of images, Σ_θ is fitted with a linear function, where the slope yields the loss of atoms, and the offset is the initial atom number. The destructiveness is then simply the slope normalised with the offset.

The summed Faraday angle for a F2 (F1) pulse duration of $500\,\mu\text{s}$ ($1500\,\mu\text{s}$) is shown in figure 7.5 (a). The fits show a small deviation from linearity, especially for the F2 pulses, which is attributed to the exponential character of the heating from the imaging pulses. The destructiveness is plotted against the pulse duration in figure 7.5 (b). The graph shows good linearity, and both the F1 (blue) and F2 (green)

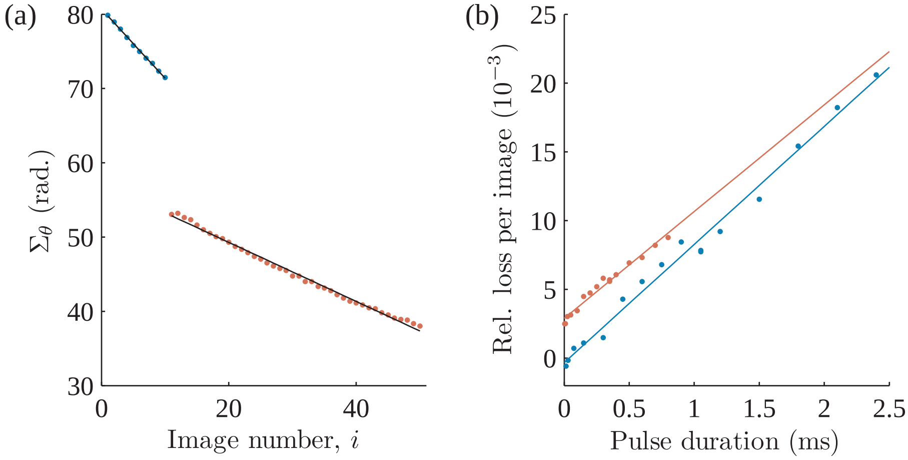

FIGURE 7.5: Evaluation of the destructiveness of the Faraday measurement technique. *(a)* The Atom number (represented by the summed Faraday angle) for a series of imaging pulses of duration 1500 µs (F1, blue dots) and 500 µs (F2, green dots). *(b)* Destructiveness versus imaging pulse duration for F1 (blue dots) and F2 (green dots) images. The data is fitted with a linear function yielding a slope of $8.6\times10^{-3}\,\text{image}^{-1}\mu\text{s}^{-1}$ for F1 and $7.8\times10^{-3}\,\text{image}^{-1}\mu\text{s}^{-1}$ for F2.

pulses have a similar slope of $\sim 8\times10^{-3}\,\text{image}^{-1}\mu\text{s}^{-1}$. The small offset on the data for F2 pulses is attributed to a decrease in signal due to evaporative cooling.

The fact that the increase of destructiveness with pulse duration is similar for F1 and F2 is somewhat surprising, since the imaging sequences occur at an effective trap depth of 1.9 MHz and 1.1 MHz respectively. The mechanism behind the destructiveness of the Faraday imaging is absorption of a photon, so each scattered photon should correspond to the absorption of one recoil energy $\hbar^2 k_{\text{ph}}^2/2m$, where k_{ph} is the wave number of the photon. The delivered energy should thus remove more atoms from the trap for F2 than for F1, since the effective trap depth is smaller for F2.

In order to evaluate the precision of the imaging, the signal error was calculated relative to the mean over j

$$E_{S,j} = \frac{S - \langle S\rangle_j}{\langle S\rangle_j}. \tag{7.23}$$

This normalises the mean atom loss approximately because the destructiveness due to the imaging is common to all repetitions of a single image i. For each repetition, the scatter may now be attributed to the measurement precision (MP), which

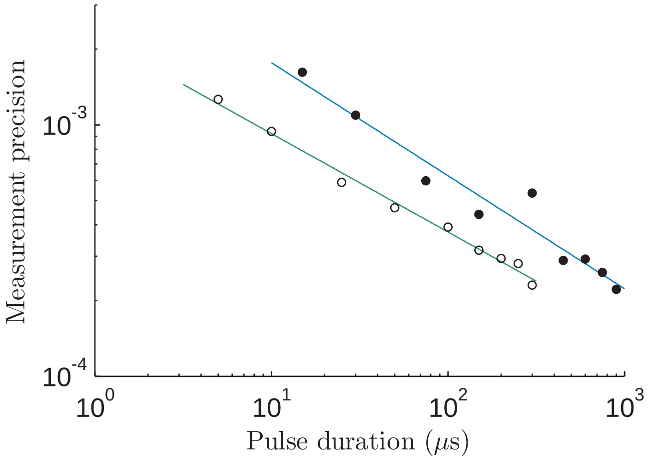

FIGURE 7.6: Measurement precision of Faraday imaging as defined by equation (7.25), but scaled by α to get the precision in atom number. The data is identical to that used for the destructiveness, i.e. 10 images for F1 and 40 images for F2, where each F1 pulse has three times the duration of each F2 pulse. Data is plotted double-logarithmically for F1 (black, filled circles) and for F2 (black, open circles). The straight-line fits correspond to a power function, yielding a slope of –0.45(4) for F1 (blue, solid) and –0.39(1) for F2 (green, solid).

we characterise by the two-sample deviation of the error [96]. We first calculate the two-sample variance of the error in signal

$$\sigma_{E_S}^2 = \frac{1}{2N_{\text{img}}} \left\langle (E_{S,i+1} - E_{S,i})^2 \right\rangle_i , \tag{7.24}$$

where N_{img} is the number of images taken. The error in signal is related to the error in atom number by the α factor, equation (7.16), which leads to the measurement precision

$$\text{MP} = \frac{\sigma_{E_S}}{\alpha}. \tag{7.25}$$

The resulting measurement precision derived from the same data as for the destructiveness is plotted against the pulse duration in figure 7.6 using a double-logarithmic plot. The slope of the fitted line gives the power law dependence on pulse duration, and for F1 it is –0.45(4) in good agreement with the –1/2 expected from equation (7.20). The precision reaches a value of 10^{-3} around 30 µs for F1 and roughly half this value for F2. This is expected, since F2 contains four times as many images.

Characterisation of RF cuts

The effect of making an RF cut into the cloud was also investigated. Experimentally, the cloud was imaged during all of the evaporation using 1 GHz blue detuning and EM gain of 80. After 18 s of evaporation, the imaging frequency was 2 images per second, and the pulse duration was 15 µs. After 30 images, a cut in the RF frequency was applied for variable duration and frequency. In order to keep sequences with different cut length comparable, the evaporation was “paused” for 50 ms at $\nu_{\text{evap}} = 1.9\,\text{MHz}$ during the cut. The cut was delivered in pulses of 8.4 µs using a pulse cycle of 168 µs.

From the data, the atom number N was calculated by division by β. The error was the found relative to an average atom number N_{ref} from 30 reference runs, where no cut was applied,

$$E_N = \frac{N}{N_{\text{ref}}} - 1. \tag{7.26}$$

The effect of the RF cut was quantified by the fraction of atoms left after the cut,

$$\frac{N^{(1)} - N^{(2)}}{N^{(1)}} = \frac{E_N^{(1)} - E_N^{(2)}}{E_N^{(1)} + 1}, \tag{7.27}$$

where the superscript 1 refers to before the cut and 2 refers to after the cut. In practice, these two values were found by averaging E_N over the 21 pictures before the cut and 30 pictures after the cut, respectively.

The data from two cuts, at 0.2 and 0.6 of the trap depth, is shown in figure 7.7 (a). The data has been fitted with an exponential decay, and the difference in time scale between the two cases is clear. The cut at 0.6 is exponential whereas the cut at 0.2 is so severe that the exponential model no longer fits the data. This is probably due to another loss mechanism, since the system is far away from equilibrium when cutting away atoms close to the mean energy.

In figure 7.7 (b), the loss rate $(1/\tau)$ is plotted versus the cut frequency. The loss rate is proportional to the number of atoms resonant with the RF radiation, and therefore it reflects the Maxwell-Boltzmann distribution of atoms in the trap. The distribution peaks close to 0.1 of the trap depth, indicating that the density of states peaks at this value.

An important outcome of the calibration is the gain for the feedback. The loss rate sets the required duration for cutting away a given fraction of the atoms. If a fraction δ needs to be cut, the effect of an RF cut should be

$$1 - \delta = e^{-t/\tau} \approx 1 - \frac{t}{\tau}. \tag{7.28}$$

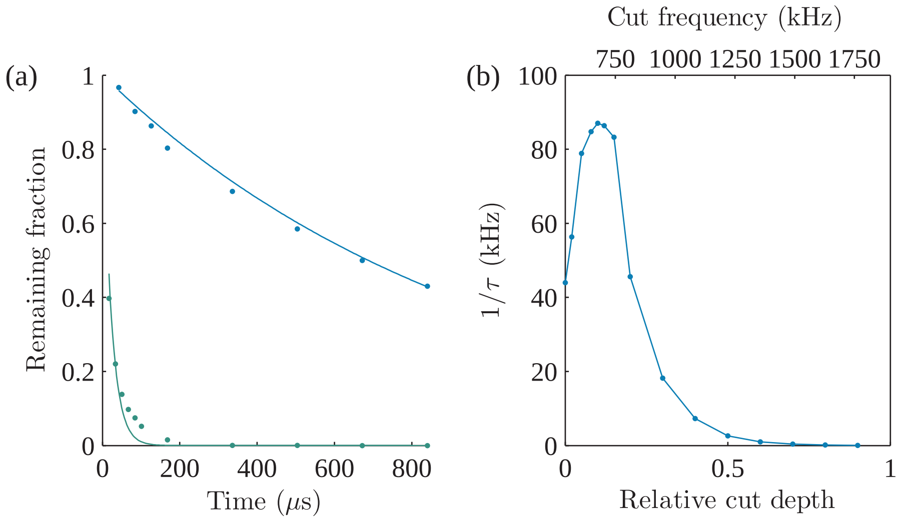

FIGURE 7.7: Calibration of the RF cut. *(a)* Effect of varying the duration of an RF cut for a cut to 0.60 (blue) and 0.20 (green) of the effective trap depth respectively. Here, the pulse duration was 8.4 µs and the cycle duration was 168 µs. Each set of data was fitted with an exponential decay. *(b)* The loss rate ($1/\tau$) for different cut depths. The curve shows, as expected, that a cut a low frequency is much more severe than a cut at a low frequency due to the distribution of atoms in the trap. Therefore, the shape of the curve reflects the Maxwell-Boltzmann distribution.

if the fraction is small,

$$t = \tau\delta. \tag{7.29}$$

This is of course an approximation, and in reality, experimental imperfections require an optimisation of the gain, as will be discussed in the following section.

7.4 Atom number stabilisation

The experimental approach for stabilising the atom number is to first evaporate for 33 seconds using the standard evaporation ramps. At this point, the evaporation frequency is 1.9 MHz, and the cloud is imaged to establish the atom number. During the imaging, the evaporation frequency is kept constant at 1.9 MHz (see figure 7.4).

The Faraday laser is locked at 1 GHz blue detuning, and 10 images are taken with a typical duration of 40 µs and an EM gain of 15. The imaging rate is 20 Hz, and the signal results from the 10 images are averaged to get an estimate of the atom number. It is advantageous to split the imaging into many pulses, since it avoids saturation of the camera, allowing a high integrated light level. The many pulses also provide statistics for each imaging series.

Following the imaging, the evaporation is resumed while applying the feedback pulses. After 9 s of evaporation, the evaporation frequency reaches 1.1 MHz, and another series of Faraday images is taken to measure the effect of the correction while keeping the evaporation constant. These images are taken with the same conditions, but a total of 40 images were taken, in order to achieve the highest possible imaging precision.

Alternatively, one could use standard absorption imaging to measure the effect of the feedback, but a comparison between absorption and Faraday imaging showed, that absorption imaging was less precise than Faraday imaging. This is caused by the fact that the integrated light level in non-destructive imaging can be much higher than for absorption imaging, since the effective well-depth of the camera is proportional to the number of images.

In order to evaluate the error signal, a reference atom number is needed. In practice, this number is calculated from 30 reference runs, where no feedback is applied, but using identical imaging conditions. The reference signal S_{ref} is then evaluated by averaging the signal over all 30 runs for each point in time. This approach makes the error signal insensitive to any systematic changes in signal during a run, since the trend is “divided” out of the signal. The reference runs are shown in figure 7.8 (a) and show the natural variation of the atom number.

Since the RF cuts are only able to remove atoms, it is important to set a “goal” that is lower than the fluctuating atom number. From the reference atom number, a desired fraction[1] x is chosen beforehand, and this is the set point from which the error signal is calculated

$$E_S = \frac{S}{S_{\text{ref}}} - x. \tag{7.30}$$

From the error, the duration of the RF cut is calculated from a gain expression. Empirically, it was found that a quadratic expression yielded good results

$$t = g E_S (1 + q E_S), \tag{7.31}$$

where g and q are parameters to be determined experimentally. The appearance of a quadratic term is attributed to experimental imperfections.

---

[1] This fraction is set in signal – not atom number – so it is not identical to the resulting atom number fraction.

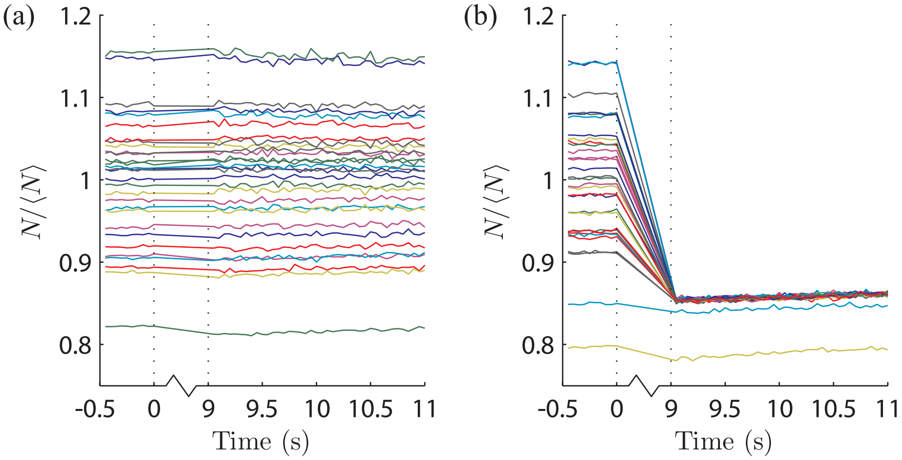

FIGURE 7.8: Atom number with and without feedback correction. Time zero indicates the point where feedback is applied. *(a)* Reference runs, no feedback is applied. *(b)* Feedback is applied to reach the goal $x = 0.675$ using a cut depth of 0.90 and a gain of $g = 3776 \times 8.4\,\mu\text{s}$ and $q = -0.215$.

The effect of activating the feedback is shown in figure 7.8 (b), where a gain of $g = 3776 \times 8.4\,\mu\text{s}$ and $q = -0.215$ was used along with a goal of $x = 0.675$. The RF cut was applied at 0.9 of the effective trap depth, and a typical cut duration was $\sim 13\,\text{ms}$.

Before applying the feedback, the images show the same spread in atom number as in figure 7.8 (a), where no feedback is applied. After the RF cut, however, the spread in atom number reduces drastically. Only the sequences, where the atom number was below the desired 86% of the reference atom number, show deviation from the small spread, but these may easily be rejected *a posteriori*, since the output from the FPGA shows that no feedback was applied.

In order to find the optimal gain, it is useful to determine the correlation between the measurement before the feedback and after the feedback. Such a plot is shown in figure 7.9 (a), and the slope of the points show how close the gain is to the optimal value. If the slope is positive, the FPGA does not apply enough feedback for large atom numbers, and the gain is too low. On the contrary, if the slope is negative, the FPGA overcompensates the large atom numbers, and the gain is too large. Only for a flat line is the atom number correctly compensated leaving no correlation between the two measurements.

A closeup of the resulting correlation is plotted in figure 7.9 (b) showing that

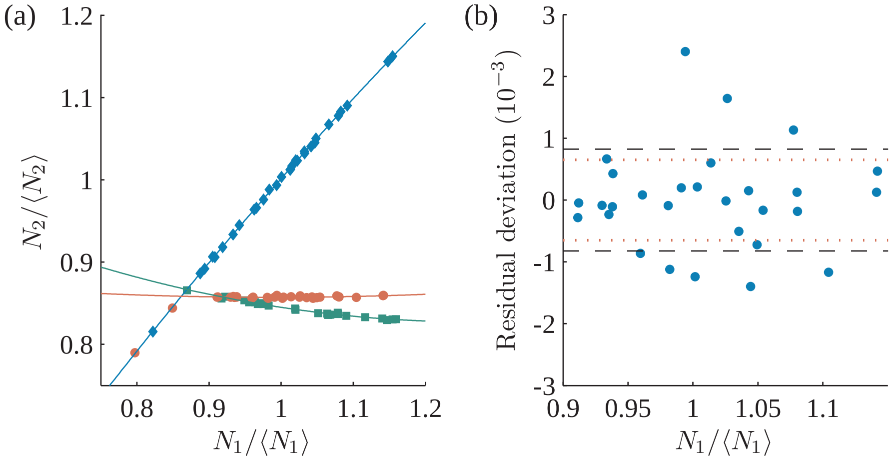

FIGURE 7.9: Correlation of the two measurements. *(a)* Correlation of the initial (F1) and final (F2) atom number for three different settings of the gain. Data is shown without feedback (blue), with an over-compensated gain setting (green), and with an optimal gain setting (red). For each data point, the atom number was evaluated by averaging the atom number over 10 images before the RF cut and over 40 images after applying the RF cut. *(b)* Closeup of the data shown in (a) for optimal gain settings. The measurement precision is shown as dotted lines and the standard deviation of the is shown as dashed lines.

the stability is 8×10^{-4} (black line, dashed). The stability before feedback is 7.7%, so the feedback improves the stability by a factor of 80. This shows, that single-step feedback is a fruitful approach to stabilizing the atom number.

The limiting factor at the moment seems to be the measurement precision of F1. The expected noise in F2 is 6.4×10^{-4} (red line, dotted), and consist of a two contributions: One from the measurement precision of F2, and one from the measurement precision of F1 used for the feedback. The latter is found from propagation of error

$$\sigma_{F1} = \left|\frac{dE_{S2}}{dE_{S1}}\right|\sigma_{S1}, \tag{7.32}$$

where σ_{S1} is the measurement precision for F1. The derivative dE_{S2}/dE_{S1} is just the correlation between the two measurements, and this is not 1 due to the nonlinearity of the α factor.

When adding the terms in quadrature and converting the result to atom number instead of signal[2], we obtain the aforementioned 6.5×10^{-4}. The measurement precision for F2 is just 2.9×10^{-4}, indicating that the limiting factor at present is the measurement precision for F1.

Another interesting aspect of the noise after feedback is that the measured uncertainty is so close to the expected uncertainty due to feedback. This means that the noise from other sources, σ_{oth} is limited, as such a contribution should be added in quadrature

$$\sigma_{\text{tot}} = \sqrt{\sigma_{F1}^2+\sigma_{F2}^2+\sigma_{\text{oth}}^2}. \tag{7.33}$$

With the measured noise, the residual noise is $\sigma_{\text{oth}} = 5.0\times10^{-4}$, but the uncertainty of this number is high, since subtraction of two similar numbers squared varies dramatically with the exact numbers.

However, this still indicates that any noise due to the evaporation is small, which is promising for the effort of creating a BEC with the same stability as the current thermal cloud. Since the evaporation is a stochastic process, it should add some noise, as should the stochasticity of the number of atoms lost in the RF cut. Both noise sources are subjects for future investigations.

Another subject of interest is the effect of trap bottom drifts. Small variations in the coil – typically from temperature changes in the cooling water – cause a similar change in the magnetic field and shift the bottom of the trap slightly. This effect is normally on the order of kHz and should not pose a problem for the current experiments that work at least 500 kHz above the trap bottom. However, for the creation of a BEC, such changes are of high importance since the end frequency typically is only tens of kHz above the trap bottom. It would therefore be highly relevant to consider ways of correcting for the trap bottom drifts through feedback. One way would be to apply two-step feedback: One at an early stage in the evaporation where the trap bottom drift is negligible, and one near the end of the evaporation, where the drift is important. The trap bottom could then be adjusted through an offset field, which should lead to a very reliable production of a condensate.

To summarise, our current experiments employs a single-step feedback algorithm as a first approach to atom number stabilisation. The preliminary results show a stability of 8×10^{-4} with an atom number of 1.8×10^{6}, and this brings us very close to the Poissonian noise of 7.5×10^{-4}. Future experiments will explore the origin of the measured noise, and investigate the prospects of using two-step feedback.

---

[2] For this purpose, the conversion was made by calibrating the E_S against the error in atom number measured by absorption imaging. This is equivalent to calculating the α factor from the average peak angle.

CHAPTER 8

OUTLOOK AND CONCLUSION

In this thesis, new tools for manipulating coherent ensembles of ultracold atoms in optical lattices were presented. The creation and localisation of wave packets through amplitude modulation of the lattice offers new means of quantum state engineering. The investigation of spinor condensates in two dimensions reveals correlations in both spin and momentum. Also, ongoing investigations using feedback with Faraday detection shows promising results in stabilising the atom number below one permille.

The work on wave packets in optical lattices allowed for the creation of a pair of wave packets propagating in the 4th excited band which is unbound by the lattice. Subsequent modulation pulses deexcites the wave packets into the 1st excited band where the atoms stay localised for hundreds of milliseconds.

The deexcitation pulse works as a beam splitter for a matter wave, splitting a fraction into the localised state. By varying the modulation frequency, amplitude and duration allows one to tune the splitting fraction and deexcitation band, and for deexcitation to the 1st excited band, an efficiency approaching unity can be realised. The localised states can also be addressed by RF radiation, sweeping the frequency to expel atoms from the trap.

Thus, the localised states work as a quantum register, where atoms may be stored in different sites or different lattice band. In particular, a superposition of atoms in two different bands would imitate a qubit, and coupling the two bands, using e.g. phase modulation of the lattice, would resemble a quantum gate.

In the field of spin dynamics, the production of correlated clouds of $|2,\pm1\rangle$ atoms in a one-dimensional optical lattice extended previous work on spinor gases [34–36] to a multi-mode regime. Here, the spatial eigenmodes of the trap are not resolved, but superpositions appear leading to distinct ring structures in time-of-flight. Furthermore, it was shown that the $|\pm1\rangle$ clouds exhibit spatial anti-correlation. Future experiments will focus on investigating a single lattice site in which the spinor dynamics would not suffer from interference from other sites. Such an experiment might shed light on the effect of bosonic stimulation during the spin-changing collisions.

To aid future experiments on spin dynamics, a crossed dipole trap was built. The successful creation of a BEC in this trap was demonstrated, and prospective applications were illustrated. Spin dynamics also occurs in the dipole trap, and loading an optical lattice from the dipole was also achieved. The dipole trap could also be used with cylindrical lenses to create a two-dimensional cloud. This would open up interesting ways to continue the spinor experiments, since the dipole trap would only feature a single two-dimensional site yielding easier identification of ring structures and possible wave packets.

Finally, preliminary results towards atom number stabilisation using Faraday feedback were presented. Using non-destructive Faraday detection, the atom number was measured and subsequently corrected using cuts in the RF evaporation frequency. This method has so far led to atom number stability below one permille, and further investigation will explore the possibility of reaching the Poissonian limit of $\sqrt{N}$ uncertainty.

The prospective application of atom number stabilisation has great potential for improving the statistics of other experiments such as the spinor dynamics. The inherent uncertainty due to the stochastic nature of the parametric amplification would be isolated, leading to improved statistics of atom number measurements. Finally, all experiments that measure small losses, such as current efforts towards observing Efimov states [97], would benefit from high stability of the initial atom number.

APPENDIX A

THE BOGOLIUBOV TRANSFORMATION

Starting from a Hamiltonian on the form of equation (5.23), we omit the indices and work only with the two operators $\hat{a}$ and $\hat{b}$ yielding the Hamiltonian

$$\hat{H} = D\left(\hat{a}^\dagger \hat{a} + \hat{b}^\dagger \hat{b}\right) + U\left(\hat{a}^\dagger \hat{b}^\dagger + \hat{a}\hat{b}\right). \tag{A.1}$$

The two Bogoliubov operators are then defined as

$$\begin{aligned} \hat{\alpha} &= u\hat{a} + v\hat{b}^\dagger \\ \hat{\beta} &= u\hat{b} + v\hat{a}^\dagger, \end{aligned} \tag{A.2}$$

where the coefficients u and v can be any complex number in general. However, as a starting point, it is convenient to choose u and v to be real, as the phase of the operators does not contain any physical meaning in itself. For the particle described by $\hat{\alpha}$ and $\hat{\beta}$ to be a boson, it should fulfill the Bose commutator relations

$$\left[\hat{\alpha},\, \hat{\alpha}^\dagger\right] = \left[\hat{\beta},\, \hat{\beta}^\dagger\right] = 1 \tag{A.3}$$

$$\left[\hat{\alpha},\, \hat{\beta}\right] = \left[\hat{\alpha}^\dagger,\, \hat{\beta}^\dagger\right] = \left[\hat{\alpha},\, \hat{\beta}^\dagger\right] = \left[\hat{\alpha}^\dagger,\, \hat{\beta}\right] = 0. \tag{A.4}$$

Given that $\hat{a}$ and $\hat{b}$ fulfill these relations, insertion of equation (A.2) yields

$$\begin{aligned} 1 &= (u\hat{a} + v\hat{b}^\dagger)(u\hat{a}^\dagger + v\hat{b}) - (u\hat{a}^\dagger + v\hat{b})(u\hat{a} + v\hat{b}^\dagger) \\ &= u^2(\hat{a}\hat{a}^\dagger - \hat{a}^\dagger\hat{a}) + v^2(\hat{b}\hat{b}^\dagger - \hat{b}^\dagger\hat{b}) \\ &= u^2 - v^2, \end{aligned}$$

which is conveniently parametrized by hyperbolic functions

$$u = \cosh(t) \tag{A.5}$$

$$v = \sinh(t). \tag{A.6}$$

The inverse transformation is simply

$$\hat{a} = u\hat{\alpha} - v\hat{\beta}^\dagger \tag{A.7}$$

$$\hat{b} = u\hat{\beta} - v\hat{\alpha}^\dagger, \tag{A.8}$$

which is used to describe the Hamiltonian in terms of $\hat{\alpha}$ and $\hat{\beta}$

$$\hat{H} = D\left[(u\hat{\alpha}^\dagger - v\hat{\beta})(u\hat{\alpha} - v\hat{\beta}^\dagger) + (u\hat{\beta}^\dagger - v\hat{\alpha})(u\hat{\beta} - v\hat{\alpha}^\dagger)\right] \tag{A.9}$$

$$+ U\left[(u\hat{\alpha}^\dagger - v\hat{\beta})(u\hat{\beta}^\dagger - v\hat{\alpha}) + (u\hat{\beta} - v\hat{\alpha}^\dagger)(u\hat{\alpha} - v\hat{\beta}^\dagger)\right]. \tag{A.10}$$

When the parentheses are removed, terms of the kind $\hat{a}\hat{a}^\dagger$ appear, which may be removed by use of the commutator $\hat{a}\hat{a}^\dagger = 1 + \hat{a}^\dagger\hat{a}$. The Hamiltonian now reads

$$\begin{aligned}
\hat{H} &= 2v^2D + D(u^2+v^2)(\hat{\alpha}^\dagger\hat{\alpha} + \hat{\beta}^\dagger\hat{\beta}) - 2uvD(\hat{\alpha}^\dagger\hat{\beta}^\dagger + \hat{\alpha}\hat{\beta}) \\
&\quad + U(u^2+v^2)(\hat{\alpha}^\dagger\hat{\beta}^\dagger + \hat{\alpha}\hat{\beta}) - 2Uuv(\hat{\alpha}^\dagger\hat{\alpha} + \hat{\beta}^\dagger\hat{\beta} + 1). \\
&= 2v^2D - 2uvU + \left[D(u^2+v^2) - 2Uuv\right](\hat{\alpha}^\dagger\hat{\alpha} + \hat{\beta}^\dagger\hat{\beta}) \\
&\quad + \left[U(u^2+v^2) - 2Duv\right](\hat{\alpha}^\dagger\hat{\beta}^\dagger + \hat{\alpha}\hat{\beta}).
\end{aligned}$$

The last expression is diagonal in $\hat{\alpha}$ and $\hat{\beta}$, if the term $U(u^2+v^2) - 2Duv$ can be set to zero. Luckily, there is still a degree of freedom left in the parametrization, namely the choice of t. This choice of t leads to a parametrization

$$0 = U\left(\cosh^2 t + \sinh^2 t\right) - 2D\cosh t \sinh t,$$

which using the square formulas is equal to

$$= U\cosh 2t - 2D\cosh t\sinh t.$$

The double angle formula gives

$$= U\cosh 2t - D\sinh 2t,$$

and the parametrization is thus

$$\tanh 2t = U/D. \tag{A.11}$$

From the definition of the inverse hyperbolic tangent, the value of t may be isolated as

$$t = \frac{1}{4}\ln\left(\frac{x+1}{1-x}\right), \tag{A.12}$$

where $x = U/D$. This, in turn, leads to the explicit expressions for u and v given the choice of t. From the definition of u, (A.5), we have

$$\begin{aligned} u = \tfrac{1}{2}\left(e^{t} + e^{-t}\right) &= \frac{1}{2}\left(\sqrt{\frac{1+U/D}{1-U/D}} + \sqrt{\frac{1-U/D}{1+U/D}}\right) \\ &= \frac{1}{2}\frac{\sqrt{D+U}+\sqrt{D-U}}{\sqrt[4]{D^2-U^2}}, \end{aligned}$$

where the identity $(a+b)(a-b) = a^2 - b^2$ was applied. Squaring the entire expression leads to

$$u^2 = \frac{1}{4}\frac{2D+2\sqrt{D^2-U^2}}{\sqrt{D^2-U^2}}, \tag{A.13}$$

which motivates the definition

$$\epsilon = \sqrt{D^2-U^2}. \tag{A.14}$$

The coefficient u is then

$$u^2 = \frac{1}{2}\left(\frac{D}{\epsilon}+1\right), \tag{A.15}$$

and following a similar calculation, we find

$$v^2 = \frac{1}{2}\left(\frac{D}{\epsilon}-1\right). \tag{A.16}$$

Returning to the Hamiltonian,

$$\hat{H} = 2v^2D - 2uvU + \left[D(u^2+v^2) - 2Uuv\right](\hat{\alpha}^\dagger\hat{\alpha} + \hat{\beta}^\dagger\hat{\beta}), \tag{A.17}$$

the product uv needs to be calculated, which is simply $uv = \frac{1}{2}U/\epsilon$. Insertion of all expression leads to

$$\begin{aligned} \hat{H} &= \frac{D^2-U^2}{\epsilon} - D + \left[\frac{D^2-U^2}{\epsilon}\right](\hat{\alpha}^\dagger\hat{\alpha} + \hat{\beta}^\dagger\hat{\beta}) \qquad \text{(A.18)} \\ &= \epsilon - D + \epsilon(\hat{\alpha}^\dagger\hat{\alpha} + \hat{\beta}^\dagger\hat{\beta}). \qquad \text{(A.19)} \end{aligned}$$

This expression shows that the ground state energy of the system is $\epsilon - D$ and that any excitation is a quasi-particle with energy ϵ.

BIBLIOGRAPHY

[1] Albert Einstein. Quantentheorie des einatomigen idealen gases. *Sitzungsberichte der Preussischen Akademie der Wissenschaften*, 1:3, 1925.

[2] Satyendra Nath Bose. Plancks Gesetz und Lichtquantenhypotese. *Zeitschrift für Physik*, 26:178–181, 1924.

[3] F. London. The λ-phenomenon of liquid helium and the Bose-Einstein degeneracy. *Nature*, 141:643, 1938.

[4] A. J. Leggett. Superfluidity. *Rev. Mod. Phys.*, 71:S318–S323, Mar 1999.

[5] M. H. Anderson, J. R. Ensher, M. R. Matthews, C. E. Wieman, and E. A. Cornell. Observation of Bose-Einstein condensation in a dilute atomic vapor. *Science*, 269(5221):198–201, 1995.

[6] C. C. Bradley, C. A. Sackett, J. J. Tollett, and R. G. Hulet. Evidence of Bose-Einstein condensation in an atomic gas with attractive interactions. *Phys. Rev. Lett.*, 75:1687–1690, Aug 1995.

[7] K. B. Davis, M. O. Mewes, M. R. Andrews, N. J. van Druten, D. S. Durfee, D. M. Kurn, and W. Ketterle. Bose-einstein condensation in a gas of sodium atoms. *Phys. Rev. Lett.*, 75:3969–3973, Nov 1995.

[8] Nobelprize.org. "Press release: The 2001 Nobel prize in physics", 2001.

[9] M. R. Andrews, C. G. Townsend, H.-J. Miesner, D. S. Durfee, D. M. Kurn, and W. Ketterle. Observation of interference between two Bose condensates. *Science*, 275(5300):637–641, 1997.

[10] Immanuel Bloch, Theodor W. Hänsch, and Tilman Esslinger. Atom laser with a cw output coupler. *Phys. Rev. Lett.*, 82:3008–3011, Apr 1999.

[11] M. R. Matthews, B. P. Anderson, P. C. Haljan, D. S. Hall, C. E. Wieman, and E. A. Cornell. Vortices in a Bose-Einstein condensate. *Phys. Rev. Lett.*, 83:2498–2501, Sep 1999.

[12] K. W. Madison, F. Chevy, W. Wohlleben, and J. Dalibard. Vortex formation in a stirred Bose-Einstein condensate. *Phys. Rev. Lett.*, 84:806–809, Jan 2000.

[13] Axel Griesmaier, Jörg Werner, Sven Hensler, Jürgen Stuhler, and Tilman Pfau. Bose-Einstein condensation of chromium. *Phys. Rev. Lett.*, 94:160401, Apr 2005.

[14] Yosuke Takasu, Kenichi Maki, Kaduki Komori, Tetsushi Takano, Kazuhito Honda, Mitsutaka Kumakura, Tsutomu Yabuzaki, and Yoshiro Takahashi. Spin-singlet Bose-Einstein condensation of two-electron atoms. *Phys. Rev. Lett.*, 91:040404, Jul 2003.

[15] B. P. Anderson and M. A. Kasevich. Macroscopic quantum interference from atomic tunnel arrays. *Science*, 282(5394):1686–1689, 1998.

[16] D. Jaksch, C. Bruder, J. I. Cirac, C. W. Gardiner, and P. Zoller. Cold bosonic atoms in optical lattices. *Phys. Rev. Lett.*, 81:3108–3111, Oct 1998.

[17] Markus Greiner, Olaf Mandel, Tilman Esslinger, Theodor W. Hansch, and Immanuel Bloch. Quantum phase transition from a superfluid to a Mott insulator in a gas of ultracold atoms. *Nature*, 415(6867):39–44, January 2002.

[18] J. Struck, C. Oelschlaeger, R. Le Targat, P. Soltan-Panahi, A. Eckardt, M. Lewenstein, P. Windpassinger, and K. Sengstock. Quantum Simulation of Frustrated Classical Magnetism in Triangular Optical Lattices. *SCIENCE*, 333(6045):996–999, AUG 19 2011.

[19] P. Soltan-Panahi, J. Struck, P. Hauke, A. Bick, W. Plenkers, G. Meineke, C. Becker, P. Windpassinger, M. Lewenstein, and K. Sengstock. Multi-component quantum gases in spin-dependent hexagonal lattices. *Nat Phys*, 7(5):434–440, May 2011.

[20] Richard P. Feynmann. Simulating physics with computers. *Int. J. Theor. Phys.*, 21(6/7):467, 1982.

[21] Immanuel Bloch, Jean Dalibard, and Sylvain Nascimbéne. Quantum simulations with ultracold quantum gases. *Nat Phys*, 8:267–276, 2012.

[22] J. F. Sherson, C. Weitenberg, M. Endres, M. Channeau, I. Bloch, and S. Kuhr. Single-atom-resolved fluorescence imaging of an atomic mott insulator. *Nature*, 467:68, 2010.

[23] Christof Weitenberg, Manuel Endres, Jacob F. Sherson, Marc Cheneau, Peter Schausz, Takeshi Fukuhara, Immanuel Bloch, and Stefan Kuhr. Single-spin addressing in an atomic Mott insulator. *Nature*, 471(7338):319–324, March 2011.

[24] D. M. Stamper-Kurn, M. R. Andrews, A. P. Chikkatur, S. Inouye, H.-J. Miesner, J. Stenger, and W. Ketterle. Optical confinement of a Bose-Einstein condensate. *Phys. Rev. Lett.*, 80:2027–2030, Mar 1998.

[25] J. Stenger, S. Inouye, D. M. Stamper-Kurn, H.-J. Miesner, A. P. Chikkatur, and W. Ketterle. Spin domains in ground-state Bose-Einstein condensates. *Nature*, 396(6709):345–348, November 1998.

[26] Tin-Lun Ho. Spinor Bose condensates in optical traps. *Phys. Rev. Lett.*, 81:742–745, 1998.

[27] M.-S. Chang, C. D. Hamley, M. D. Barrett, J. A. Sauer, K. M. Fortier, W. Zhang, L. You, and M. S. Chapman. Observation of spinor dynamics in optically trapped ^{87}Rb bose-einstein condensates. *Phys. Rev. Lett.*, 92:140403, Apr 2004.

[28] H. Schmaljohann, M. Erhard, J. Kronjäger, M. Kottke, S. van Staa, L. Cacciapuoti, J. J. Arlt, K. Bongs, and K. Sengstock. Dynamics of $f = 2$ spinor Bose-Einstein condensates. *Phys. Rev. Lett.*, 92:040402, Jan 2004.

[29] C. V. Ciobanu, S.-K. Yip, and Tin-Lun Ho. Phase diagrams of $f = 2$ spinor Bose-Einstein condensates. *Phys. Rev. A*, 61:033607, 2000.

[30] Artur Widera, Fabrice Gerbier, Simon Fölling, Tatjana Gericke, Olaf Mandel, and Immanuel Bloch. Coherent collisional spin dynamics in optical lattices. *Phys. Rev. Lett.*, 95:190405, Nov 2005.

[31] M. S. Chang, Q. Qin, W. Zhang, L. You, and M. S. Chapman. Coherent spinor dynamics in a spin-1 Bose condensate. *Nature Phys.*, 1:111, 2005.

[32] L. E. Sadler, J. M. Higbie, S. R. Leslie, M. Vengalattore, and D. M. Stamper-Kurn. Spontaneous symmetry breaking in a quenched ferromagnetic spinor Bose-Einstein condensate. *Nature*, 443(7109):312–315, September 2006.

[33] Y. Liu, S. Jung, S. E. Maxwell, L. D. Turner, E. Tiesinga, and P. D. Lett. Quantum phase transitions and continuous observation of spinor dynamics in an antiferromagnetic condensate. *Phys. Rev. Lett.*, 102:125301, Mar 2009.

[34] C. Klempt, O. Topic, G. Gebreyesus, M. Scherer, T. Henninger, P. Hyllus, W. Ertmer, L. Santos, and J. J. Arlt. Multiresonant spinor dynamics in a Bose-Einstein condensate. *Phys. Rev. Lett.*, 103:195302, Nov 2009.

[35] C. Klempt, O. Topic, G. Gebreyesus, M. Scherer, T. Henninger, P. Hyllus, W. Ertmer, L. Santos, and J. J. Arlt. Parametric amplification of vacuum fluctuations in a spinor condensate. *Phys. Rev. Lett.*, 104:195303, May 2010.

[36] M. Scherer, B. Lücke, G. Gebreyesus, O. Topic, F. Deuretzbacher, W. Ertmer, L. Santos, J. J. Arlt, and C. Klempt. Spontaneous breaking of spatial and spin symmetry in spinor condensates. *Phys. Rev. Lett.*, 105:135302, Sep 2010.

[37] B. Lücke, M. Scherer, J. Kruse, L. Pezzé, F. Deuretzbacher, P. Hyllus, O. Topic, J. Peise, W. Ertmer, J. Arlt, L. Santos, A. Smerzi, and C. Klempt. Twin matter waves for interferometry beyond the classical limit. *Science*, 334(6057):773–776, 2011.

[38] Bernd Lücke, Jan Peise, Giuseppe Vitagliano, Jan Arlt, Luis Santos, Géza Tóth, and Carsten Klempt. Detecting multiparticle entanglement of dicke states. *Phys. Rev. Lett.*, 112:155304, Apr 2014.

[39] A. Einstein, B. Podolsky, and N. Rosen. Can quantum-mechanical description of physical reality be considered complete? *Phys. Rev.*, 47:777, 1935.

[40] Henrik Kjær Andersen. *Bose-Einstein condensates in optical lattices.* PhD thesis, Department of Physics and Astronomy, Aarhus University, 2008.

[41] Jesper Fevre Bertelsen. *Ultracold Atomic Gases.* PhD thesis, Department of Physics and Astronomy, Aarhus University, 2007.

[42] Lev Pitaevskii and Sandro Stringari. *Bose-Einstein Condensation.* The International Series of Monographs on Physics. Oxford University Press, 2003.

[43] Kerson Huang. *Statistical mechanics.* John Wiley & Sons, 1963.

[44] C.J. Pethick and H. Smith. *Bose-Einstein Condensation in Dilute Gases.* University Press, Cambridge, second edition, 2002.

[45] B.H. Bransden and C.J. Joachain. *Physics of Atoms and Molecules.* Prentice Hall, 2003.

[46] Dan M. Stamper-Kurn and Masahito Ueda. Spinor Bose gases: Symmetries, magnetism, and quantum dynamics. *Rev. Mod. Phys.*, 85:1191–1244, Jul 2013.

[47] Gebremedhn Gebreyesus Hagoss. *Parametric Amplification in Spinor Bose-Einstein Condensates.* PhD thesis, Institut für Theoretische Physik, Leibniz Universität Hannover, 2010.

[48] N. Bogoliubov. On the theory of superfluidity. *J. Phys. USSR*, 11:23, 1947.

[49] Frank Deuretzbacher. Private communication.

[50] Daniel A. Steck. Rubidium 87 d line data. available online at `http://steck.us/alkalidata`, 2010.

[51] Allen L. and J. Eberly. *Optical resonance and two-level atoms.* Dover Pbblications, 1975.

[52] G. Reinaudi, T. Lahaye, Z. Wang, and D. Guéry-Odelin. Strong saturation absorption imaging of dense clouds of ultracold atoms. *Opt. Lett.*, 32(21):3143–3145, Nov 2007.

[53] Leonard I. Schiff. *Quantum mechanics.* McGraw-Hill, 1968.

[54] Nils Winter. *Creation of ^{39}K Bose-Einstein condensates with tunable interaction.* PhD thesis, Department of Physics and Astronomy, Aarhus University, 2013.

[55] Robert D. Guenther. *Modern optics.* John Wiley, 1990.

[56] Daniel A. Steck. Quantum and atom optics. available online at `http://steck.us/teaching`, 2006.

[57] John Stockton. *Continuous Quantum Measurement of Cold Alkali-Atom Spins.* PhD thesis, California Institute of Technology, 2007.

[58] Marcin Kubasik. *Towards Spin Squeezing in Cold Atomic Ensembles.* PhD thesis, Departament de Física Aplicada, 2009.

[59] M. Gajdacz, P. L. Pedersen, T. Mørch, A. Hilliard, J. Sherson, and J. Arlt. Non-destructive faraday imaging of dynamically controlled ultracold atoms. *Rev. Sci. Instr.*, 84(8):083105, 2013.

[60] J. J. Sakurai. *Modern Quantum Mechanics.* Addison-Wesley, 1994.

[61] R. Grimm and and Y. Ovchinnikov M.Weidemuller. Optical dipole traps for neutral atoms. *Adv. At. Mol. Opt. Phys.*, 42:95, 2000.

[62] Peter Milonni and Joseph Eberly. *Lasers.* Wiley, 1988.

[63] Philip Hofmann. *Solid State Physics: An Introduction.* Wiley-VCH, 2008.

[64] Neil W. Ashcroft and N. David Mermin. *Solid State Physics.* Thomson Learning, 1976.

[65] Markus Greiner. *Ultracold quantum gases in three-dimensional optical lattice potentials.* PhD thesis, Ludwig-Maximilians-Universität München, 2003.

[66] J Hecker Denschlag, J E Simsarian, H Häffner, C McKenzie, A Browaeys, D Cho, K Helmerson, S L Rolston, and W D Phillips. A Bose-Einstein condensate in an optical lattice. *Journal of Physics B: Atomic, Molecular and Optical Physics*, 35(14):3095, 2002.

[67] T. Gericke, F. Gerbier, A. Widera, S. Fölling, O. Mandel, and I. Bloch. Adiabatic loading of a Bose-Einstein condensate in a 3D optical lattice. *Journal of Modern Optics*, 54(5):735–743, 2007.

[68] Harold J. Metcalf and Peter van der Straaten. *Laser Cooling and Trapping.* Springer, 1999.

[69] L. Ricci, M. Weidemüller, T. Esslinger, A. Hemmerich, C. Zimmermann, V. Vuletic, W. König, and T.W. Hänsch. A compact grating-stabilized diode laser system for atomic physics. *Optics Communications*, 117(56):541 – 549, 1995.

[70] Henrik Kjær Andersen. Opbygning af et rubidium MOT lasersystem (only available in danish). Bachelor rapport, 2003.

[71] Romain Müller. Towards a high-resolution, non-destructive imaging experiment. Progress report, 2013.

[72] F. Kaminski, N.S. Kampel, M.P.H. Steenstrup, A. Griesmaier, E.S. Polzik, and J.H. Müller. In-situ dual-port polarization contrast imaging of faraday rotation in a high optical depth ultracold 87rb atomic ensemble. *The European Physical Journal D*, 66(9):227, 2012.

[73] *Andor DU-888 Specifications.*

[74] Eugene Hecht. *Optics.* Addison-Wesley, fourth edition, 2002.

[75] Kristoffer Theis Skalmstang. Microwave transistions of ^{87}rb hyperfine structure through direct digital synthesis. Bachelor rapport, 2014.

[76] Ferenc Krausz and Misha Ivanov. Attosecond physics. *Rev. Mod. Phys.*, 81:163–234, Feb 2009.

[77] J. Heinze, J. S. Krauser, N. Fläschner, B. Hundt, S. Götze, A. P. Itin, L. Mathey, K. Sengstock, and C. Becker. Intrinsic photoconductivity of ultracold fermions in optical lattices. *Phys. Rev. Lett.*, 110:085302, Feb 2013.

[78] H. Ott, E. de Mirandes, F. Ferlaino, G. Roati, V. Türck, G. Modugno, and M. Inguscio. Radio frequency selective addressing of localized atoms in a periodic potential. *Phys. Rev. Lett.*, 93:120407, Sep 2004.

[79] Jacob F Sherson, Sung Jong Park, Poul L Pedersen, Nils Winter, Miroslav Gajdacz, Sune Mai, and Jan Arlt. The pump-probe coupling of matter wave packets to remote lattice states. *New Journal of Physics*, 14(8):083013, 2012.

[80] Poul L. Pedersen, Miroslav Gajdacz, Nils Winter, Andrew J. Hilliard, Jacob F. Sherson, and Jan Arlt. Production and manipulation of wave packets from ultracold atoms in an optical lattice. *Phys. Rev. A*, 88:023620, Aug 2013.

[81] C Zener. Non-adiabatic crossing of energy levels. *Proceedings of The Royal Society of London Series A*, 137(833):696–702, Sep 1932.

[82] Wenxian Zhang, D. L. Zhou, M.-S. Chang, M. S. Chapman, and L. You. Coherent spin mixing dynamics in a spin-1 atomic condensate. *Phys. Rev. A*, 72:013602, Jul 2005.

[83] L. Zhao, J. Jiang, T. Tang, M. Webb, and Y. Liu. Dynamics in spinor condensates tuned by a microwave dressing field. *Phys. Rev. A*, 89:023608, Feb 2014.

[84] Jasper S. Krauser, Jannes Heinze, , Nick Fläschner, Sören Götze, Ole Jürgensen, Dirk-Süren Lühmann, Christoph Becker, and Klaus Sengstock. Coherent multi-flavour spin dynamics in a fermionic quantum gas. *Nat Phys*, 8:813–818, 2012.

[85] J. S. Krauser, U. Ebling, N. Fläschner, J. Heinze, K. Sengstock, M. Lewenstein, A. Eckardt, and C. Becker. Giant spin oscillations in an ultracold Fermi sea. *Science*, 343(6167):157–160, 2014.

[86] M. Scherer, B. Lücke, J. Peise, O. Topic, G. Gebreyesus, F. Deuretzbacher, W. Ertmer, L. Santos, C. Klempt, and J. J. Arlt. Spontaneous symmetry breaking in spinor bose-einstein condensates. *Phys. Rev. A*, 88:053624, Nov 2013.

[87] Poul L. Pedersen, Miroslav Gajdacz, Frank Deuretzbacher, Luis Santos, Carsten Klempt, Jacob F. Sherson, Andrew J. Hilliard, and Jan J. Arlt. Spin dynamics in a two-dimensional quantum gas. *Phys. Rev. A*, 89:051603, May 2014.

[88] Anand Ramanathan, Sergio R. Muniz, Kevin C. Wright, Russell P. Anderson, William D. Phillips, Kristian Helmerson, and Gretchen K. Campbell. Partial-transfer absorption imaging: A versatile technique for optimal imaging of ultracold gases. *Rev. Sci. Instrum.*, 83(8):083119, 2012.

[89] Manuel Scherer. *Nichtklassische Zustände in spinor-Bose-Einstein-Kondensaten.* PhD thesis, Fakultät fü Mathematik und Physik, Leibniz Universität Hannover, 2011.

[90] M. Napolitano, M. Koschorreck, B. Dubost, N. Behbood, R. J. Sewell, and M. W. Mitchell. Interaction-based quantum metrology showing scaling beyond the Heisenberg limit. *Nature*, 471:486, 2011.

[91] M. R. Andrews, M.-O. Mewes, N. J. van Druten, D. S. Durfee, D. M. Kurn, and W. Ketterle. Direct, nondestructive observation of a Bose condensate. *Science*, 273(5271):84–87, 1996.

[92] N. V. Morrow, S. K. Dutta, and G. Raithel. Feedback control of atomic motion in an optical lattice. *Phys. Rev. Lett.*, 88:093003, Feb 2002.

[93] Jacob F. Sherson, Hanna Krauter, Rasmus K. Olsson, Brian Julsgaard, Klemens Hammerer, Ignacio Cirac, and Eugene S. Polzik. Quantum teleportation between light and matter. *Nature*, 443(7111):557–560, OCT 5 2006.

[94] JM Geremia, John K. Stockton, and Hideo Mabuchi. Real-time quantum feedback control of atomic spin-squeezing. *Science*, 304:270–273, 2004.

[95] Miroslav Gajdacz. Non-destructive imaging and feedback with ultra-cold gases. Progress report, 2013.

[96] D. B. Hume, I. Stroescu, M. Joos, W. Muessel, H. Strobel, and M. K. Oberthaler. Accurate atom counting in mesoscopic ensembles. *Phys. Rev. Lett.*, 111:253001, Dec 2013.

[97] G. Barontini, C. Weber, F. Rabatti, J. Catani, G. Thalhammer, M. Inguscio, and F. Minardi. Observation of heteronuclear atomic efimov resonances. *Phys. Rev. Lett.*, 103:043201, Jul 2009.